Laser diode systems for photodynamic therapy and medical diagnostics

Eva Samsøe

Lund Reports on Atomic Physics
LRAP-321

Doctoral Thesis
Department of Physics
Lund Institute of Technology
July 2004

Lund Institute of Technology
Lund University

Doctoral Thesis
Atomic Physics Division
Department of Physics
Lund Institute of Technology
P.O. Box 118
SE–221 00 Lund
Sweden

Lund Reports on Atomic Physics, ISSN 0281-2762
LRAP-321

ISBN 91-628-6144-1
Printed by Pitney Bowes Management Services, Dk

To Anders and my Family
In memory of my beloved Father ...

Abstract

This work concerns techniques for improvement of the coherence properties of diode lasers so that they may be used be used in two specific medical applications: (Interstitial) photodynamic therapy (PDT) and laser-induced fluorescence diagnostics. In the first application, spatial coherence is crucial, since the therapeutic light should be delivered through relatively thin optical fibers to optimize treatment and to facilitate minimally invasive treatment. In the second application a pulsed, blue source at 405 nm is desired. This has been approached by frequency doubling the output from an external-cavity laser diode at 810 nm. Thus, both spatial and temporal coherence are important to ensure that the second harmonic generation is efficient.

Two red (635 nm) laser diode systems for PDT, a first and a second generation, have been developed and tested in preliminary clinical trials. The first generation system is based on asymmetrical optical feedback from a $BaTiO_3$ crystal. This system is coupled into a thin (50 μm core diameter) optical fiber and tested in preliminary clinical trials involving interstitial PDT of solid tumors in rat. The second generation system couples two similar systems by means of polarization coupling, whereby the output power is doubled. The individual systems are based on asymmetrical feedback from ordinary mirrors. This system has been tested in PDT treatment of skin cancer in human and has been compared with a conventional treatment.

For laser-induced fluorescence diagnostics, an 810 nm external-cavity laser diode system with improved spatial and temporal coherence has been constructed. The system is based on a new configuration that employs double feedback from the first diffracted and the zeroth reflected order of a diffraction grating. The output from this system is frequency doubled to 405 nm using a single pass configuration with a periodically poled KTP crystal. It has been shown that the double grating feedback improves the second harmonic conversion efficiency by several orders of magnitude as compared with the freely running laser.

Sammanfattning

Arbetet i denna avhandling syftar till att utveckla bättre ljuskällor för fluorescensavbildning och fotodynamisk behandling av cancertumörer. Små kompakta diodlasrar är ideala ljuskällor för detta, men en del kliniska användningar kräver att deras prestanda förbättras. Gemensamt för de bägge diagnostik- och behandlingsmetoderna är att man behöver uppnå högre strålkvalitet av laserljus med hög effekt. Detta har till dels förverkligats i detta arbete genom att utveckla en speciell återkoppling av ljus tillbaka in i diodlasern med hjälp av en yttre kavitet.

Fotodynamisk tumörterapi (PhotoDynamic Therapy - PDT) är en behandlingsmetod som på senare tid utnyttjas allt mer i behandlingen av vissa tumörsjukdomar, medan metoden fortfarande utvecklas och utvärderas i kliniska studier för andra tumörtyper. Metoden innebär att patienten tar ett läkemedel som gör att tumören blir ljuskänslig. Om man sedan belyser tumören med ljus av en speciell färg, startar en kemisk reaktion som dödar tumörcellerna. Metoden har många fördelar, såsom att den är effektiv mot tumören, medan den ofta kan spara omkringliggande frisk vävnad. Läkningen after behandlingen är även ofta bättre än för de flesta andra behandlingsmetoder. Den stora nackdelen med metoden är att ljuset inte når till alla delar av tumören om tumören är stor, och därmed blir behandlingen inte effektiv i dessa delar av tumören. Vid behandling av större tumörer med PDT, är det därför en fördel att sticka in en eller flera optiska fibrer som kan belysa tumören innifrån, och därmed lysa ut tumören bättre. För att kunna göra detta effektivt, önskar man kunna leda ljuset i relativt tunna optiska fibrer. Problem uppstår då när man ska koppla in laserljuset in i fibrerna. För att detta ska kunna ske effektivt, behöver strålkvaliteten på laserljuset vara god. Arbetet i denna avhandling handlar bland annat om att förbättra strålkvaliteten av behandlingslasern, så att denna koppling blir effektiv och därmed göra det möjligt att utveckla bättre lasrar för denna behandling.

Fluorescensavbildning är ett diagnostiskt hjälpmedel som kan användas för att finna tidiga tumörer eller för att markera var tumörgränsen går. Med fluorescens menas ljus som molekyler i olika matrial skickar ut när de de belyses med ultraviolett eller

violett ljus. Fluorescens gör t.ex. att vita kläder lyser blått på diskotek där man har lampor med osynligt ultraviolett ljus i taket. När man använder fluorescens för diagnostik av cancer, utnyttjar man att tumörer fluorescerar annorlunda än frisk vävnad, eftersom de delvis innehåller andra molekyler. Denna typ av diagnostiska mätningar kan göras punktmässigt, där man belyser vävnaden genom en optisk fiber som hålles i kontakt med vävnaden som undersöks, eller genom en avbildning där en större vävnadsyta kan studeras. Ofta görs dessa undersökningar med hjälp av endoskop, så att vävnadsytor av inre organ, såsom matstrupe, magsäck, tarmar, urinblåsa, luftvägar, osv, kan undersökas. Detta medför att ljuset måste ledas genom optiska fibrer. Det är därmed viktigt att utveckla en kompakt och robust ljuskälla som klarar att ge tillräckligt mycket violett ljus genom en fibrer. Denna avhandling handlar delvis om utveckling med syfte att ta fram en sådan ljuskälla.

Diodlasrar kan vara konstruerade på olika sätt för att optimera olika egenskaper. De viktigaste egenskaperna är ofta uteffekten, strålkvaliteten och hur smalbandig lasern är (dvs hur bred lasertoppen är våglängdsmässigt). För de tillämpningar som nu är aktuella är uteffekten den viktigaste egenskapen, men de andra parametrarna är också mycket viktiga. Generellt kan man säga att ju högre uteffekt en laser har, ju sämre blir ofta de andra egenskaperna. Huvuddelen av arbetet för denna avhandling har varit att teoretiskt modellera, bygga upp och testa olika typer av yttre kaviteter till diodlasrar som väsentligt förbättrar en högeffektsdiodlasers strålegenskaper och bandbredd, utan att förlora för mycket ljus. Arbetet har dessutom gått ut på att effektivt konvertera rött ljus från en sådan laser till violett ljus i en olinjär optisk kristall. Detta kan vara den mest effektiva metoden idag att åstadkomma hög effekt med i diodlaser vid dessa våglängder.

Contents

Part II

Papers

Paper I: **A novel diode laser system for photodynamic therapy**
E. Samsøe, P. M. Petersen, P. E. Andersen, S. Andersson-Engels, and K. Svanberg
In: *Laser-tissue interactions, therapeutic applications, and photodynamic therapy*, eds. R. Birngruber, H. van den Bergh, Proc. SPIE **4433**, 134-139 (2001).

Paper II: **Improvement of brightness and output power of high-power laser diodes in the visible spectral region**
E. Samsøe, P. Malm, P. E. Andersen, P. M. Petersen, and S. Andersson-Engels
Opt. Commun. **219**, pp. 369-375 (2003).

Paper III: **Improvement of spatial and temporal coherence of a broad area laser diode using an external-cavity design with double grating feedback**
E. Samsøe, P. E. Andersen, S. Andersson-Engels, and P. M. Petersen
Opt. Express **12**, pp. 609-616 (2004).

Paper IV: **Second harmonic generation of 405 nm using periodically poled $KTiOPO_4$ pumped by external-cavity laser diode with double grating feedback**
E. Samsøe, P. M. Petersen, S. Andersson-Engels, and P. E. Andersen
Submitted to *Appl. Phys. Lett.*

Paper V: **An external-cavity laser diode at 635 nm for laser display applications**
N. Kjærgaard, E. Samsøe, H. Lausen, P. E. Andersen, and P. M. Petersen
Submitted *Opt. Commun.*

Paper VI: **Guiding of laser modes based on four-wave mixing in a semiconductor amplifier**
P. M. Petersen, E. Samsøe, S. Blaabjerg, and P. E. Andersen
Manuscript in preparation for *Phys. Rev. Lett.*

Additional material:

PATENT: **Laser system for tretament and diagnosis**
P. E. Andersen, E. Samsøe, P. M. Petersen, S. Svanberg, K. Svanberg, and S. Andersson-Engels
WO 02/103859 A2 (Risø ref. no. P.419).

IPA01: **A novel diode laser system for photodynamic therapy**
E. Samsøe, P. M. Petersen, P. E. Andersen, S. Andersson-Engels, and K. Svanberg
IPA 8th World Congress of Photodynamic Medicine, June 5-9 2001, Vancouver, Canada. Oral presentation.

ECBO01: **A novel diode laser system for photodynamic therapy**
E. Samsøe, P. M. Petersen, P. E. Andersen, S. Andersson-Engels, and K. Svanberg
European Conference on Biomedical Optics (ECBO), June 17-21 2001, Munich, Germany. Oral presentation with proceedings.

DOPS-NYT: **A novel diode laser system for photodynamic therapy**
E. Samsøe, P. E. Andersen, P. M. Petersen, S. Andersson-Engels, and K. Svanberg
DOPS-nyt **16**(4) (2001). Invited paper.

Part I

Chapter 1

Introduction

Lasers based on semiconductors are attractive in a clinical environment due to their compactness, simple operation, excellent efficiency, and relatively low costs. They are continuously replacing conventional lasers in medicine, as the wavelength range is expanded and the output power increased. Remaining drawbacks are poor spatial and temporal coherence of such lasers. These drawbacks lead to poor coupling efficiency to thin optical fibers, e.g. single-mode fibers, and poor conversion efficiency in nonlinear optical processes that requires a narrow spectral bandwidth, e.g. second harmonic generation.

Photodynamic therapy (PDT) is an interesting treatment modality for cancerous and precancerous lesions in addition to a number of other diseases. PDT involves irradiation of the diseased tissue with a light source that matches an absorption band of a preadministered tumor marker. To avoid thermal effects, lasers are often preferred due to their narrow spectral bandwidth. Furthermore, the ability to couple laser light into optical fibers, facilitating guidance of the therapeutic light, is advantageous. The most important drawback of PDT is the limited penetration of the therapeutic light.

Interstitial PDT of solid, deeper lying tumors or body cavities is a research area that receives a large amount of interest. For this treatment, it may be an advantage that the therapeutic light is guided through relatively thin optical fibers so that the treatment is minimally invasive and so that several fibers may be inserted at optimized positions within the lesion.

Laser-induced fluorescence diagnostics is a powerful method suitable for monitoring tissue before, during, and after PDT treatment. It relies on the excitation and monitoring of fluorescence from the tumor selective compound added in connection with the PDT treatment. By monitoring this fluorescence, a means of diagnosis is provided, and the physician may use this information

to keep track of important treatment parameters, such as tumor boundaries and treatment status of irradiated tumor volume.

This Ph.D. project is the result of a collaborative project between the Optics and Plasma Research Department (OPL) at Risø National Laboratory in Denmark and Lund University Medical Laser Centre in Sweden. Experimental setups concerning improvement of the coherence properties of diode lasers and their adaptation to a clinical environment were developed at Risø from where they could be transported to Lund University Hospital for clinical testing. Furthermore, part of the clinical testing was performed at Marselisborg Hospital in Denmark.

1.1 Status of clinical apparatus

The first laser system, an Nd:YAG laser-pumped dye laser system, for ALA-PDT at Lund University Medical Laser Centre was implemented in 1991. This system was relatively expensive and voluminous with a weight of about 300 kg. A further disadvantage with such a laser is the complexity of management. In 1998, a commercial diode laser system for PDT, yielding approximately 1.5 W at 635 nm, was implemented at Lund University Medical Laser Centre (CeramOptec, Ceralas PDT635). This unit only weighs about 15 kg and is remarkably smaller and easier to handle than the previous system. However, this diode laser system (and all other commercial diode lasers available for PDT) delivers the therapeutic light through relatively thick optical fibers of 400 μm core diameter or more. At Lund University Medical Laser Centre, intensive research regarding interstitial PDT is ongoing. It is believed that this treatment modality may be optimized by the use of thinner treatment fibers. However, if fibers thinner than 400 μm are used in connection with the commercial PDT laser, a large amount of output power is lost. For PDT at Lund University Medical Laser Centre a wavelength of 635 nm is required due to the choice of tumor marker (ALA-PDT).

For laser-induced fluorescence diagnostics, two systems are currently available at Lund University Medical Laser Centre. Both systems are pulsed to facilitate suppression of the surrounding white light by gated detection. One is a nitrogen laser-pumped dye laser system (337 nm or 405 nm) and the other is a frequency doubled alexandrite laser (385 nm). The former system has a pulse energy around 1-2 μJ and can only be used for point monitoring purposes. The latter system has a pulse energy around 1 mJ and can be used for imaging as well. However, the alexandrite laser system is large ($0.5 \times 1 \times 1.5\,\mathrm{m}^3$), heavy ($> 200$ kg), and needs water cooling. Recently, a compact system based on a GaN laser diode (400 nm) has been introduced. However, the output power from this system is low (< 5 mW) and the laser is not pulsed.

Thus, background light has to be turned off during fluorescence measurements, and that is a serious drawback in a clinical environment. For laser-induced fluorescence diagnostics of malignant and premalignant lesions at Lund University Medical Laser Centre, a wavelength around 405 nm is required.

1.2 Specifications

The purpose of this Ph.D. work was to develop and construct diode laser-based systems suitable for (interstitial) PDT treatment and laser-induced fluorescence diagnostics. The systems should meet the required specifications, i.e. the PDT system should emit approximately 1 W at 635 nm through thin optical fibers with core diameter(s) around 50 μm. The system for laser-induced fluorescence should approximately resemble the frequency doubled alexandrite laser system. However, it was estimated that a pulse energy around 0.1 mJ was sufficient for the purpose. The wavelength should be 405 nm, the pulse length should not exceed 1 μs, and the repetition rate should be in the range 25-50Hz.

1.3 Motivation

There are no commercial diode laser-based systems available for (interstitial) PDT that deliver the therapeutic light through fiber(s) of the desired thin diameter. Neither is there, to the authors knowledge, a diode laser-based source for laser-induced fluorescence diagnostics available. The tasks were to develop diode laser-based systems with improved coherence properties and adopted to a clinical environment so that the clinical requirements could be met. At the time of initiation of this project, broad area laser diodes at 635 nm and 405 nm were available with output powers around 250 mW and 5 mW, respectively. The PDT system was realized in a first (**Paper I**) and second (**Paper II**) generation using external-cavity configurations with optical feedback from a phase conjugate crystal and mirrors, respectively. In the second generation system, the output power was doubled by the coupling of two independent external-cavity systems. The diagnostic system was based on frequency doubling of an external-cavity diode laser with improved spatial and temporal coherence. It is shown that the so-called double grating feedback system (**Paper III**) improves the second harmonic conversion efficiency by several orders of magnitude as compared with the freely running laser (**Paper IV**). In the meantime, the blue GaN based laser diodes have become available at high (>30 mW) output powers. However, these devices lack the long lifetime of the GaAs based near infrared diodes and their wavelength is limited by the material band gap. Furthermore, the laser for diagnostics should be pulsed. By the use of second har-

monic generation, large peak powers in the blue spectral region may be obtained by pulsing the pump (fundamental wavelengh) laser.

1.4 Structure of thesis

The thesis has been divided into Part I and Part II. Part I contains seven chapters and serves as an introduction to the scientific work, which is presented as six original papers in Part II.

Chapter 2 introduces high-power diode lasers, which are the lasers applied throughout the experimental work of this Ph.D. project. The main focus has been put on the semiconductor materials relevant for the present work, i.e. materials emitting at 405 nm, 635 nm, and 810 nm. Some experimental results are present at the end of chapter 2. The poor coherence properties of diode lasers may be improved by implementation in an external cavity. Different variations of such cavities, which have been applied in the experimental work, are presented in chapter 3, which also provides some experimental results. Chapter 4 introduces the theory of second harmonic generation, which is a technique applied in this work to generate blue light for fluorescence diagnostics. In chapter 5 the basic mechanisms for PDT are described and followed by laser-induced fluorescence diagnostics, which is treated in chapter 6. Finally, in chapter 7, the clinical experience with the developed laser systems is described. Only the lasers for PDT were tested in the clinic. However, clinical evaluation of both systems is provided and an outlook regarding their future clinical relevance is given. This chapter concludes Part I of the thesis and is followed by the scientific papers in Part II.

Chapter 2

High-power diode lasers

Diode lasers are preferred in many of todays photonics applications due to their numerous advantages, such as compactness, high efficiency, and reasonable cost. Since the invention of the semiconductor laser in 1962 [1–4] its performance has improved steadily, primarily in terms of lifetime and output power. This chapter deals with the basic physical properties of typical high-power diode lasers.

2.1 Emission and absorption in semiconductors

Unlike gas and solid-state lasers, which have sharp energy levels, the energy levels of diode lasers are broadened into energy bands, see Fig. 2.1. In the figure, $E_c(k)$ and $E_v(k)$ denote the electron energies in the conduction band and in the valence band, respectively, and $k = 2\pi/\lambda$ is the wavenumber. For a free electron, the energy as a function of wavenumber is given by $E(k) = (\hbar^2 k^2)/(2m_0)$ since the kinetic energy of a free electron is $E = p^2/(2m_0)$, where m_0 is the free electron rest mass and $p = \hbar k$ is the quantum-mechanical momentum with $\hbar = h/(2\pi)$ being the reduced Planck constant. Thus the electron energies show parabolic band structures, which are given by

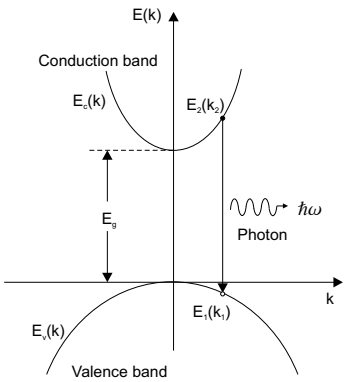

Figure 2.1. *The parabolic conduction and valence bands, $E_c(k)$ and $E_v(k)$ are separated by an energy band gap, E_g. Recombination of an electron at $E_2(k_2)$ in the conduction band and a hole at $E_1(k_1)$ in the valence band occurs at $k_1 = k_2$ and generates a photon with energy $\hbar\omega$.*

$$E_c(k) = E_g + \frac{\hbar^2 k^2}{2m_e} \quad \text{and} \quad E_v(k) = -\frac{\hbar^2 k^2}{2m_h}\,, \tag{2.1}$$

where E_g denotes the energy gap between the two bands. The introduction of effective masses m_e and m_h ($m_e, m_h \neq m_0$ in general) for electrons and holes, respectively, accounts for the interaction of the carriers with the solid-state lattice. The energy gap, $\mathrm{E_g}$ between the conduction and valence bands is typically in the order of $0.5 - 2.5\,\mathrm{eV}$ [5] for semiconductor materials used for high-power diodes. Conservation of energy and momentum must be fulfilled

in the radiative band-to-band transitions and the associated absorption or emission of photons. Thus, since the momentum $\hbar k$ of the photon is negligibly small ($p = \hbar k = \hbar\omega/c = E_{\text{photon}}/c$) in comparison to the momentum of the free carriers, radiative transitions between the conduction and valence bands occur at the same wavenumber k, i.e. $k_2 = k_1$ in Fig. 2.1.

When pumped, the active volume has a large concentration of electrons in the upper energy band, the conduction band, and holes (missing electrons) in the valence band. Three types of radiative transitions transitions occur in semiconductors. These are spontaneous emission, (stimulated) absorption, and stimulated emission. The processes are sketched in Fig. 2.2.

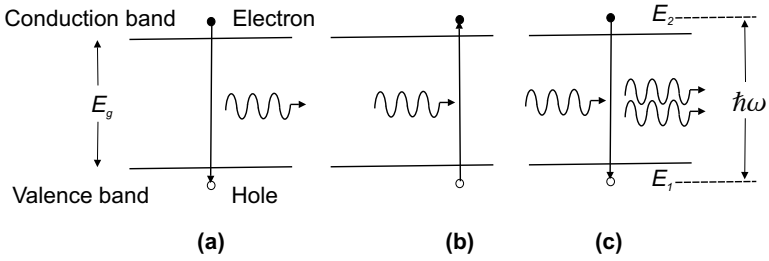

Figure 2.2. *Radiative band to band transitions in semiconductors: (a) Spontaneous emission, (b) Absorption, and (c) Stimulated emission.*

In thermal equilibrium at temperature T, The Fermi function, $f(E,T)$, expresses the probability whether a state with energy level E is occupied by an electron:

$$f(E,T) = \frac{1}{\exp\left(\frac{E-E_F}{k_B T}\right) + 1}\,, \tag{2.2}$$

where $k_B = 8.617347 \times 10^{-5}\,\text{ev/K}$ is the Boltzmann constant and E_F is the Fermi-level energy. At $T = 0\,\text{K}$, $f(E,T) = 1$ (i.e. all electronic states filled) for $E < E_F$ and $f(E,T) = 0$ (all states empty) $E > E_F$.

An electron in the conduction band may recombine with a hole in the valence band under the emission of a photon, with random direction and phase. This is called spontaneous emission (Fig. 2.2 (a)) and is the dominating process in light emitting diodes (LEDs). This transition must be proportional to the product of the electron density at E_2, and the hole density at E_1. The density of electrons in the state E_2 is given by the density of electronic states D_{E_2} times the probability that they are occupied, $f(E_2,T)$. Furthermore it depends on the density of holes at the energy E_1, which is the density of electronic states $D(E_1)$ times the probability that they

are not occupied by an electron, $[1-f(E_1,T)]$. Thus the transition rate per volume for spontaneous emission, R_{sp} of photons with a fixed energy $\hbar\omega = E_2 - E_1$ ($k_2 = k_1$) may be expressed as:

$$R_{sp} = AD(E_2)f(E_2,T)D(E_1)[1-f(E_1,T)]\,, \qquad (2.3)$$

where A is the proportionality constant for spontaneous emission.

On the other hand, a photon may be absorbed thereby generating an electron-hole pair (Fig. 2.2 (b)). The transition rate, R_{12} for this process is proportional to 1) the density of non-occupied states in the conduction band at energy E_2: $D(E_2)[1-f(E_2,T)]$, 2) the density of states occupied by electrons in the valence band at E_1: $D(E_1)f(E_1,T)$, and 3) the density of photons $\rho(\hbar\omega)$ with energy $\hbar\omega = E_2 - E_1$. We thus have:

$$R_{12} = B_{12}\rho(\hbar\omega)D(E_1)f(E_1,T)D(E_2)[1-f(E_2,T)]\,, \qquad (2.4)$$

where B_{12} is the proportionality constant for spontaneous emission.

Finally, a photon may stimulate the recombination of an electron-hole pair, thus leading to the emission of yet another photon, with the same direction and phase as the first photon. Due to the coherence between the stimulating and the emitted photons, this stimulated emission is the process leading to the optical amplification responsible for laser action (Fig. 2.2 (c)). Analogous to Eq. (2.7), the rate for stimulated emission R_{21} becomes:

$$R_{21} = B_{21}\rho(\hbar\omega)D(E_2)f(E_2,T)D(E_1)[1-f(E_1,T)]\,, \qquad (2.5)$$

where B_{21} is the proportionality constant for spontaneous emission.

The proportionality constants, Einstein's A and B coefficients, in Eqs. (2.3)-(2.5) can be shown to satisfy [5]

$$B_{12} = B_{21} = B, \quad A = \frac{n^3}{\pi^2\hbar^3c^3}(\hbar\omega)^2 B\,, \qquad (2.6)$$

where n is the refractive index of the medium.

Laser operation can only be achieved if the rate of stimulated emission is larger than the absorption rate, i.e. $R_{12}/R_{21} < 1$. Furthermore, by using Eqs. (2.3), (2.5), and (2.6), the ratio between the rates of stimulated and spontaneous emission, can be formulated:

$$\frac{R_{21}}{R_{sp}} = \frac{B}{A}\rho(\hbar\omega) = \frac{\pi^2\hbar^3c^3}{n^3(\hbar\omega)^2}\rho(\hbar\omega)\,. \qquad (2.7)$$

From this ratio it is apparent that a high photon density $\rho(\hbar\omega)$ is necessary in order to suppress spontaneous emission. Furthermore, it is observed that a higher value of the photon density is necessary for lasers with higher photon energy $\hbar\omega$. This means that short wavelength lasers, e.g. blue or red diode lasers, require a higher photon density in order to operate than does e.g. infrared diodes.

2.2 Structures of diode lasers

A diode laser is realized from a number of basic elements, such as a gain medium, a waveguide, other guiding/confinement mechanisms, and a resonator. A typical diode laser, exemplified by a double heterostructure, is shown in Fig. 2.3. The coordinate system represents the lateral (x), the transverse (y), and the longitudinal axes (z), respectively. The active layer, which is typically made of $Al_xGa_{1-x}As$ (x: molar fraction) (see section 2.3.1) is sandwiched between two cladding layers of another semiconductor material. The cladding layers are p- and an n-doped, respectively such that when the p-n junction is forward biased, electrons and holes are injected into the active region and optical gain by stimulated emission becomes possible. The laser cavity is formed between two cleaved surfaces of the sandwich-like structure. The end-surfaces of the cavity, the *facets*, have a natural reflection coefficient of approximately 30%. Most commonly, two different coatings are applied to the facets, such that and end facet and an output facet are formed. The end-facet typically has a high reflection coating applied (R > 99%), while the output-facet is anti-reflection coated (R < 4-10 %). The lasing action takes place in the active medium, which is also referred to as the *junction*. The external voltage acts as a pump, constantly providing new electrons and holes, which migrate into the active region where they recombine and leads to the emission of a photon. When the external current exceeds a critical value, known as the threshold, population inversion is achieved. When this happens, the rate of photon emission is superior to the rate of absorption and the lasing action takes place.

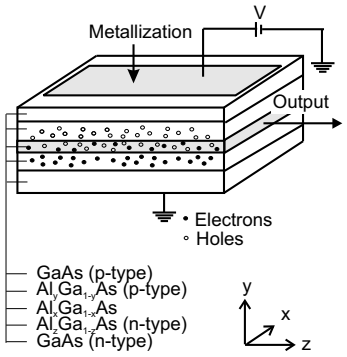

Figure 2.3. *The double heterostructure diode laser exemplified by a AlGaAs structure. The active layer is sandwiched between the cladding layers. The coordinate system represents the lateral (x), the transverse (y), and the longitudinal (z) axes, respectively.*

Fundamental mode AlGaAs lasers typically have an emitting aperture of $1\times3\,\mu m^2$ ($y\times x$). The output power of such lasers is limited to approximately 200 mW during continuous wave (CW) operation. This limitation is due to the occurrence of damage effects, such as local heating damage or catastrophic optical damage at the facet mirrors [6, 7]. Such damage effects typically occur when the intensity density becomes too large. Numerous approaches have been made in order to increase the power level of diode lasers. Some of them are discussed in the sections 2.2.1-2.2.3 below.

2.2.1 Broad area lasers

The most straight-forward solution to obtain high output power isi to simply increase the area of the emitting aperture, thereby creating a broad area laser (BAL) diode, see Fig. 2.3. This may be done by applying a wide metallization contact, also known as the stripe, on top of the structure. In a BAL the lateral dimension of the junction is typically 100-200 μm, but BALs up to at least 1 mm have been manufactured [8]. However, when increasing the width of the junction, several problems occur. When the width is increased to above approximately 6 μm, the laser is no more single-mode and several lateral modes emerge on the expense of spatial and temporal coherence. The intensity distribution on the output facet of a BAL has a periodic variation due to a self-induced filamentation mechanism [9]. The filamentation is caused by a carrier-induced change of refractive index, know as the lateral antiguiding effect, which in addition results in a double-lobed intensity pattern in the far field. Lateral antiguiding and filamentation effects are discussed in more detail in section 2.4 and the optical modes of BALs are discussed in section 2.5. When the width exceeds a couple of hundred microns, lateral lasing may occur. Finally, thermal effects takes place in wide aperture BALs, which causes an envelope on the refractive index profile [10]. Commercial BALs with a stripe width of 200 μm emit up to approximately 4 W during CW operation. The experimental work performed during this Ph.D. is based on work with BALs (**Papers I-V**). Therefore, this thesis will mainly focus on these structures.

2.2.2 Laser diode arrays

The structure of laser diode arrays (LDAs) is based on multiple stripes placed next to each other. Proton implantations between the stripes enhances the separation of the current flow from each stripe. This results in a controllable periodic gain profile and the self-induced filamentation, known from the BALs, may be avoided. The intensity profile on the facets is controlled by controlling the stripes (and thus the gain profile). The resulting intensity profile is generally more uniform than for the BAL such that the risk of facet damage, is reduced. The width of a LDA is typically 100-500 μm containing a number of 5-10 μm wide stripes, with a separation similar to the stripe width. The optical power from a commercial LDA is on the order of 1-2 W CW for a 100 μm wide array with ten stripes.

2.2.3 Laser diode bars

Laser diode bars (LDBs) consists of a number of arrays placed next to each other in a monolithic structure. The width of the individual

array is typically on the order of a few hundreds of microns and they are generally separated by a distance of that same order. The ratio between the optically active area to the whole area of the bar, is between 30 and 80 % [11]. The typical width of a LDB is around 10 mm and the output power may exceed 100 W in CW mode (see e.g. [12]). However, the high power is obtained on the expense of coherence. Further power increase to several hundreds of watts may be obtained by stacking LDBs on top of each other thereby fabricating stacked arrays or two-dimensional LDBs [13].

2.3 Materials for high-power diode lasers

Semiconductor materials that exhibit lasing action are represented in large numbers, covering the optical spectrum from ultraviolet to far infrared. One of the most important criteria when selecting a semiconductor material is the reduction of lattice defects. This criteria is related to the quality of the interface between the two semiconductor materials with different band gaps. Typically, the lattice match, i.e. the match between the lattice constants of the two compounds, should be better than 0.1 % [4] for a high quality lattice interface. Another important criteria is, of course, the desired lasing wavelength. Since the photon energy is approximately equal to the band gap energy (see section 2.1), the lasing wavelength is found from $E_g = hc/\lambda$, where h is the Planck constant and c is the speed of light in vacuum. With E_g expressed in electron volts, the lasing wavelength in micrometers is given by [4]:

$$\lambda = \frac{1.24}{E_g} \tag{2.8}$$

In the following, a brief discussion of three of the most important structures for semiconductor lasers will be given. The selected materials are of interest for active regions with emission around 800 nm, 630 nm, and 400 nm, respectively. These wavelengths are central in the present work.

2.3.1 GaAs and AlGaAs

(Aluminium) gallium arsenide ((Al)GaAs) was already mentioned as a candidate for a semiconductor laser material in section 2.2. This material is widely used for manufacturing near-infrared laser diodes around 800 nm and it is the most intensively investigated (see e.g. [14]). The reason for its success is mainly a small lattice mismatch between AlAs and GaAs, which result in a fairly practicable fabrication of heterostructures, since the requirements on composition control are lower than for other structures. Furthermore, arsenide is easier to handle than e.g. phosphide (P), which

has a high vapor pressure and occurs in different modifications, some of which self-ignite. The limitations in (Al)GaAs are mainly related to impurity problems. Increasing the content of Al will increase the impurity incorporation in the structure, due to the reactive nature of Al, which result in an increased reaction rate for formation of oxides. The oxide formation will decrease as temperature increases, which is why high growth temperatures around 750°C are used when growing AlGaAs lasers. Also carbon (C) impurities are found in AlGaAs, but it is the addition of Al into the active layer, that lead to degradation of performance due to its introduction of centers of nonradiative recombination [15, 16]. However, AlGaAs lasers are in general highly reliable structures with lifetimes exceeding tens of thousands of hours. AlGaAs laser diodes are used in the work described in **Papers III-IV**.

2.3.2 GaInP and AlGaInP

(Aluminium) gallium indium phosphide ((Al)GaInP) lattice matched to GaAs is used for manufacturing visible red laser diodes around 630 nm. The lattice match is far from as well established as for AlGaAs and the red diode lasers remain a challenge to manufacture at high powers. GaInP has also found its applications in the cladding layers of the longer wavelength AlGaAs-structures [17]. The rate of oxidation in GaInP is much smaller than in the AlGaAs devices, which makes the red laser diodes more robust against facet damage, such as catastrophical optical damage. However, as for AlGaAs, the incorporation of Al lead to an enhanced oxide impurity incorporation. Again, this problem may be overcome by the use of high growth temperatures, which suppresses the incorporation of oxygen in the structure. However, due to the risk of re-evaporation of In, the temperature must not be too high. The temperature range for growing these structures is thus rather narrow and contributing to the challenge in manufacturing these devices [18]. AlGaInP based laser diodes are applied in the work described in **Papers I-II, V**.

2.3.3 InGaN, AlGaN, and GaN

The (indium/aluminium) gallium nitride (In/Al)GaN-based laser diodes emit their radiation at the ultraviolet-blue/green wavelengths around $370 - 470$ nm. These lasers have experienced a major break through during the past decade. In the beginning of the nineties, S. Nakamura and coworkers initiated an intensive work in the area, and in 1999 the first commercial products from violet InGaN-based laser diodes became available (see [19] and references therein). InGaN structures grown on sapphire substrates have a large number of threading dislocations originating from the interface between GaN and the sapphire substrate, which suffer from a

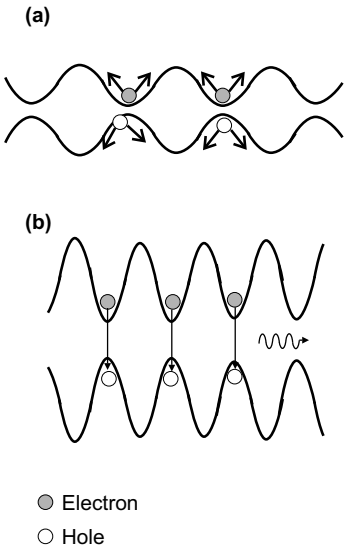

Figure 2.4. *Localized energy states formed by In composition fluctuations: (a) When the fluctuations are small, carriers easiily overflow the localized states with increasing current, (b) When the fluctuations are large, carriers are still confined even at high current operation [29].*

large lattice mismatch of 15% [20, 21]. These defects lead to the formation of non-radiative recombination centers ("dark spots") at the dislocations. In order to reduce the number of threading dislocations in the laser diodes, epitaxially laterally overgrown GaN (ELOG) on sapphire was developed [22–24]. Using ELOG, the number of dislocation were reduced, but the lifetime of the laser diodes (< 500 hours) was still very low compared to the lifetime of the InGaN-based LEDs (> 100.000 hours). This difference was attributed to the difference in operating current density in the two devices and to localized energy states formed by In composition fluctuations [20, 25–28]. The effect of varying In composition fluctuations is depicted in Fig. 2.4. When the In composition decreases, the In composition fluctuations decrease, and the carriers easily overflow the localized states with increasing current (Fig. 2.4 (a)). However, with increasing In composition, the degree of In composition fluctuations increase and the carriers are still confined even at high currents (Fig. 2.4 (b)). At low currents, the carriers are easily captured by localized energy states formed by In composition fluctuations and they radiatively recombine before they are captured by non-radiative recombination centers formed by the dislocations [30]. When current is increased, some carriers can overflow from the localized energy states due to a small In composition fluctuation, and reach non-radiative recombination centers. As a result, the internal loss of the laser diode-cavity and the threshold current density of the laser diode is increased, which leads to a decrease in efficiency and a shortening of lifetime. The lasing wavelength decreases with decreasing In composition. Furthermore, the In composition fluctuations decrease with decreasing In composition. This means that the problem is most pronounced for laser diodes at the short UV-blue wavelengths $\lambda \lesssim 400\,\mathrm{nm}$ [29]. By using ELOG, and thereby reducing the dislocation density and threshold current desity, the lifetime of the InGaN/GaN/AlGaN structures was increased from around 500 hours at 30 mW in the year 2000 [29] to several thousands of hours today [31]. Recently, an engineering sample with an output power of 60 mW and an estimated lifetime exceeding a couple of thousands hours, became available [31]. The InGaN laser diodes must be remembered when considering the possibilities for simple laser systems for laser-induced fluorescence diagnostics.

2.4 Field confinement

Different mechanisms are available to confine the optical field in the active region. A convenient way to describe the confinement of the optical field is through the confinement factor [5] (or filling factor [4]) Γ, which represents the fraction of the mode energy contained within the active region:

$$\Gamma = \frac{\int_{-d/2}^{+d/2} J(y)dy}{\int_{-\infty}^{\infty} J(y)dy} . \tag{2.9}$$

Here $J(y)$ is the optical intensity pattern along the direction y and d is the thickness of the active layer so that this is an expression for the transverse confinement factor, see Fig. 2.5. Since Γ depends on the overlap of the optical mode pattern with the gain region of the laser, it can be used to describe the relation between modal gain g_m and material gain g, $g_m = \Gamma g$.

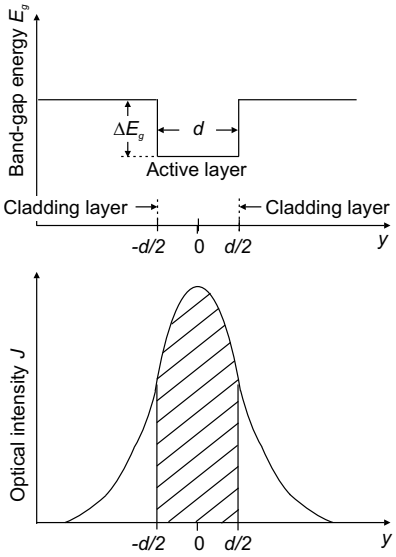

Figure 2.5. *The confinement factor Γ is defined as the overlap between the mode pattern and the active region (bottom). The top figure depicts the corresponding band-gap energies in the transverse direction of the structure.*

2.4.1 Transverse confinement

Fig. 2.6 illustrates the simultaneous confinement of carriers and the optical wave in the transverse direction (y) of the double heterostructure laser (Fig. 2.3) when it is forward biased by the application of an external voltage. The active layer with band gap E_g, refractive index n_2 and thickness d is sandwiched between the high-band-gap cladding layers. The band gap of the cladding layers is $E_{g,cl}$ and the refractive index is n_1, with $n_2 > n_1$, such that the optical field is confined to the active region. For sufficiently small index step and core thickness, a nearly Gaussian field distribution may be obtained since only the fundamental mode propagates. The refractive index n_{eff} experienced by an optical wave

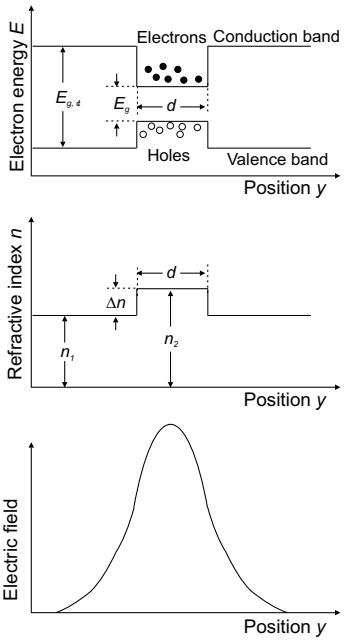

Figure 2.6. *Transverse confinement of carriers and field in the double heterostructure diode laser. Shown are the electron energy diagram (top), the refractive index profile (middle), and the the electric field distribution (bottom) of the fundamental nearly Gaussian optical mode.*

travelling in the active medium is different from the refractive indices of the core and the cladding, $n_1 \leq n_{eff} \leq n_2$. The confinement mechanism described above, is know as index-guiding, since the refractive-index discontinuity between the active an cladding layers is responsible for the mode confinement through the total internal reflection occurring at the interface.

2.4.2 Lateral confinement

There is no index-guiding in the lateral direction of the double heterostructure laser shown in Fig. 2.3. In this direction, the carriers and the optical field may be confined by current-confinement leading to a gain-guided lateral waveguide, see Fig. 2.7. The current is confined by controlling the width W of the metallization contact, i.e. by providing a current aperture, on top of the structure. By narrowing W, a better confinement of the injected carriers and thus a narrower gain region for the optical field is obtained. However, gain-guided devices suffer from an effect known as antiguiding, which leads to a broadening of the optical field. This effect is discussed in the paragraph below.

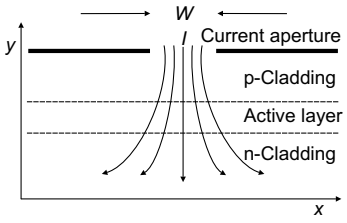

Figure 2.7. *Lateral current confinement. The current I is injected through the aperture of width W which confines the carriers.*

Outside the metallization stripe, an optical wave experiences high optical losses. If a single-lateral-mode device is desired, the current aperture has to be small enough to allow only for amplification of the fundamental lateral mode. Pure current-confined lasers are often referred to as stripe-lasers and the lateral confinement of the optical field is formed by gain-guiding. Other lateral guiding mechanisms are possible. Lateral index-guiding is implemented by introducing a step in the thickness of the upper cladding layer, such that a lateral effective refractive index step provides the guiding. A typical example of a lateral index-guided laser is the ridge-waveguide laser [5]. Finally, lateral carrier confinement may be implemented by an epitaxial regrowth technique, where barriers are grown and then used to prevent the lateral diffusion of electrons and holes. The buried heterostructure laser is an example of a diode laser with all three types of lateral confinement implemented [5]. The lasers used in the experiments carried out in this work are all index-guided in the transverse direction and gain-guided in the lateral direction. Their stripe widths are all in the range $W = 100 - 200\,\mu$m, i.e. they are all multi-lateral mode.

Lateral antiguiding

The increase in carrier density (increase in gain) just beneath the stripe region leads to a local reduction of refractive index since the refractive index of a semiconductor materials depends on the concentration of free carriers [4]. The local decrease in refractive index in the center of the device will broaden the optical field towards the edges of the active region. This *antiguiding* of the lateral

optical field may be quantified through the antiguiding parameter [4] (also known as the line width broadening factor [32]:

$$\beta_c = -2k_0 \frac{\Delta n}{\Delta g}\,, \tag{2.10}$$

where k_0 is the free-space wave vector and Δn is the change in the real part of the refractive index when the gain has changed Δg due to a change in the carrier density. The antiguiding parameter β_c thus describes the coupling between the carrier-concentration induced variations of real (refractive index) and imaginary (gain or loss) parts of complex index of refraction, which is responsible for defocusing and broadening of the optical field. The change $\Delta\tilde{n}$ in local complex refractive index originating from a change in the carrier density in the center of the active layer, is given by

$$\Delta\tilde{n} = \Delta n + i\Delta g/(2k_0)\,, \tag{2.11}$$

where i is the imaginary unit. The antiguiding parameter β_c varies in general, e.g. with current, but is often treated as a fixed parameter. The sign in Eq. 2.11 is chosen to have β_c positive for semiconductor materials [32], and its value for GaAlAs lasers typically lie in the range 1.5-3 [33].

For lasers with a broad-stripe geometry, the antiguiding effect will lead to a radiation pattern with two symmetric lobes in the far field. This is due to the lateral variation in effective refractive index, which imparts an overall phase curvature to the travelling wave mode (as opposed to the transverse, planar phase front). Diffraction from the edges of the output-facet results in a double-lobed intensity distribution in the far field.

Furthermore, the antiguiding effect will lead to filamentation for BALs with stripe widths $W \gtrapprox 6\,\mu$m [34]. Due to stimulated emission, the gain is locally depleted in high intensity regions (spatial hole-burning), which leads to a local increase in refractive index. Thus the optical field experiences self-focusing and a periodic variation in the lateral intensity profile occur. The spatial modes of diode lasers are treated in sections 2.5.1 - 2.5.2.

2.5 Emission characteristics

This section deals with the emission characteristics of laser diodes, with the main focus put on BALs. The full derivation of the BAL mode structure is beyond scope of this thesis. However, main results will be present and the physical mechanisms will be discussed. Throughout this section, we consider modes with electrical fields $\mathbf{E}_m$ of each mode m of the form [4]:

$$\mathbf{E}_m(x,y,z) = \hat{\mathbf{e}}\phi_m(y)\psi_m(x)\exp(i\beta_m z)\,, \tag{2.12}$$

where $\hat{\mathbf{e}}$ is the polarization vector, $\phi_m(y)$ and $\psi_m(x)$ are the field distributions of the m^{th} transverse and lateral modes, respectively, and β_m is the propagation constant of the m^{th} mode. In Eq. (2.12), we have assumed the effective index approximation [4], which splits up the problem into two one-dimensionnal parts in stead of having one two-dimensional wave equation. This approximation is valid when the dielectric constant $\epsilon(x,y)$ varies slowly in the lateral x direction compared to its variation in the transverse y direction. In general several spatial modes oscillate, and the resulting field is a superposition of the individual modes.

2.5.1 Transverse modes

The transverse modes depend on the thicknesses and refractive indices of the various layers used to fabricate the semiconductor laser. In the transverse direction, where the laser is index-guided, the waveguide is generally designed in such a way that only the fundamental spatial mode is supported. In practise, this is done by controlling the thickness of the active layer d. The transverse field distributions $\phi_m(y)$ are obtained by solving the time-independent wave equation, obtained from Maxwells equations [4] and inserting the boundary conditions (slab waveguide). The solutions are trigonometric functions in the active layer with an evanescent exponentially decaying field in the cladding. Due to the periodic nature of trigonometric functions, several solutions exists. However, a condition on the active-layer thickness may be formulated that ensures oscillation of the fundamental transverse mode only. The condition is [4]

$$d < \frac{\lambda}{2}(n_2^2 - n_1^2)^{-\frac{1}{2}}\,, \tag{2.13}$$

where n_2 and n_1 are the refractive indices of the active and cladding layers, respectively, with $n_2 > n_1$, and $k_0 = 2\pi/\lambda$ is the vacuum wavenumber. $D = k_0(n_2^2 - n_1^2)^{1/2}d$ is the normalized waveguide thickness. The single-transverse-mode condition is usually satisfied in practical devices, and it holds for all the diode lasers used and described in **Papers I-VI**. The fundamental, almost Gaussian, mode in the transverse direction is denoted $\phi_0(y)$.

2.5.2 Lateral modes

The lateral-mode behavior depends on the guiding mechanism in the lateral direction. Here we will only consider laterally gain-guided devices, with the main focus on the lateral modes of BALs, which we will denote BAL modes.

As noted in section 2.4.2, BALs suffer from filamentation [34], originating from the antiguiding effect and the boundary conditions (the edges of the structure). As a result of local gain depletion, spatial-hole burning induces self-focusing of the optical beam within the semiconductor laser [35, 36]. Furthermore, a positive feedback mechanism between the field and the material which forms its confining waveguide occurs, since the carrier-density is dependent on the intensity. In regions with high intensity, the gain is locally depressed by stimulated emission, which lead to a local increase in refractive index, and thus a further confinement of the light. The situation is shown in Fig. 2.8.

The lateral modes depend on the gain and index gratings introduced by the steady-state carrier distribution. In the near field (on the output facet), they turn out to consist of a large, broad dc value with a small ripple (filamentation) superimposed on it, see Fig. 2.8. In the far field, as mentioned in section 2.4.2, they show a double lobed behavior originating from diffraction due to the antiguiding effect.

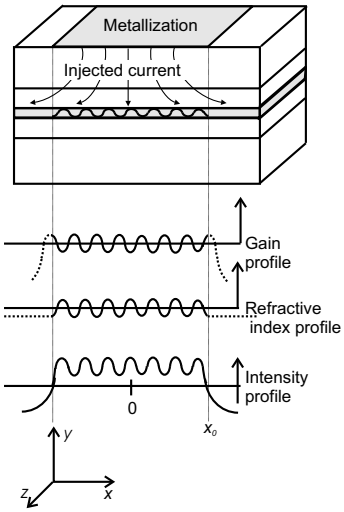

Figure 2.8. *Carrier induced gain and index gratings in the lateral direction. The resulting near field has a ripple superimposed on a large DC field. See Ref. [37].*

In order to obtain the lateral modes, $\psi_m(x)$, where m denote mode index, the wave equation has to be solved with the proper gain and carrier induced index change inserted (both dependent on the carrier-density profile). A complete description of the lateral BAL modes is found in the model by Mehuys *et al.* [37]. This model describes the self-stabilized nonlinear lateral modes of BALs, and takes into account the carrier induced gain and index gratings in addition to the intensity induced gain depletion (the positive feedback mechanism) that further confines the light and leads to a self-stabilization condition above a certain current level or saturation intensity. This comprehensive model serves as a more detailed description of the phenomena observed in BALs. However, the main experimental observations may be explained in a much simpler way, by the introduction of the perturbed broad-area model by Verdiell *et al.* [10]. Though, originally developed to describe the modes of multiple-stripe LDAs, experiments show that this model serves as a description of the main experimentally observed features of BALs as well. The perturbed broad-area model, however, does not take into account the intensity induced gain depletion. Below a brief review of the main results, applicable to BALs, are given in order to understand the experimentally observed behavior.

The infinite square potential well

Let us first consider a simple, but very illustrative, approach to the problem. Assume that the optical field is confined in an infinite square well potential with half-width x_0, corresponding to the half-width of the junction ($W/2$). Outside the well, infinite absorption is assumed, i.e. the field is perfectly confined within the broad-

area waveguide. The real refractive $n_0(x)$ index and the gain $g_0(x)$ are assumed to be uniform with values n_0 and g_0 inside the well. The corresponding wave equation to be solved is similar to an eigenvalue problem. In this simple case, the *unperturbed* solutions (eigenvalues), $\psi_m(x)$, to the problem are the solutions to the well-known infinite square potential well problem [10]:

$$\begin{aligned} \psi_m(x) &= \frac{1}{\sqrt{x_0}} \sin\left(\frac{m\pi x}{2x_0} + \frac{m\pi}{2}\right) \\ \psi_m(x) &= 0 \quad \text{for} \quad |x| > x_0\,, \end{aligned} \tag{2.14}$$

where m again denotes the mode number. Thus $\psi_m(x)$ describes the near field distribution of the BAL modes. In [10], these solutions are denoted the unperturbed broad-area modes and their propagation constants (eigenvalues) are given by:

$$\beta_m = \tilde{n}_m k_0 = n_m k_0 - i\frac{g_0}{2}\,, \tag{2.15}$$

where $\tilde{n}_m$ is the complex refractive index for the m^{th} mode. The real refractive index is given by $n_m = [n_0 - m^2\pi^2/(4k_0^2x_0^2)]^{1/2}$ and we have used the assumption that modal gain, $g_m \simeq g_0$ since we have $k_0 n_m \gg g_m$, i.e. the small deviations in modal gain may be ignored.

The far field of the BAL modes may be obtained as the Fourier transform of the near field in 2.14 i.e. [38]:

$$\begin{aligned} FT\{\psi_m(x)\} =& \frac{\sqrt{x_0}}{2\pi}[\exp\left(i\frac{(m-1)\pi}{2}\right)\operatorname{sinc}\left(\frac{m\pi}{2} - k_0x_0\theta\right) \\ &+ \exp\left(i\frac{-(m-1)\pi}{2}\right)\operatorname{sinc}\left(\frac{m\pi}{2} + k_0x_0\theta\right)]\,, \end{aligned} \tag{2.16}$$

where the radiation angle in radians with respect to the longitudinal axis (z-axis), θ, is assumed small, such that $\sin\theta \simeq \theta$. Since the BAL mode is the product of a sine wave and a square function, its far field pattern mainly consists of two narrow lobes radiating at angles [10, 38]:

$$\theta_m = \pm\frac{m\pi}{2k_0x_0} = \pm\frac{m\lambda_0}{4x_0}\,, \tag{2.17}$$

where the plus sign refers to the "positive" lobe and the minus sign refers to the "negative" lobe. The fundamental mode ($m = 1$) is single-lobed.

Though the unperturbed resolution of the lateral modes is not accurate, and does not take into account the gain and index gratings, it reveals some of the most important aspects of BAL modes for the purpose of this work. The spatial separation between the modes, which is apparent from Eq. (2.17), allows for discrimination between them e.g. with spatial filters. This is a technique which is used frequently in **Papers I-V** and it will be discussed in chapter 3.

The perturbed broad-area model

In the perturbed broad-area model [10], two perturbations are initially induced in the effective index profile. These are (a) a periodic modulation of the gain and (b) a modulation in the real refractive index originating from the carrier induced index change, due to the antiguiding effect. Eq. (2.10) describes the coupling between these two effects, which are accounted for by introducing a sinusoidal perturbation to the change in complex index:

$$\Delta\tilde{n}(x) = (-1)^N \frac{\Delta g}{2k_0}(\beta_c + i)\cos(\frac{\pi N x}{x_0}), \qquad (2.18)$$

where N denotes the number of stripes, Δg is half of the amplitude of the gain perturbation and $i^2 = -1$. The factor $(-1)^N$ ensures that the gain is minimum in the center of the device for even values of stripes and maximum for odd values. Equation 2.18 thus describes a gain and index grating along the lateral axis of the laser.

Temperature variations across the laser width may be included as a perturbation. The temperature perturbation is purely real and it does not affect the gain of the lateral modes. It does, however, change the mode envelope and in the far field it shows as small lobes that are usually less than 1% of the main lobes [38]. The temperature has negligible effect on the position of the far field lobes, and we chose to ignore it in the present discussion. The overall result of the perturbations is a broadening of the far field lobes in terms of side-lobes originating from the gain, index and temperature variations.

As noted earlier, to find the lateral modes, the wave equation has to be solved with the index change (Eq. (2.18)) inserted. The presentation of the full solution is beyond the scope of this thesis, and the reader is referred to Refs. [10] and [38] for a complete description. Here we settle with the unperturbed solution to the problem, from which the main features of the lateral radiation can be resolved.

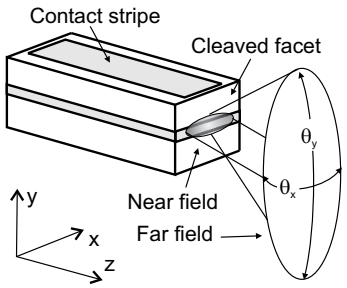

Figure 2.9. *The optical near field on the output facet is transformed by diffraction into the far field intensity distribution radiated at angles θ_x (slow/low coherence axis) and θ_y (fast/high coherence axis) with respect to the optical axis.*

2.5.3 High and low coherence axes

To summarize on the spatial mode pattern of the laser diode emission, each spatial mode, $\Phi_m^{tot}(x,y)$, of the diode laser is a multiplication of the transverse $\phi_0(y)$ and the the lateral $\psi_m(x)$ contributions, i.e.

$$\Phi_m^{tot} = \phi_0(y)\psi_m(x)\,. \tag{2.19}$$

In general several spatial modes are excited, and the resulting field is formed by a superposition of them. However, as mentioned previously, the transverse part, $\phi_0(y)$, usually only consists of the fundamental mode, so they differ only in lateral behavior, $\psi_m(x)$. Thus, the spatial coherence is very different in the two directions, which are often denoted the *high* (y) and the *low* (x) coherence axes, respectively. Sometimes the notations *fast* (y) and *slow* (x) axes are also used, referring to the fast and slow divergence of the emission in the two directions (see Fig. 2.9).

2.5.4 Astimatism

Due to the different guiding mechanisms in the lateral and the transverse directions, BALs suffer from astigmatism. This means that the beam waists in the two directions are not coinciding and that their far field angles θ_x and θ_y differ, see Fig. 2.9. In the narrow transverse direction, which typically has a dimension of $d \lesssim 1\,\mu$m, the waist is located on the output facet, while, in the broader lateral direction, which may be several hundreds of microns wide, the waist is located behind the output facet. The longitudinal astigmatism results in the need for cylindrical optics and/or anamorphic prism pairs in order to collimate the laser and/or re-image the junction. For gain-guided diode lasers, the astigmatism may be as large as $30 - 50\,\mu$m [39].

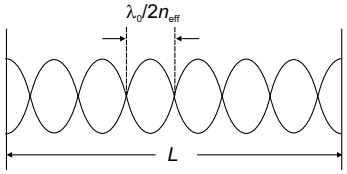

Figure 2.10. *Fabry-Perot resonator with cavity length L and standing wave with $q = 7$ nodes. The wave propagates in a waveguide with refractive index n_{eff} such that the distance between two neighboring nodes is $\lambda_0/2n_{eff}$, where λ_0 is the vacuum wavelength.*

2.5.5 Spectral properties of diode lasers

For high-power diode lasers, Fabry-Perot resonators are used. This type of resonator is shown in Fig. 2.10, which depicts two mirrors, corresponding to the cleaved and coated facets of the diode laser. The active semiconductor material, with unpumped refractive index n_{eff}, is situated in between the mirrors, which are separated by a distance L. Several longitudinal modes are allowed to oscillate, since the high-power diode laser has no mechanism for discrimination of modes and since spatial hole-burning permits the simultaneously oscillation of many modes. The longitudinal mode spacing, $\Delta\lambda_{FP}$, also denoted the *free spectral range*, may be found by noting that the cavity length is given by (see Fig. 2.10)

$$L = q\frac{\lambda_0}{2n_{eff}}\,. \tag{2.20}$$

where q is the number of nodes of the standing wave (the order of the longitudinal mode), and λ_0 is the vacuum wavelength. According to Eq. (2.20), an increase of q by 1, e.g. from q_n to q_{n+1}, switches to the next resonant value for λ_0. We thus have for the free spectral range:

$$\lambda_{FP} = \frac{2n_{eff}L}{q_n q_{n+1}} \approx \frac{2n_{eff}L}{(2n_{eff}L/\lambda_0)^2} = \frac{\lambda_0^2}{2n_{eff}L}\,. \tag{2.21}$$

where we have used $q_1 \approx q_2$. The refractive index for GaAlAs is approximately $n_{eff} \approx 3.6$, so for $\lambda_0 = 810\,\text{nm}$ and $L = 1\,\text{mm}$, we obtain a longitudinal mode spacing of $\Delta\lambda_{FP} \approx 0.1\,\text{nm}$. The spectral bandwidth (FWHM) of a typical diode laser is $\Delta\lambda \approx 1-2\,\text{nm}$, i.e. 10-20 longitudinal modes may oscillate simultaneously. Each longitudinal mode contains a number of spatial modes. Since the various spatial modes all oscillate with slightly different oscillation frequencies, these frequencies will be observed as substructures in the Fabry-Perot modes. The spatial mode spacing, i.e. the difference in resonant wavelength for two adjacent spatial modes is typically in the range $0.01 - 0.03\,\text{nm}$ [40, 41].

2.6 Pulsing diode lasers

By modulating e.g. the injection current, high peak powers may be obtained, which have advantages in a lot of areas such as cutting, welding, and various medical applications including tissue cutting and evaporation. In second harmonic generation (SHG) of new frequencies, pulsed lasers are very interesting since the power of the frequency doubled light depends quadratically on the power of the incoming light at the fundamental frequency. Unlike Q-switched or mode-locked lasers, where a large amount of energy is accumulated inside the gain medium before it is released in a huge pulse, pulsed diode lasers are usually realized by direct current modulation. Since the lifetime of the carriers is low, diode lasers do not store energy.

2.6.1 Fundamentals of pulsed diode lasers

Usually a periodic sequence of laser pulses are considered when lasers operate in pulsed mode. In Fig. 2.11 a few laser pulses are plotted as a function of time. The frequency f, or the repetition rate, of the sequence is determined from the period, T, as

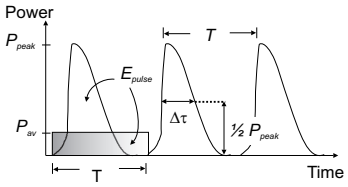

Figure 2.11. *Periodic laser pulses as a function of time. P_{peak} is the peak power, P_{av} is the average power, E_{pulse} is the energy of each pulse, T is the period of the pulse train, and $\Delta\tau$ is the pulse duration.*

$$f = \frac{1}{T}\,. \tag{2.22}$$

To determine the relative part of the time that the laser is *on*, we use the relation between the pulse duration $\delta\tau$ and and the period of the pulse train. This quantity is denoted the duty cycle (DC) of the pulsed laser:

$$DC = \frac{\Delta\tau}{T}\,. \tag{2.23}$$

The duty cycle of diode lasers is usually rather low. consider e.g. a diode laser emitting 100 ns pulses with a repetition rate of 1 kHz, equivalent to a period of 1 ms. this yields a duty cycle of $DC = 100 \times 10^{-9}\,\mathrm{s} \cdot 1 \times 10^{3}\,\mathrm{s}^{-1} = 1 \times 10^{-4} = 0.1\,{}^{0}/_{00}$, i.e. the laser only emits radiation during 0.1 thousands of the time. If in stead the repetition rate was as low as 50 Hz, which is not uncommon in medical purposes, the DC would be as low as $0.005\,{}^{0}/_{00}$, if the pulse duration of 100 ns is maintained.

The average power P_{av} of a pulsed laser is defined as the power of a continuous laser that would emit the same amount of energy per second as the pulsed laser. The amount of energy E_{pulse} carried by each pulse (see Fig. 2.11) is given by the relation between the average power and the frequency, i.e.

$$P_{av} = E_{pulse} \cdot f\,, \tag{2.24}$$

and the peak power, P_{peak} of the pulses can be expressed by

$$P_{peak} = \frac{E_{pulse}}{\Delta\tau} = \frac{P_{av}}{\Delta\tau f} = \frac{P_{av}}{DC}\,. \tag{2.25}$$

Pulsed diode lasers ususally operate with a maximum pulse duration limited to 100-200 ns and a DC not exceeding 1-2 %. There are certain important issues to take into account when pulsing a diode laser. These are summarized in sections 2.6.2-2.6.3 below.

2.6.2 Impedance

One of the fundamental principles involved when pulsing diode lasers is impedance matching. Impedance is a measure of how much a device resists the flow of an AC signal. It is similar to resistance, which is how much a device resists the flow of a DC signal. It is a measure in Ohms of the degree to which an electric circuit resists the flow of electric current when a voltage is impressed across its terminals. Impedance is expressed as the ratio

of the voltage impressed across a pair of terminals to the current flow between those terminals.

When a laser diode is in "on"-mode it represents a low impedance, while in "off" mode it represents a high impedance. Modulation signals may be an incentive to an impedance mismatch at the laser diode and be reflected back toward the source. If the reflected energy is not absorbed by the source, undesirable effects can occur [42]. This may cause the light from the laser diode to show extra detail depending on cable length, pulse width, and impedance mismatches. Impedance mismatches may also overdrive or reverse bias the laser diode, possibly causing damage. It is thus important to match the impedance of the lead to the impedance of the diode. This may be done simply by the insertion of a resistor in series with the diode. The impedance of the lead is typically around $50\,\Omega$, while the diode impedance is much less (maybe a couple of Ohms). If the laser diode has an impedance of $3\,\Omega$, the resistor should then have an impedance of $47\,\Omega$ [43].

2.6.3 Turn-on delay and relaxation oscillation

The turn-on time of a laser diode is typically 1 ns. Most laser diodes exhibit relaxation oscillations (ringing) in response to fast input current waveforms. This is illustrated in Fig. 2.12. For BALs, the ringing has about 0.5 ns period, and damps to steady state in 5 ns. Overshoot and undershoot can be as much as 50% to 80% of final steady state power [42]. Diode lasers typically have relaxation resonances of about 1-3 GHz, so intrinsically they can respond in less than a nanosecond. The frequency of these relaxation oscillations sets an upper limit to the frequency with which the laser can be modulated by varying the input current. This maximum modulation frequency is given by [44]:

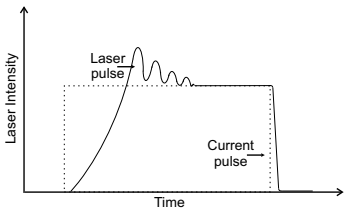

Figure 2.12. *Typical output from a laser diode when a square current pulse is applied. The period of the relaxation oscillations is typically around 0.5 ns.*

$$f_r = \frac{1}{2\pi}\sqrt{\frac{I/I_{th} - 1}{\tau_p \tau_s}} \tag{2.26}$$

where $\mathrm{I}/\mathrm{I}_{th}$ denotes the ratio of the injection current to its threshold value, τ_p is the photon lifetime and τ_s is the charge-carrier lifetime at threshold. For semiconductor lasers, typical values of τ_s is on the order of a nanosecond. For $\tau_p \simeq 3 \times 10^{-12}$ s and $\mathrm{I}/\mathrm{I}_{th} \simeq 2$, we calculate $\mathrm{f}_r \simeq 3$ GHz.

2.6.4 Experimental results

Initial experiments concerning pulsing of laser diodes have been performed. The experimental setup is shown in Fig. 2.13. The laser is a 200 μm, 4 W, 810 nm BAL (SLI-1169). It is collimated in the fast axis using an achromate with focal length $f = 4.5$ mm.

The laser diode is temperature controlled with a Peltier element and pulsed by direct current modulation using a pulsed current supply from Avtech Electrosystems (Av-107D-B). The average power is measured in front of the laser, and the peak power is calculated according to (2.25). The current pulse from the pulse generator, the signal measured by the power meter, and the voltage over the laser diode, are monitored using an oscilloscope. The parameters used in the experiment are a frequency of $f = 50\text{Hz}$ and a pulse duration of $\Delta\tau = 250\,\text{ns}$, which match the specifications required for a blue laser system for laser-induced fluorescence diagnostics at Lund University Medical Laser Centre [45].

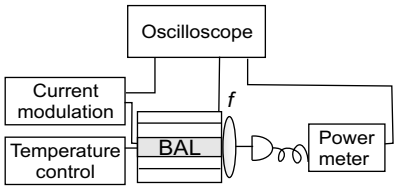

Figure 2.13. *Experimental setup for pulsing a 200 μm, 810 nm BAL. The temperature controlled BAL is pulsed by current modulation. The current pulse delivered from the pulsed current source, the voltage over the diode, and the signal measured by the power meter, are visualized by the oscilloscope. The test parameters are $f = 50Hz$ and $\Delta\tau = 250\,ns$.*

Fig. 2.14 shows experimental results in terms of peak and average powers as a function of current. As apparent from the figure, peak powers far exceeding the rated maximum CW power of 4 W (at $I = 4\,\text{A}$) are obtainable.

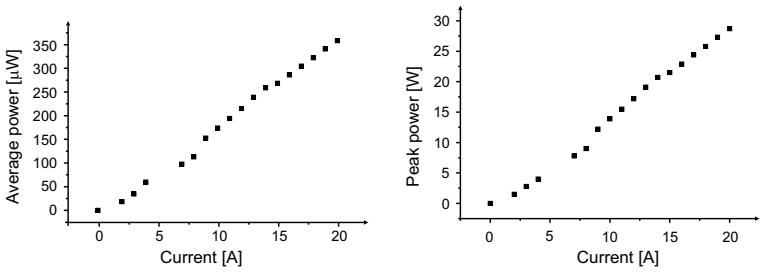

Figure 2.14. *Experimentally obtained average and peak powers from 200 μm, 810 nm BAL. The results are obtained with $f = 50Hz$ and $\Delta\tau = 250\,ns$.*

In the case in Fig. 2.14, the maximum peak power is approximately 30 W at a pump current of 20 A. However, the average power is rather low. This is due to the extremely low duty cycle of $DC = 50\,\text{Hz} \times 250\,\text{ns} = 1.25 \times 10^{-5}$. The average power may be increased by increasing the pulse duration and/or the frequency (see Eqs. (2.24) - (2.25)).

Unfortunately this laser suffered from damage before the average power was increased. The reason for the damage is not completely clear, but it may be due to reverse biasing of the diode during the high-current pulsing. Fig. 2.15 shows a plot from the oscilloscope during 20 A current modulation with pulse duration $\Delta t = 500$ ns. The upper track (a) shows the signal from the current modulator to the diode, the middle (b) shows the voltage over the diode and the lowest track (c) is the signal measured by the power meter, i.e. the output power from the diode. From (b) a voltage undershoot of approximately 3 V is observed. The overshoot reaches about 13 V and the steady-state voltage is approximately 4 V. The laser front facet was investigated and showed no signs of damage, so the damage is most likely due to some electrical phenomenon. However, this problem remains to be thoroughly investigated.

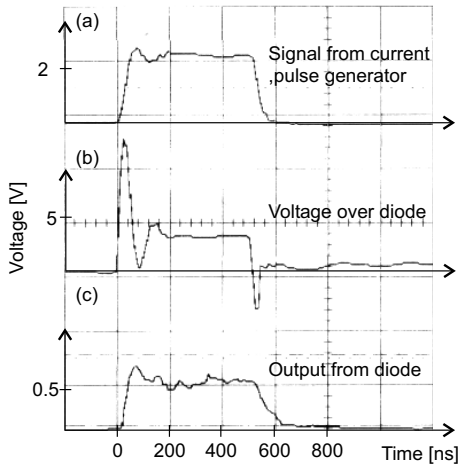

Figure 2.15. *Plots from the oscilloscope in Fig. 2.13 showing (a) The signal from the current modulator, (b) The measured voltage over the diode, and (c) The output power from the diode. The results are obtained with $I = 20\,A$ and $\Delta\tau = 500\,ns$.*

Chapter 3

External-cavity diode lasers

This chapter serves as a brief overview of the external cavity techniques that are used for improvement of the spatial and/or temporal coherence properties of laser diodes. Only off-axis configurations are considered, in which mode selection occurs using asymmetrical feedback of only part of the intensity distribution in the far field. One of the lobes in the double-lobed far field is selected by spatial filtering and fed back into the laser diode using an external reflector. This is in contrast to on-axis configurations, where the entire far field radiation is directed towards the external reflector. In order to improve the temporal coherence, means for spectral filtering must be included in the cavity. In this chapter different external reflectors and configurations are considered, and typical emission characteristics, which have been measured experimentally during this Ph.D. work, of the discussed external-cavity laser diodes are provided.

3.1 Single lobe far field formation

Fig. 3.1 shows the off-axis self-injection locking scheme. One of the far field lobes of a single BAL mode, mode number m, is externally injected back into the active region at an angle $-\theta_m$ by an external reflector. The reflected beam propagates towards the laser back facet, where it is reflected before it enters the front facet and (partly) leaves the laser in the angle $+\theta_m$. Propagation through the laser gain medium by multiple reflections amplifies the lobe in the positive angle, which constitutes the output. This scheme thus leads to a single-lobed far field profile radiated at angle $+\theta_m$. This mechanism is explained by the model suggested by Pillai [46], which furthermore suggests that the output lobe is not true single-lobed, but rather consists of an overlap of the central mode with its nearest neighbors, i.e. positive angle lobes of modes $m-1$ and $m+1$. Due to the spatial overlap of the modes, they cannot be

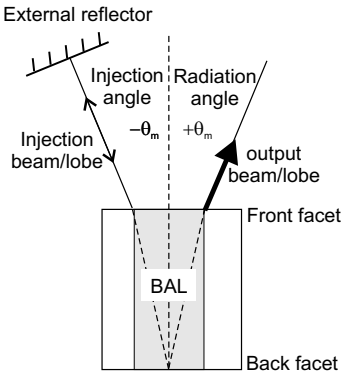

Figure 3.1. *The off-axis self-injection locking scheme. One of the far field lobes of a single BAL mode is reflected back at angle $-\theta_m$ into the laser by an external reflector. After reflection at the back facet, the amplified lobe leaves the front facet as the output at the opposite angle.*

completely discriminated by a spatial filter and thus the modes contributing to the single-lobed output are weighted according to their spatial overlap with the mode m addressed by a spatial filter (see next section).

3.2 Spatial mode filtering in the Fourier plane

Various kinds of external reflectors, such as mirrors, diffraction gratings, phase conjugate crystals, or combinations thereof, may be applied in an external-cavity setup. Fig. 3.2 shows a side view of the basic scheme for the external-cavity laser diodes considered in this Ph.D. work. The coordinate system represents the lateral (x), the transverse (y), and the longitudinal (z) axes, respectively. Typically, the laser is collimated using two lenses, L_1 and L_2, with focal lengths f_1 and f_2. L_1 is inserted at a distance f_1 from the BAL emission facet, thereby collimating the transverse direction. At the same time L_1 generates a far field plane, FF, for the lateral direction in its front focal plane. L_2 collimates the beam in the lateral direction and generates an image of the far field plane, FF, in the plane FF^* at distance s_2. The distance s_2 is determined by f_2 and the distance s_1 between FF and L_2 through the Lensmaker's equation [47]:

$$\frac{1}{s_1} + \frac{1}{s_2} = \frac{1}{f_2} \tag{3.1}$$

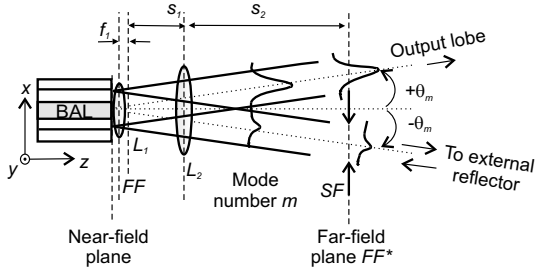

Figure 3.2. *Side view of the basic configuration and experimental setup for the off-axis external-cavity laser diodes considered in this work. The external reflector may be a conventional mirror, a grating, a phase conjugate crystal or a combination of such elements. L_1, L_2: Collimating lenses; f_1: Focal length of L_1; FF, FF^*: Far field planes; SF: Spatial filter; x, y, and z: Lateral, transverse, and longitudinal axes. The mode number m radiates its lobes at far field angles $\pm\theta_m$.*

As discussed in section 2.5.2, different spatial modes radiate their lobes at different angles. In FF^*, where the intensity distribution of mode number m, is double-lobed and radiated at angles $\pm\theta_m$ (see Eq. (2.17) and Fig. 3.2), a spatial filter SF can be inserted to allow for one of the lobes to reach the external reflector.

This "feedback lobe" is thus reflected back into the active layer where it is amplified. The other lobe serves as the output from the system. By careful filtering, this scheme may result in an almost diffraction limited output (see e.g. [48]). However, since several longitudinal modes oscillate, the spatial filtering will in general not lead to an improvement of the spectral properties of the laser diode. In order for this to occur, a spectral filter, such as an etalon, must be included in the cavity. Single spatial and longitudinal mode operation may be achieved by appropriate use of spatial and spectral filtering or by highly selective spectral filtering alone. The spatial and temporal behavior of the external-cavity laser diode shown in Fig. 3.2 may be measured by inserting a beam splitter plate after L_2 thereby extracting reflections for beam diagnostics. These reflections may also be used for alignment purposes.

3.3 External cavity modes

The external reflector will lead to oscillation of external cavity modes, which have their own set of resonance frequencies. The length of the external cavity, L_{ext}, is in general much longer than the length of the semiconductor laser cavity itself, such that the external cavity modes are closely spaced and form a continuum around each longitudinal mode of the laser cavity itself. The mode spacing of the external cavity modes is given by $c/2L_{ext}$, where c is the speed of light. A single mode laser exposed to optical feedback will in general suffer from a broadening of the spectral bandwidth, and thus a reduction of coherence length, due to the appearance of external cavity modes [49].

3.4 Feedback mechanisms

Various external reflectors can be used. In this section, only a few will be mentioned, which have been applied to more or less extent during the experiments in this Ph.D. work.

3.4.1 Mirror feedback

When using an ordinary mirror as the external reflector, nearly diffraction limited emission may be obtained (see e.g. [38, 48, 50–52]). Fig. 3.3 shows the far field intensity distributions with (solid) and without (dashed) conventional mirror feedback as a function of lateral radiation angle θ according to the setup in Fig. 3.2. The intensity profiles are measured by inserting a beam splitter after the collimating lenses. The beam splitter extracts a reflection in which a beam scanner (Melles Griot SuperBeamAlyzer) is inserted at a distance corresponding to the far field plane. The results are

obtained experimentally using a 3 W, 200 μm wide (lateral direction), 810 nm BAL from Coherent Inc.

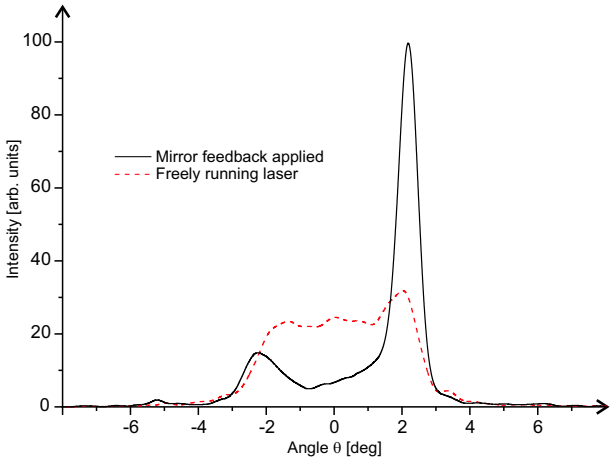

Figure 3.3. *Intensity distribution in the far field from 200 μm, 810 nm BAL with (solid) and without (dashed) spatial filtering and feedback from a conventional mirror.*

From the figure it is observed that the intensity profile assumes the asymmetrical, double-lobe in the far field, when spatial filtering and mirror feedback are applied. The high-intensity lobe constitutes the output from the system and the small lobe is the feedback lobe. The width (FWHM) of the output lobe is 0.71° corresponding to 2.6 times the diffraction limit [38]. In comparison, the freely running laser is 17 times the diffraction limit. The spectral behavior of the laser is not changed significantly when conventional mirror feedback is applied (see e.g. [53]).

3.4.2 Grating feedback

Littrow configuration

The external reflector in Fig. 3.2 may be a diffraction grating arranged in a Littrow configuration [54] and otherwise unchanged from the mirror-feedback configuration. In the Littrow configuration, the first diffraction order is sent directly back into the laser and the zeroth order is lost, see Fig. 3.4. With this configuration, the spatial intensity distributions in the far field resembles the profiles obtained with mirror feedback, as expected. Fig. 3.5 shows the measured intensity distributions in the far field from a grating feedback setup with a similar laser as the one used in the mirror feedback experiment described above. The grating is a ruled diffraction grating with 1200 lines/mm. The FWHM of the output lobe is 0.66° corresponding to 2.4 times the diffraction limit, or a factor of 7 less than than the freely running profile. Due

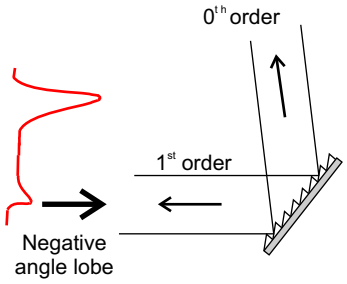

Figure 3.4. *Littrow configuration. The first diffracted order is directed back into the laser and the zeroth order is lost.*

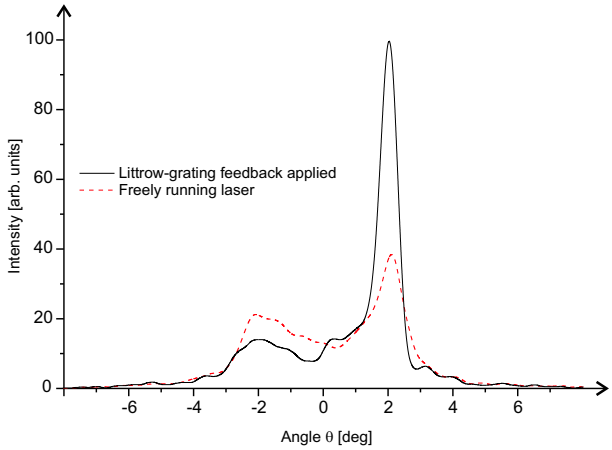

Figure 3.5. *Intensity distribution in the far field from a 3 W, 200 µm, 810 nm BAL with (solid) and without (dashed) spatial filtering and feedback from a conventional mirror.*

to the dispersion of the grating, this setup introduces a spectral filtering. This can be seen e.g. in Ref. [53], where a narrowing of the spectrum from approximately 1.5 nm to 0.3 nm is observed. By tilting the grating, the center wavelength of the emission may be tuned several nanometers.

Littman configuration

The grating may also be arranged in a Littman configuration [55], where the first diffraction order is directed to an external mirror. From here, it is directed back onto the grating where it is diffracted a second time before it reenters the diode, see Fig. 3.6. As expected, the spatial results with this configuration are comparable to the results obtained with mirror feedback and Littrow-grating feedback. Due to the second diffraction, the spectrum may be narrowed more with the Littman configuration as compared to the Littrow configuration. As before, the wavelength may be tuned several nanometers by rotation of the grating. This is observed in Fig. 3.7, which shows the measured spectra from a laser diode in an asymmetrical Littman configuration, i.e. the grating is placed in the Littman configuration, but only one of the far field lobes is reflected, as indicated in Fig. 3.2. The spectrum of the freely running laser (low intensity, dark curve) has a bandwidth (FWHM) of 1.2 nm, which narrows down to approximately 0.1 nm when spatial filtering and Littman-grating feedback are applied (high intensity, single-peaks). When using an on-axis configuration, where all the far field radiation is collected and directed towards the external reflector, a stronger coupling between the diode and the external reflector is obtained. This lead to tuning ranges exceeding several

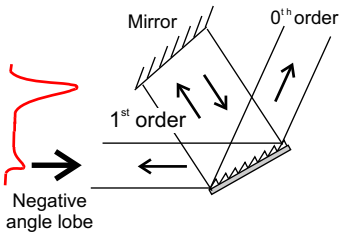

Figure 3.6. *Littman configuration. The first diffracted order is directed to an external mirror from where it is directed back onto the grating before it reenters the diode laser.*

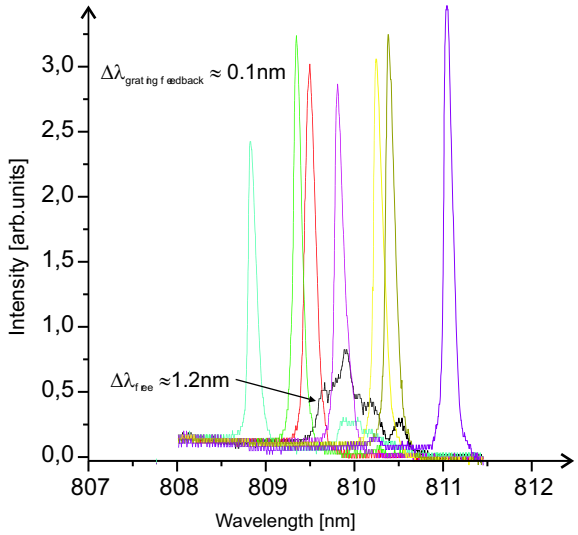

Figure 3.7. *Measured spectra from the freely running (low intensity, dark curve) and the Littman grating-feedback laser (high intensity, single-peaks). The spectrum from the feedback laser can be tuned by rotating the grating. The laser is a 3 W, 200 μm, 810 nm BAL and the grating is a ruled diffraction grating with 1200 lines/mm.*

tens of nanometers (see e.g. [56]). However, such systems lack the possibility to extract a large fraction of the laser beam with a high spatial coherence as well.

Simultaneous feedback from the first and the zeroth order of a grating

The spatial and temporal coherence of laser diodes may be improved by using simultaneous feedback from the first diffracted and the zeroth reflected order of a diffraction grating. The grating is arranged in a configuration similar to a Littman configuration, but in addition to feedback from part of the first order, part of the zeroth order is also coupled back into to the laser. For experimental setup, see **Paper III** [57]. With this method, the spatial coherence is controlled by adjusting the filtering of the zeroth order feedback, and the spectral coherence is controlled by adjustment of the first order feedback. This configuration improves the spectral bandwidth of the laser from approximately 1.2 nm to below 0.1 nm [57]. The spatial, and temporal properties of a laser diode in this double-grating feedback configuration is shown and described in detail in **Paper III**.

3.4.3 Phase conjugate feedback

A phase conjugate crystal may be used as the external reflector in an external-cavity laser diode system [58–60]. Phase conjugate crystals may be arranged in the self-pumped Cat geometry [61], such that no additional mirrors or pump beams are needed. There are some advantages of using phase conjugate feedback over conventional feedback, such as mirror or grating feedback. The phase conjugate mirror is self-aligning and provides a suitable feedback signal independent of the external cavity length and aberrations due to imperfect components (distortion correction). However, phase conjugate crystals are expensive and less robust than ordinary mirrors or gratings. Furthermore, their reflectivity is often low and the spatial filter may have to be partly removed in order for the phase conjugation to start up after the laser system has been turned off. They are well suited for research purposes, but maybe less suited in a commercial product. Inclusion of a Fabry-Perot etalon in such a cavity can lead to true spatial and spectral single-mode operation of the laser diode [53, 62].

Various combinations of the above reflectors may form other possibilities for configurations, such as a grating in a Littman configuration where the Littman mirror is a phase conjugate crystal [63].

3.5 Single lobe output formation without spatial filtering

Experiments have shown that a single-lobed output can occur without the incorporation of a spatial filter in the external cavity setup. This observation indicates that a mode selective mechanism occurs inside the gain medium of the laser diode cavity itself. Fig. 3.8 shows the intensity profile in the far field of a laser diode exposed to phase conjugate feedback from a Rh:$BaTiO_3$ crystal. The laser is a 200 μm, 3 W, 810 nm diode which was originally implemented in the configuration shown in Fig. 3.2. However, the spatial filter was removed when the results in Fig. 3.8 were recorded. The asymmetrical double lobe is clearly present even though no spatial mode selection has been applied. The FWHM of the high-intensity lobe is 0.72° or 2.6 times the diffraction limit, which corresponds to an improvement of a factor of 7 compared to the freely running laser. Fig. 3.9 show results from a similar experiment, where the external reflector is a Fabry-Perot etalon placed in the focal plane of a $f = 40$ mm plane convex lens. Here the output lobe is 2.1 times the diffraction limit (0.58° FWMH), which is again a factor of 7 less than the freely running profile. Experiments with ordinary mirror feedback have shown similar behavior. This is presented in **Paper VI**, which provides a theory that has been developed in order to explain these findings. The theory is

based on the presence of self-pumped degenerate four-wave mixing in the semiconductor amplifier. The interacting waves inside the active medium form gain and index gratings. These gratings lead to selective amplification of one spatial mode and suppression of other modes.

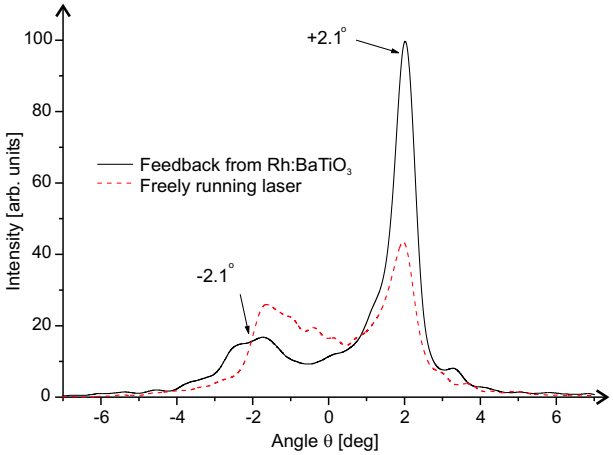

Figure 3.8. *Intensity distribution in the far field from a 200 µm, 810 nm BAL with (solid) and without (dashed) feedback from a Rh:BaTiO₃ crystal. No spatial filtering applied.*

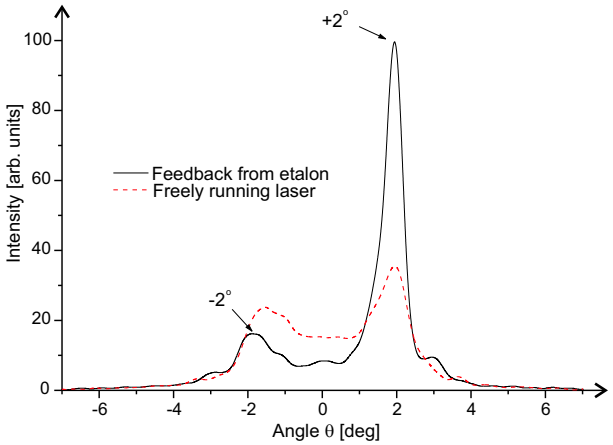

Figure 3.9. *Intensity distribution in the far field from a 200 µm, 810 nm BAL with (solid) and without (dashed) feedback from an etalon placed in focal plane of $f = 40$ mm lens. No spatial filtering applied.*

Chapter 4

Second harmonic generation

The invention and experimental realization of the laser in 1960 [64, 65] lead to a major breakthrough for nonlinear optics. The high intensities obtainable with a laser was already in 1961 demonstrated to generate second harmonic frequencies in an experiment with a ruby laser and quartz [66]. This was the beginning of nonlinear optics, which ever since have been intensively explored. This chapter deals with second harmonic generation (SHG), which is one of the most applied second order nonlinear effects, since it opens the possibility of creating lasers at twice the fundamental frequencies.

4.1 Basic principles of SHG

Light propagation in matter can be described through the electric and magnetic field vectors $\mathbf{E}$ and $\mathbf{H}$ and the corresponding electric and magnetic flux densities, $\mathbf{D}$ and $\mathbf{B}$ through Maxwell's equations [67]:

$$\nabla \times \mathbf{E} = -\partial \mathbf{B}/\partial t \tag{4.1}$$

$$\nabla \times \mathbf{H} = \mathbf{J} + \partial \mathbf{D}/\partial t \tag{4.2}$$

$$\nabla \cdot \mathbf{D} = \rho \tag{4.3}$$

$$\nabla \cdot \mathbf{B} = 0 \tag{4.4}$$

where $\mathbf{J}$ and ρ represent the current density vector and the charge density, respectively. The flux densities $\mathbf{D}$ and $\mathbf{B}$, which arise in response to the electric and magnetic fields propagating in the medium, are expressed in the constitutive relations, as [67]:

$$\mathbf{D} = \epsilon_0 \mathbf{E} + \mathbf{P} \tag{4.5}$$

$$\mathbf{B} = \mu_0 \mathbf{H} + \mathbf{M} \tag{4.6}$$

$$\mathbf{J} = \sigma \mathbf{E} \tag{4.7}$$

where ϵ_0 and μ_0 are the free space permittivity and permeability, respectively, and σ is the conductivity of the medium. The induced polarization $\mathbf{P}$ and magnetization $\mathbf{M}$ are defined as induced electric and magnetic dipole moment pr. unit volume, respectively. In the following $\mathbf{M}$ is assumed to be zero.

Maxwells equations can be used to obtain a wave equation that describes how the optical field propagates inside the medium. First take the curl of Eq. (4.1):

$$\nabla \times \nabla \times \mathbf{E} = -\mu_0 \frac{\partial}{\partial t}(\nabla \times \mathbf{H}) \tag{4.8}$$

where Eq. (4.6) have been used and we have assumed a nonmagnetic material. We now use Eqs. (4.2), (4.5), and (4.7) to obtain

$$\nabla^2 \mathbf{E} = \mu_0 \sigma \frac{\partial \mathbf{E}}{\partial t} + \mu_0 \epsilon_0 \frac{\partial^2 \mathbf{E}}{\partial t^2} + \mu_0 \frac{\partial^2 \mathbf{P}}{\partial t^2} \tag{4.9}$$

where we have used the vector identity $\nabla \times \nabla \times \mathbf{E} = \nabla(\nabla \cdot \mathbf{E}) - \nabla^2 \mathbf{E}$ and assumed an isotropic media with no free charges ($\nabla \cdot \mathbf{E} = 0$). The wave equation (4.9) is valid for arbitrary time-varying fields and we will use it in the following to obtain a fundamental wave equation for propagation in a medium with nonlinear polarisation.

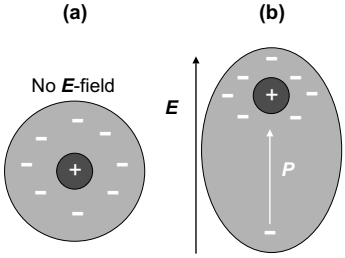

Figure 4.1. *Semiclassical model of an atom. a positive nucleus is surrounded by an electron cloud. (a) No field is applied, (b) The applied **E**-field slightly displaces the electron cloud so that a polarization **P** is induced.*

4.1.1 The nonlinear polarization

When a medium is exposed to light with the field vector $\mathbf{E}$, a polarization field $\mathbf{P}$ will be induced. Consider the simplified model in Fig. 4.1(a), where the nonlinear crystal is made up of atoms which we consider to be comprised of a positively charged nucleus surrounded by an electron cloud (depicted by the gray cloud with white minuses). In the equilibrium situation, there is no net polarization in the material and the centers of positive and negative charges coincide. Applying a light wave with frequency ω_1 to the material, the electric field $\mathbf{E}$ associated with that light wave exerts a force upon the electron cloud, which becomes distorted, Fig. 4.1(b). In this situation, the centers of positive and negative charges, becomes spatially separated, and a polarization is induced in the material.

For linear optical phenomena, the induced polarization is proportional to the applied field, i.e. a sinusoidally-varying electric field will induce a polarization that varies sinusoidally at the same frequency, see Fig. 4.2(a). However, if the light intensity is large, $\mathbf{P}$ may no longer depend on $\mathbf{E}$ in a linear manner, and a number of nonlinear phenomena may be excited. This situation is depicted

in 4.2(b). The induced polarization (lower part in black) can be decomposed into frequency components at higher harmonics of the original frequency ω_1. In the example in Fig. 4.2(b), $\mathbf{P}$ contains a component at the applied (fundamental) frequency (dashed), and at the second harmonic frequency $2\omega_1$ (gray). To describe the nonlinear effects, it is convenient to consider the i^{th} component of the induced nonlinear polarization as a power series expansion in the applied electrical field [68]:

$$P_i = \epsilon_0 \chi_{ij}^{(1)} E_j + 2\chi_{ijk}^{(2)} E_j E_k + 4\chi_{ijkl}^{(3)} E_j E_k E_l + ... \tag{4.10}$$

where summation must be made over repeated indices. $\chi^{(n)}$ is the n^{th} order complex susceptibility of the material and it depends on the frequencies of the $n+1$ interacting waves. The frequency dependency of $\chi^{(n)}$ indicates how the waves interact inside the nonlinear medium. E_j is the j^{th} component of the instantaneous, total electric field. This field is in general composed of a superposition of $n+1$ electrical fields, each with frequency ω_i [68]:

$$\mathbf{E}(\omega_i) = \frac{1}{2}\mathbf{A}(\mathbf{r},t)\exp[i(\omega_i t - \mathbf{k_i}\cdot\mathbf{r})] + c.c.\,, \qquad i = 1,2,...,n+1\,. \tag{4.11}$$

In Eq. (4.11), $\mathbf{A}(\mathbf{r},t)$ is the field amplitude, $\mathbf{k}_i$ is the wave vector, $\mathbf{r}$ is the direction of propagation, and *c.c.* is the complex conjugate.

The first term in Eq. (4.10) gives rise to the first-order, linear, phenomena, such as index of refraction. If $\chi_{ij}^{(1)}$ is complex, its imaginary part describes the light absorption. The linear phenomena does not cause the formation of new fields. The second-order term, which involves the square of the applied electric field, gives rise to the nonlinear effect which is important in the present work: SHG. It also leads to sum-frequency mixing, difference-frequency generation, linear electro-optic effect, and parametric mixing. Throughout this chapter, we will only consider SHG, i.e. we ignore the processes of sum/difference-frequency generation and assume $\chi^{(2)} = \chi^{(2)}(\omega_3 : \omega_1, \omega_2)$ with $\omega_1 = \omega_2 = \omega$ and $\omega_3 = 2\omega$. The third-order term, involving the cube of the electric field, leads to third-harmonic generation, quadratic Kerr-effect, and intensity dependent refractive index [68]. The latter effect is used in degenerate four-wave mixing, which is a method to generate phase conjugate wavefronts. Phase conjugate crystals were briefly discussed in chapter 3, where they were considered as phase conjugating mirrors in external cavities. In the following, we will concentrate on the second order term and SHG.

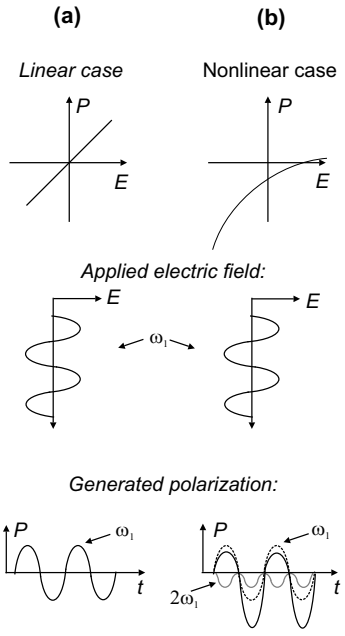

Figure 4.2. *The induced polarization may be a linear (a) or nonlinear (b) function of the incident field. In the former case, the generated polarization oscillates at the same frequency, ω_1, as the applied field (left). In the latter case (right), the generated polarization will contain frequency components at higher harmonics, here at the second harmonic (gray), of the original frequency (dashed).*

Frequencies of the nonlinear polarization

To clarify the appearance of higher-order frequencies in the nonlinear polarization, consider a monochromatic light wave propagating along z: $E_1(z,t) = \frac{1}{2}A_1 \exp[i(\omega_1 t - k_1 z)] + c.c.$ We rewrite, to obtain $E_1(z,t) = A_1 \cos(\omega_1 t - k_1 z)$. Now the (scalar) nonlinear polarization can be written (insertion into Eq. (4.10)) [69]:

$$\begin{aligned} P(z,t) =& \epsilon_0 \chi^{(1)} A_1 \cos(\omega_1 t - k_1 z) \\ &+ 2\chi^{(2)} [A_1 \cos(\omega_1 t - k_1 z)]^2 + ... \\ =& \epsilon_0 \chi^{(1)} A_1 \cos(\omega_1 t - k_1 z) \\ &+ \chi^{(2)} A_1^2 [1 + \cos(2\omega_1 t - 2k_1 z)] + ... \end{aligned} \tag{4.12}$$

where we have used the identity $\cos^2 A = \frac{1}{2}[1 + \cos(2A)]$. In the expression (4.12), we clearly recognize the appearance of the fundamental and the second harmonic contributions to the nonlinear polarization, as described above.

Wave propagation in nonlinear media

The polarization in Eq. (4.5) can, according to Eq. (4.10) be decomposed into a linear and a nonlinear ($\mathbf{P}_{nl}$) part:

$$\mathbf{P} = \epsilon_0 \chi^{(1)} \mathbf{E} + \mathbf{P}_{nl} \,. \tag{4.13}$$

Insertion of this expression for the polarization into the wave equation (4.9), results in the fundamental wave equation for propagation in a medium with nonlinear polarization [68]:

$$\nabla^2 \mathbf{E} = \mu_0 \sigma \frac{\partial \mathbf{E}}{\partial t} + \mu_0 \epsilon_0 \epsilon \frac{\partial^2 \mathbf{E}}{\partial t^2} + \mu_0 \frac{\partial^2 \mathbf{P}_{nl}}{\partial t^2} \,, \tag{4.14}$$

where $\epsilon = (1 + \chi^{(1)})$ is the linear part of the permittivity.

4.1.2 The d coefficient

Often *the nonlinear coefficient* d is used instead of the second-order nonlinear susceptibility $\chi^{(2)}$, $\chi^{(2)}_{ijk} = d_{ijk}$ [68, 69]. With this notation, the i^{th} component of the second-order polarization may be expressed as (second term in Eq. (4.10)):

$$P_i^{(2)} = 2 \sum_{j,k} d_{ijk} E_j E_k \,. \tag{4.15}$$

In general, the nonlinear coefficient is a 27-element tensor of the third rank. However, the number of independent elements of d_{ijk}

can be reduced considerably. Since the order of appearance of E_j and E_k in Eq. (4.15) is trivial and without physical significance, we have $d_{ijk} = d_{ikj}$. Since the j, k indices in $d^{(2)}_{ijk}$ are interchangeable, we are able to reduce the number of elements from 27 to 18, by introducing the contracted notation:

$$\begin{array}{cccccccc} jk: & 11 & 22 & 33 & 23,32 & 13,31 & 12,21 \\ l: & 1 & 2 & 3 & 4 & 5 & 6 \end{array} \tag{4.16}$$

With this notation we have $\chi^{(2)}_{ijk} = d_{ijk} \rightarrow d_{il}$, and Eq. (4.15) may be written in matrix form, as:

$$\begin{bmatrix} P_x \\ P_y \\ P_z \end{bmatrix} = \begin{bmatrix} d_{11} & d_{12} & d_{13} & d_{14} & d_{15} & d_{16} \\ d_{21} & d_{22} & d_{23} & d_{24} & d_{25} & d_{26} \\ d_{31} & d_{32} & d_{33} & d_{34} & d_{35} & d_{36} \end{bmatrix} \begin{bmatrix} E_x^2 \\ E_y^2 \\ E_z^2 \\ 2E_yE_z \\ 2E_xE_z \\ 2E_xE_y \end{bmatrix} [1+\cos(2\omega t)] \tag{4.17}$$

with $\mathbf{E} = (E_x, E_y, E_z)\cos\omega t$. The d-matrix given in Eq. (4.17) is for the least symmetric, triclinic, class-I crystals [69]. Usually, a high degree of symmetry is present, which limits the number of elements in d even more. For example, the *Kleinman symmetry* [70, 71] applies if all the frequencies involved in the nonlinear process are sufficiently different from any resonance frequencies of the material. This symmetry results in a further reduction in d from 18 to 10 elements. Moreover, certain orientations of applied electric fields may be equivalent to others, due to some regularity in the arrangement of the crystal. Such spatial symmetries reduce the number of independent elements in the d-matrix further.

4.1.3 The generated wave

When the nonlinear polarization is known (from Eq. (4.15)) we can determine the second-harmonic wave radiated by that source using Maxwell's equations. For second-order nonlinear effects, two light fields $\mathbf{E}_1(\omega_1)$ and $\mathbf{E}_2(\omega_2)$ interact through the nonlinear coefficient d_{il} to generate a third light field $\mathbf{E}_3(\omega_3)$. If we, for simplicity, assume that all waves propagate along the z-axis and that they are all polarized along the same direction, we may consider scalar fields of the form:

$$E_i(\omega_i) = \frac{1}{2}A_i \exp i(\omega_i t - k_i z) + c.c.\,, \;\; i = 1, 2, 3 \tag{4.18}$$

where the indexing i now refers to the numbering of the interacting waves. Taking the Laplacian of this field, yields:

$$\nabla^2 E_i = \frac{1}{2}\left(\frac{d^2 A_i}{dz^2} - 2ik_i\frac{dA_i}{dz} - k_i^2 A_i\right)\exp[i(\omega_i t - k_i z)] + c.c. \tag{4.19}$$

If we now apply the slowly varying envelope approximation:

$$|k_i^2 A_i| \gg \left|k_i \frac{dA_i}{dz}\right| \gg \left|\frac{d^2 A_i}{dz^2}\right|, \tag{4.20}$$

which is valid when the complex amplitude A_i only depends weakly on z, the wave equation (4.14) may, for stationary fields ($dA_i/dt = 0$), be reduced to a first order differential equation:

$$\begin{aligned}\frac{dA_i}{dz}e^{i(\omega_i t - k_i z)} + c.c. = &-\frac{1}{2}\sqrt{\mu_0/\epsilon_0\epsilon_i}\,\sigma_i A_i e^{i(\omega_i t - k_i z)} + c.c. \\ &+ i\sqrt{\mu_0/\epsilon_0\epsilon_i}\,\frac{1}{\omega_i}\frac{\partial^2 P_{nl}}{\partial t^2},\end{aligned} \tag{4.21}$$

where P_{nl} is the component of $\mathbf{P}_{nl}$ in the direction of the A_i-field, and where we have used $k_i = \omega_i\sqrt{\mu_0\epsilon_0\epsilon_i}$. The first term to the right is an attenuation term, which is often expressed in terms of an absorption coefficient: $\alpha_i = \sigma_i\sqrt{\mu_0/(\epsilon_0\epsilon_i)}$. For SHG, we have $\omega_1 = \omega_2 = \omega$ and $\omega_3 = 2\omega$. The component of the nonlinear polarization in the direction of the generated field $A_3 = A_{2\omega}$ is thus

$$P_{nl,2\omega} = \frac{1}{2}d_{\mathit{eff}}A_\omega^2 e^{i(2\omega t - 2kz)} + c.c., \tag{4.22}$$

where d_{eff} is the relevant element of the d_{il} matrix. Taking the second time-derivative of this component and insertion into Eq. (4.21) yields:

$$\begin{aligned}\frac{dA_3}{dz}e^{i(\omega_3 t - k_3 z)} + c.c. =& \frac{dA_{2\omega}}{dz}e^{i(2\omega t - k_3 z)} + c.c. \\ =& -\frac{1}{2}\sqrt{\mu_0/\epsilon_0\epsilon_3}\sigma_3 A_{2\omega}e^{i(2\omega t - k_3 z)} + c.c. \\ &- i\sqrt{\mu_0/\epsilon_0\epsilon_3}\omega d A_\omega^2 e^{i(2\omega t - 2kz)} + c.c.\end{aligned}$$

Division by $e^{i(2\omega - k_3 z)}$ and assuming that the medium is transparent at ω_3 ($\sigma_3 = 0$) finally yields for the second-harmonic field:

$$\frac{dA_{2\omega}}{dz} = -i\frac{\mu_0 c d_{\mathit{eff}}\omega}{n_{2\omega}}A_\omega^2 e^{i\Delta k z}, \tag{4.23}$$

where we have used $\sqrt{\mu_0/\epsilon_0\epsilon_3} = \mu_0 c/n_{2\omega}$, where c is the speed of light and $n_{2\omega}$ is the index of refraction at the second harmonic frequency and where $\Delta k = k_3 - k_2 - k_1 = k_{2\omega} - 2k_\omega$. In a similar way, we may find for the fundamental fields $A_1 = A_2 = A_\omega$ [68]:

$$\frac{dA_\omega}{dz} = -i\frac{\mu_0 c d_{eff}\omega}{2n_\omega} A_{2\omega}\tilde{A}_\omega e^{-i\Delta kz}\,, \tag{4.24}$$

where n_ω is the refractive index at the fundamental frequency, and the tilde denotes the complex conjugate. The coupled equations (4.23) and (4.24) are the fundamental equations describing SHG. When they are satisfied, the three waves in Eq. (4.18) with the conditions $\omega_3 = \omega_1 + \omega_2$ and $\omega_1 = \omega_2 = \omega$ are solutions to the Maxwell equations. In practice, the relevant d-element must be found from Eq. (4.17) and the equations (4.23) and (4.24) may be supplemented by the equivalent equations for the other spatial components.

Intensity of the generated second harmonic wave

For a crystal of length L and assuming that $A(\omega)$ does not depend on z (non-depleted pump approximation), Eq. (4.23) may be integrated to obtain

$$A_{2\omega} = -i\frac{\mu_0 c d_{eff}\omega}{n_{2\omega}} A_\omega^2 \frac{e^{i\Delta kL} - 1}{i\Delta k}\,. \tag{4.25}$$

The intensity $I_{2\omega}$ of the second harmonic wave is described by the numerical value of the Poynting vector $\mathbf{S} = (1/\mu_0)\,\mathbf{E} \times \mathbf{B}$ ($[\mathrm{S}] = \mathrm{W/m^2}$), and is thus found from $I = (1/2)n|A|^2/c\mu_0$ (with $1/c^2 = \mu_0\epsilon_0$) by insertion of (4.25) as:

$$I_{2\omega} = \frac{n_{2\omega}}{2c\mu_0}|A_{2\omega}|^2 = \frac{2\mu_0^3 c^3\omega^2 d_{eff}^2}{n_\omega^2 n_{2\omega}} I_\omega^2 L^2 \left(\frac{\sin(\Delta kL/2)}{\Delta kL/2}\right)^2\,, \tag{4.26}$$

where d_{eff} is in units of $\mathrm{As/V^2}$ (division by ϵ_0 gives the unit pm/V). Thus, the intensity of the second harmonic wave depends on the square of the intensity of the incident field I_ω^2 and the length L^2 of the nonlinear crystal. We note that L also appears in the sine function, i.e. the second harmonic intensity oscillates throughout the crystal. Such oscillations are referred to as Maker fringes [72, 73]. Furthermore, it is noted that in practical cases where the beam is often focused into the crystal, some constraint has to be applied to L. Long crystals will eventually cause the conversion efficiency to fall off, due to an increase in beam cross section. Later, we will see that when focused Gaussian beams are used, the conversion efficiency increases as the crystal length L rather than as L^2. For

highly efficient SHG, where A_ω is dependent on z, a more accurate expression than (4.26) must be used, which can be found from solving Eqs. (4.23) and (4.24). The parameter Δk is of particular interest. It is apparent from Eq. (4.26) that in order to have efficient SHG, we must have

$$\Delta k = k_{2\omega} - 2k_\omega = \frac{2\omega}{c}(n_{2\omega} - n_\omega) = 0 \tag{4.27}$$

which is the important phasematching condition in SHG. The importance of this condition is easily observed from a plot of the last term in Eq. (4.26), i.e. $\left(\frac{\sin(\Delta kL/2)}{\Delta kL/2}\right)^2 = \mathrm{sinc}^2(\Delta kL/2)$ as a function of $\Delta kL/2$, see Fig. 4.3. Methods to fulfill the condition (4.27) and thus accomplish phasematching are discussed in section 4.3.

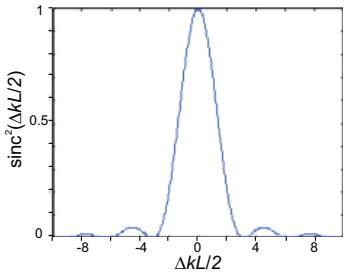

Figure 4.3. *The sinc^2 function. Phasematching is obtained when $\Delta k = 0$.*

4.2 Spatial confinement

According to Eq. (4.26), the intensity of the second harmonic light depends on the square of the intensity of the incident beam. Since intensity is power per unit area, one may expect that for a given power, the conversion efficiency from fundamental to second harmonic light could be maximized by confining the incident beam as tightly as possible. This could be achieved by focusing an incident laser beam with a short focal length. However, strong focusing lead to rapid diffraction, and the confinement of the beam to a small area, will not be maintained over a long length. Since the second harmonic intensity also depends on the nonlinear interaction length, there is a tradeoff between having both tight focusing and long interaction length. From these arguments, it may be expected that an optimal focusing in a given situation may exist. As will be apparent from section 4.2.1, this is in fact the case.

4.2.1 Boyd-Kleinman analysis for SHG with circular gaussian beams

In 1968, Boyd and Kleinman developed the analysis of SHG for focused, circular, gaussian beams [74]. In this section, the main results of their analysis will be summarized. The full derivation is beyond the scope of this thesis and the interested reader is referred to the original work.

Assume a circular, gaussian beam with an electrical field that has a radial distribution e^{-r^2/w_0^2}. The beam is focused to a waist w_0 at the center of a nonlinear crystal of length L. This is the fundamental beam and it may be characterized by its confocal parameter $b = 2\pi n_\omega w_0^2/\lambda_\omega$, where λ_ω is the wavelength of the fundamental beam and $\theta_0 = \lambda_\omega/(\pi n_\omega w_0)$ is the angle by which, the

beam diverges in the far field. The approach by Boyd and Kleinman is illustrated in Fig. 4.4. [69]. The nonlinear crystal is divided into slices of infinitesimal width dz and SHG takes place in each slice. In the observation plane, all the fields from the infinitesimal slices adds up, taking their respective phases into account, to the total second harmonic field. Since the fundamental beam is focused, the intensity of the second harmonic beam vary from slice to slice.

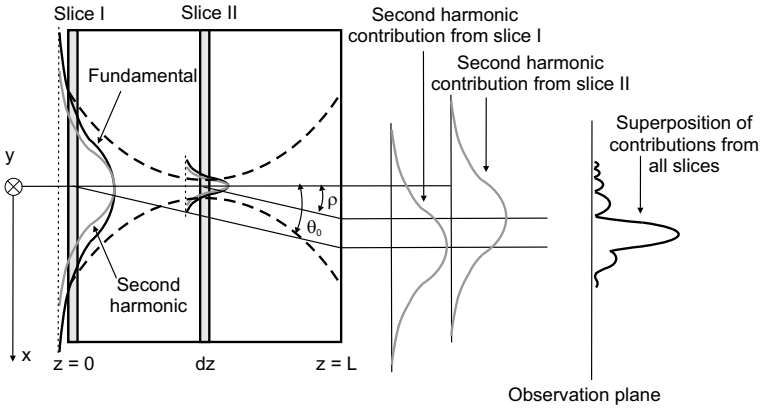

Figure 4.4. *The geometry in the analysis by Boyd and Kleinman [74]. A fundamental, Gaussian beam (black) is focused into a nonlinear crystal. The SHG takes place in each slice of width dz and adds up to the total field in the observation plane [69].*

It is sometimes necessary to have beam propagation along a direction at some angle with respect to the crystal axes in order to achieve phasematching at the wavelenght of interest (see section 4.3.1). If this is the case, the effect of birefringent *walk-off* must be taken into account, since the fundamental and the second harmonic beams propagates at a small angle ρ with respect to each other (see Fig. 4.4). This put a limit for the interaction length in the crystal, since the waves propagate away from each other. Furthermore, the second harmonic contributions to the field at the observation plane generated near the entrance of the crystal has a larger spatial displacement than the second harmonic fields generated near the crystal output. These dislocations result in a total second harmonic output which is distorted and thus no longer Gaussian (see Fig. 4.4).

All these effects are discussed in closer detail in Ref. [74]. Here we suffice with the main result (in SI units [69]), which expresses the second harmonic power (for $\Delta k = 0$):

$$P_{2\omega} = \frac{16\pi^2 d_{eff}^2}{\epsilon_0 c \lambda_\omega^3 n_{2\omega} n_\omega} P_\omega^2 e^{-\alpha' L} L h(\sigma, \beta, \kappa, \xi, \mu) \tag{4.28}$$

The expression is obtained from the intensity by integration over the area of a Gaussian beam. The nonlinear coefficient, d_{eff}, is now expressed in pm/V and $h(\sigma, \beta, \kappa, \xi, \mu)$ is the Boyd-Kleinman focusing factor, which must be evaluated in the individual case. The parameters in the argument are $\kappa = \alpha b/2$, $\sigma = b\Delta k/2$, $\beta = \rho/\theta_0$, $\xi = L/b$, and $\mu = (L - 2f)/L$, where α is a combined absorption coefficient (see below Eq. (4.21)), which describes the loss at both wavelengths, and $z = f$ is the position of the focus. If we neglect losses, and assume a focus in the center of the crystal, the focusing factor is reduced to $h(\sigma, \beta, 0, \xi, 0)$. We are interested in the behavior of h as the focusing is changed. Thus, we keep all the parameters fixed except for the confocal parameter b. Furthermore, we define a parameter $B = \rho\sqrt{Lk_\omega}/2 = \beta\sqrt{\xi}$, which only depends on fixed parameters, such that we can define $h(\sigma, B, \xi) = h(\sigma, B\xi^{-\frac{1}{2}}, 0, \xi, 0)$. This h can now be maximized by choosing an appropriate degree of focusing, $\xi = L/b$, and assuring that the phasematching condition is fulfilled by adjusting $\sigma = b\Delta k/2$. We now assume phasematching, such that $\sigma_m(B, \xi)$ is the value of σ that maximizes h for fixed B and ξ. The maximized value of h is then denoted $h_m(B, \xi) = h(\sigma_m, B, \xi) = h[\sigma_m(B, \xi), \beta\sqrt{\xi}, 0, \xi, 0]$. Calculated values of the maximized focusing factor $h_m(B, \xi)$ for different degrees of birefringence (B) is shown in Fig. 4.5.

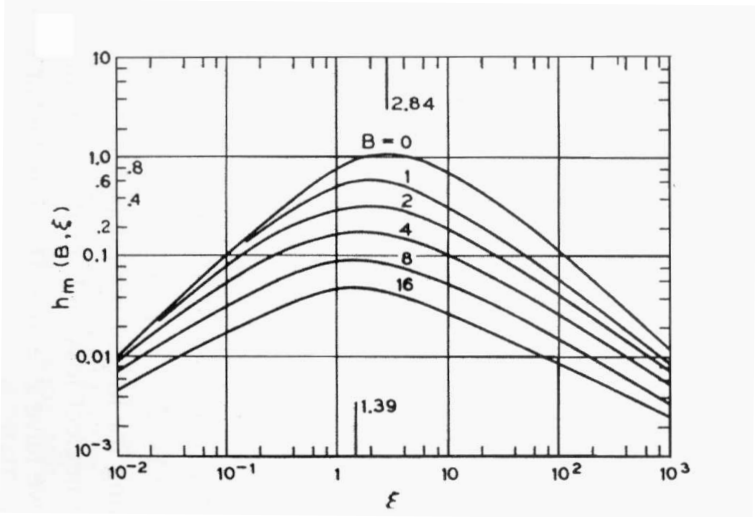

Figure 4.5. *The Boyd-Kleinman focusing factor h_m versus ξ for various values of B (From [74]).*

From this figure, we see that for each value of B (walk-off angle and crystal length), a maximum value of $\xi = \xi_m$ can be found. This value of ξ corresponds to a maximum value of h_m, such that $h_{mm}(B) = h_m[B, \xi(B)]$. We also note from the figure that as B

increases, ξ_m decreases, i.e. the optimal focusing is looser for the case of walk-off as compared to no walk-off ($B = 0$). Finally, it is observed that the maximum value of the focusing factor is a rapidly decreasing function of ξ, i.e. the second harmonic power decrease rapidly, as we move away from the optimal focusing condition.

A special case, is the case with no walk-off, $B = 0$. In this case $h_{mm} = 1.068$ and $\xi = 2.84$, i.e. the focusing condition is $b = L/2.84$ and Eq. (4.28) reduces to

$$P_{2\omega} = 1.068 \frac{16\pi^2 d_{eff}^2}{\epsilon_0 c \lambda_\omega^3 n_{2\omega} n_\omega} P_\omega^2 L \,, \tag{4.29}$$

for optimal focusing and neglecting absorption.

4.2.2 Extended analysis for SHG with elliptical Gaussian beams

The Boyd-Kleinman analysis summarized in the previous section applies to circular, Gaussian beams. However, sometimes the interacting beams are elliptical, which is especially the case for diode lasers. In 1975 Librecht and Simons [75] extended the theory of Boyd and Kleinman to include the case of elliptical, Gaussian beams. It turns out that for crystals displaying strong walk-off the second harmonic generation efficiency may in fact be optimized by the use of asymmetric focusing [75, 76]. The reason for this is the simultaneous ability to 1) increase intensity and thus SHG efficiency by tight focusing in the direction orthogonal to walk-off and 2) to use looser focusing in the direction of walk-off in order to maintain the spatial overlap of the fundamental and second harmonic beams over a long distance in the crystal. Here the Librecht-Simons analysis of SHG by Gaussian beams with elliptical cross sections is shortly reviewed.

The analysis assumes no depletion of the fundamental beam by the doubling process and in addition absorption is neglected at both the fundamental and the second harmonic wavelengths. The beam propagates along the z-axis and the geometry is as follows: A nonlinear crystal of length L is placed in the focus of the propagating Gaussian beam with elliptical cross section, such that the beam diameter at $z = 0$ (center of crystal) is $2w_x$ and $2w_y$ in the x and y directions, respectively. The electromagnetic field of a Gaussian beam with an elliptical cross section is described by Carter [77] and adopted in the paraxial approximation in the analysis. This field is dependent on the Rayleigh ranges $z_{Rx} = kw_x^2/2$ and $z_{Ry} = kw_y^2/2$ in the two directions respectively.

Now the ellipticity of the beam is defined as $\alpha = w_y/w_x$ and a focusing parameter (analogue to ξ in Boyd-Kleinman analysis) is defined as $\zeta = L/(\alpha)kw_x^2$. The second harmonic field is then

calculated following the formal analysis from [78] and [79] and finally the second harmonic power is found by integrating the z-component of the time-averaged Poynting vector (intensity) over the beam cross section.

The reader is referred to the original work for the full solution to the problem. Here we suffice with some important asymptotical values of the second harmonic power, $P_{2\omega}$. We will only consider the cases with no walk-off (i.e. $\rho = 0$):

$$\begin{aligned} &\zeta << 1\,, \quad \frac{\rho L}{w_x} << 1 \qquad \Rightarrow \quad P_{2\omega} = K\frac{L^2}{\alpha w_x^2}P_\omega^2 \\ &\zeta >> 1\,, \quad \frac{\rho k w_x \alpha}{2} << 1 \quad \Rightarrow \quad P_{2\omega} = K\pi^2\alpha k^2 w_x^2 P_\omega^2 \end{aligned} \tag{4.30}$$

where

$$K = \frac{8\pi d_{eff}^2}{\epsilon_0 n_\omega^2 n_{2\omega} c\lambda^2}. \tag{4.31}$$

Thus, for elliptical beams in the limits of loose ($\zeta << 1$) or strong focusing in phasematching interactions with no walk-off, the equations 4.30 may be used to estimate the efficiency of the interaction. The loose-focusing limit and the corresponding expression for $P_{2\omega}$ given in (4.30) is used for comparison in **Paper IV**, where an elliptical diode laser beam is applied in a SHG experiment.

4.3 Phasematching

In section 4.1.3 it was found that a phasematching condition $\Delta k = k_{2\omega} - 2k_\omega = 0$ must be fulfilled in order to have efficient SHG. This condition is equivalent to the condition that the refractive indices $n_{2\omega} = n_\omega$ (Eq. (4.27)), i.e. the fundamental and the second harmonic wave must travel at the same rate through the crystal. If this is in fact the case, then the contributions to the second harmonic wave generated at each position along the crystal add up in phase, such that the total second harmonic power is maximized. However, due to normal dispersion ($n_{2\omega} > n_\omega$) of the material, this is generally not the case, and several techniques have been investigated to overcome this problem. The most important techniques, birefringent phasematching and quasi-phasematching, are discussed in the following sections.

4.3.1 Birefringent phasematching

The arrangement of atoms in a three-dimensional lattice constituting a particular crystal defines three crystallographic, orthogonal axes a, b, and c. It turns out that for some materials, the velocity

of light propagating along one of these axes depend on the polarization of that light, i.e. the light may propagate slower along a if linearly polarized along b than if linearly polarized along c. Thus $n_b > n_c$. This means that if we arrange for the fundamental beam to be polarized along the "slow" axis of polarization (here b) and the second harmonic beam to be polarized along the "fast" axis of polarization (here c), the phase velocity difference due to dispersion of the material may be compensated for by the phase velocity difference due to birefringence, such that $n_{c,2\omega} = n_{b,\omega}$. This results in $\Delta k = 0$, as desired. This phasematching technique only applies for a particular wavelength, the phasematching wavelength λ_{pm} of the fundamental beam. See Fig. 4.6, which depicts the refractive index profiles for n_b and n_c as a function of wavelengths. It is observed that for wavelengths $\lambda_\omega > \lambda_{pm}$, the dispersion due to birefringence exceeds the material dispersion, while the opposite is the case for $\lambda_\omega < \lambda_{pm}$.

Finally, in order for efficient second harmonic conversion, the nonlinear d tensor must contain an appropriate component that couples the fundamental and the second harmonic waves. For a given crystal, and for given polarizations, this component is found from Eq. (4.17).

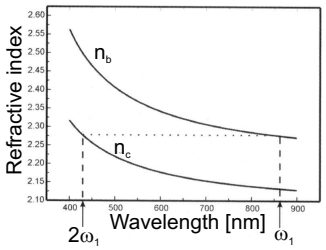

Figure 4.6. *The birefringent phasematching technique. Refractive index profiles n_b and n_c illustrate how birefringence can be used to achieve phasematching. From [69].*

Temperature tuning

Phasematching is sensitive to crystal temperature. This is due to the fact that the refractive indices involved in the SHG process change at a slightly different rate with temperature (see eg. [80]). Thus the wavelength at which $\Delta k = 0$ varies with temperature, and the desired phasematching wavelength may be obtained by tuning the temperature of the crystal.

Angle tuning

Also the direction of propagation affects the phasematching. The phasematching wavelengths when propagating the fundamental beam along the crystallographic a- or b-axes are different. Thus, if propagating the fundamental beam along some intermediate direction in the $a-b$ plane (keeping the polarization of the second harmonic along c), an intermediate phasematching wavelength may be obtained. This is illustrated in Fig. 4.7, which in analogy with Fig. 4.6 show the refractive index profiles of n_a, n_b, and some intermediate n_θ, which applies for a fundamental beam propagating at an angle θ with respect to the a-axis. Though angle tuning often makes it possible to obtain phasematching around room temperature, this technique involves the problem of spatial walk-off as mentioned in section 4.2.1. Phasematching by angle-tuning is sometimes referred to as *critical* phasematching, since the tolerance to angular deviation of the phasematching condition

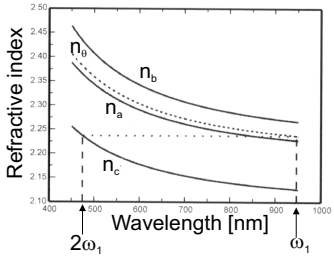

Figure 4.7. *Refractive index profiles for n_c, n_a and n_b in addition to some intermediate n_θ illustrates how angle tuning of the fundamental beam may be used to obtain phasematching. From [69].*

is decreased when propagation is not along one of the crystal principal axes [69]. Correspondingly, when propagation is along one of the crystal principal axes, the phasematching (e.g. by temperature tuning) is said to be *noncritical*.

Phasematching tolerances

When a phasematching solution is found for a wavelength of interest, the tolerance of this phasematching may be evaluated. I.e. the degree of accuracy to which the temperature and angle must be controlled can be examined. A common way to describe this phasematching tolerance is by the deviation in a phasematching parameter, ς ($\varsigma = T, \theta, ...$), of interest that results in a decrease in second harmonic power to 50% of its maximum value, $P_{2\omega,max}$. That is, if the second harmonic power is rewritten in the form

$$P_{2\omega} = P_{2\omega,max}\mathrm{sinc}^2\left[\frac{\Delta k(\varsigma)L}{2}\right], \tag{4.32}$$

where Δk now depends on ς, we wish to evaluate the change in ς that causes the sinc^2 function to equal 0.5. The maximum value of 1 is reached when ς is phasematched, $\varsigma = \varsigma_{pm}$, i.e. for $\Delta k = 0$. In order for the sinc^2 function to equal 0.5, the argument must equal 1.39. By expansion of Δk in a Taylor series, we obtain:

$$\Delta k(\varsigma) = \left.\frac{\partial \Delta k}{\partial \varsigma}\right|_{\varsigma=\varsigma_{pm}} (\varsigma - \varsigma_{pm}) + \frac{1}{2}\left.\frac{\partial^2 \Delta k}{\partial \varsigma^2}\right|_{\varsigma=\varsigma_{pm}} (\varsigma - \varsigma_{pm})^2 + \dots, \tag{4.33}$$

where we may choose to disregard the second derivative, which is usually negligible as compared to the first. The condition that the second harmonic output is one-half of its maximum value thus reads

$$\frac{1}{2}\left.\frac{\partial \Delta k}{\partial \varsigma}\right|_{\varsigma=\varsigma_{pm}} (\varsigma_{1/2} - \varsigma_{pm})L = 1.39\,, \tag{4.34}$$

i.e. the the tolerance in a phasematching parameter may be written

$$\Delta\varsigma_{1/2} = (\varsigma_{1/2} - \varsigma_{pm}) = \frac{2.78}{\left.\frac{\partial \Delta k}{\partial \varsigma}\right|_{\varsigma=\varsigma_{pm}} L} \tag{4.35}$$

Eq. (4.35) can be applied to estimate the phasematching tolerance for any phasematching parameter of interest.

4.3.2 Quasi-Phasematching

As we saw in the preceding section, there are some problems occurring when using birefringent phasematching, such as walk-off, possibly low effective nonlinear coefficient, and inconvenient phasematching temperatures and angles. Furthermore, the material may not possess enough birefringence to provide phasematching at the desired wavelength and the phasematching tolerances may be very strict. Quasi-phasematching (QPM) is an alternative method to enable a continous growth of the second harmonic wave along the crystal. QPM is based on an artificial structuring of the material rather than on its birefringent properties. It can even be achieved in materials possessing no birefringence at all, i.e. isotropic media, such as certain semiconductors having large nonlinearities (e.g. GaAs and GaN). A significant advantage of QPM is that any interaction within the transparency range of the crystal can be noncritically phase-matched at a specific temperature. Another benefit is that QPM gives access to the largest element of the d-tensor, by appropriate choice of the interacting waves. The method of QPM was suggested as early as 1962 by Armstrong *et al.* [81]. Numerous realizations were attempted during the 1970's (see e.g. [82–85]), but with limited success due to manufacturing problems of periodic nonlinear structures on micrometer scales.

Basic ideas of QPM

The flow of power from one wave to the other in the nonlinear crystal is determined by the relative phase between the waves. The continuous phase slip between the fundamental and the second harmonic waves caused by their differing phase velocities leads to an alternation in the direction of the flow of power. After a certain distance, known as the coherence length L_c, the conversion efficiency reduces and energy flows back from the second harmonic to the fundamental wave. This distance has been travelled when the relative phase of the two waves has changed by π, i.e. $L_c = \pi/\Delta k = \lambda/4(n_{2\omega} - n_\omega)$. For a crystal of a length much longer than the coherence length, the efficiency thus behave in the way of the Maker fringes discussed in section 4.1.3 (see Eq. (4.26) and text below). The period of these oscillations is $2\pi/\Delta k = 2L_c$ so that after one coherence length maximum energy has been transferred to the second harmonic wave. This oscillating behavior is illustrated in Fig. 4.8(d), which shows the second harmonic intensity as a function of crystal length. Fig. 4.8(a), shows the ideal phasematching situation, where by some means $n_{2\omega} = n_\omega$. We will return to curves (b) and (c).

In QPM, the relative phase between the fundamental and the second harmonic waves is repeatedly inverted after an odd number of coherence lengths. In this way, the phase is periodically

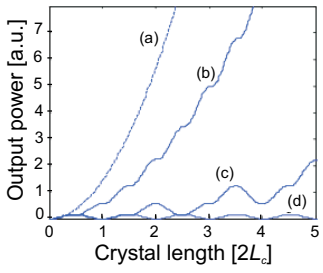

Figure 4.8. *Output power versus crystal length for (a) perfectly phasematched, (b) first-order QPM, (c) third-order QPM, and (d) non-phasematched frequency conversion.*

"reset" when the transfer of energy to the second harmonic wave is at its maximum. Thus, the second harmonic wave continues to grow through the crystal. One way to accomplish phase inversion is by changing the sign of the nonlinear coefficient. This can be done e.g. by slicing the crystal into sections one odd number of coherence lengths long and rotate every other section by 180° about the direction of propagation. However, in blue-green generation, where the coherence length is only a couple of micrometers, this mechanical approach is difficult to handle.

A more practical approach, which can be used for ferroelectric crystals, involves forming regions ("domains") of periodically reversed spontaneous polarization. Ferroelectric materials exhibit a spontaneous electric polarization below a certain temperature (the Curie temperature), even with no electric field applied. Reversing the direction of the spontaneous polarization by some means and then applying a fundamental electric field will result in a second-harmonic component of the induced polarization which is indeed 180° out of phase with the component when no reversal has been applied [69]. Thus in order to obtain QPM, the spontaneous polarization must be periodically inverted. The process of aligning the direction of the spontaneous polarization is called *poling* and a region of the crystal in which the spontaneous polarization has the same alignment is called a *ferroelectric domain*. Thus a crystal having periodic reversals of the spontaneous polarization is said to be *periodically poled* (PP) (or periodically domain inverted). In practice domain-inversion may be obtained by applying a periodic electrode, such as e.g. a patterned metal film, on one surface of the crystal. On the other side, a uniform electrode is applied. When a sufficiently large (in the range of kV/mm) electric field is applied to the electrodes, inverted domains begin to form below the areas where the electrode is in contact with the crystal. The domain continue to grow until the entire volume below the electrode is inverted and a periodically poled crystal is formed. The electrical field necessary to start the inversion process is referred to as the *coercive field*. Periodically poled crystals benefit from the possibility of phasematching any nonlinear process and thus are limited only by the transparency range of the crystal.

The most efficient QPM appears when the sign of the spontaneous polarization is changed every coherence length. This situation is shown in Fig. 4.8(b), and is denoted first-order QPM. Third-order QPM, shown in Fig. 4.8(c) is less efficient, but may be applied, e.g. if the coherence length is too small in order to produce a high-quality periodic poling in the crystal. By mixing different domain lengths, even-order QPM may also be obtained and in general m^{th} order QPM results in modulation with a period $2mL_c$, where m is an integer.

As apparent from Fig. 4.8, even first-order QPM is not as efficient as birefringent phasematching. However, as mentioned in

the beginning of this section, the advantages of QPM are numerous and of great significance. The results in **Paper IV** are obtained using QPM in a periodically poled $KTiOPO_4$ (KTP) crystal. With this material, phasematching at 810 nm can be achieved at modest temperature and the QPM approach permits access to the highest nonlinear coefficient, which is the d_{33} coefficient in KTP. Furthermore, any walk-off problems are avoided because parallel polarizations along the crystal main axis are used. (PP)KTP is described in more detail in section 4.4.1.

Theory of QPM

The summary of the theory of QPM given in this section largely follows the work by Fejer et al. [86]. In that work, special attention is given to the imperfect QPM structures and the influence on these imperfections on effeciency. Using the same assumptions as in section 4.1.3, the growth of the second harmonic field is given by (see Eq. (4.23))

$$\frac{dA_{2\omega}}{dz} = -\Gamma d(z) e^{i\Delta k' z}\,, \tag{4.36}$$

where $A_{2\omega}$ is the amplitude of the second-harmonic field, z is the distance along the propagation direction, $d(z)$ is the spatially varying nonlinear coefficient, and $\Gamma = i\omega A_\omega^2 \mu_0 c/n_{2\omega}$. $\Delta k'$ is the wave vector mismatch caused by dispersion in the material:

$$\Delta k' = k_{2\omega} - 2k_\omega = \pi/L_c\,, \tag{4.37}$$

where $L_c = \lambda/4(n_{2\omega} - n_\omega)$ is the coherence length of the QPM structure. Integration of (4.36) yields the second harmonic field at the end of a crystal of length L:

$$A_{2\omega}(L) = -\Gamma \int_0^L d(z) e^{i\Delta k' z} dz \tag{4.38}$$

For perfect and conventional phasematching, i.e. $d(z) = d_{\mathit{eff}}$, where d_{eff} it the appropriate nonlinear coefficient for the interaction, and $\Delta k' = 0$, (4.38) readily yields:

$$A_{2\omega}(L) = -\Gamma d_{\mathit{eff}} L\,, \tag{4.39}$$

in agreement with (4.25). In the QPM approach, assume $d(z)$ consists of domains of nonlinear coefficient $\pm d_{\mathit{eff}}$ with sign changes occurring at the positions z_j. If the sign of the j^{th} domain is denoted g_j, Eq. (4.38) may be written:

$$A_{2\omega} = \frac{i\Gamma d_{eff}}{\Delta k'} \sum_{k=1}^{N} g_k [e^{i\Delta k' z_k} - e^{i\Delta k' z_{k-1}}] , \tag{4.40}$$

where N is the number of domains. If the structure is perfect, the sign changes occur at positions $z_{k,0}$ which are chosen to satisfy

$$e^{i\Delta k'_0 z_{k,0}} = (-1)^k , \tag{4.41}$$

where $\Delta k'_0$ is the wave vector mismatch at the design wavelength. For symmetrical odd-order QPM, we have $z_{k,0} = mkL_c$. If the device structure differs from the ideal and/or $\Delta k'$ differs from the designed value, phase errors will accumulate. We define the position error of the k^{th} boundary as $\delta z_k = z_k - z_{k,0}$, and the deviation of the actual wave vector mismatch from that of the designed value as $\delta\Delta k' = \Delta k' - \Delta k'_0$. The accumulated phase error at the k^{th} boundary is then given by

$$\begin{aligned} \Phi_k =& \Delta k' z_k - \Delta k'_0 z_{k,0} \\ =& \Delta k'(\delta z_k + z_{k,0}) - (\Delta k' - \delta\Delta k') z_{k,0} \\ =& \Delta k' \delta z_k + \delta\Delta k' z_{k,0} . \end{aligned} \tag{4.42}$$

Rewriting Eq. (4.40), collecting terms, and using (4.41) and (4.42) gives

$$A_{2\omega} = \frac{i\Gamma g_1 d_{eff}}{\Delta k'} \left[2 \sum_{k=1}^{N-1} e^{i\Phi_k} + (e^{i\phi_N} + 1) \right] , \tag{4.43}$$

where the last two terms originate from the the N^{th} and the first ($e^{i\Delta k' z_0}$) terms in the sum, respectively. For $N >> 1$, which is usually the case, the following approximation holds

$$A_{2\omega} = \frac{i\Gamma g_1 d_{eff}}{\Delta k'} \sum_{k=1}^{N} e^{i\Phi_k} . \tag{4.44}$$

For a structure without phase errors, $\Phi_j = 0$ for $1 > j > N$, the sum in (4.44) equals N, which for a perfect structure obeys $N = L/mL_c = L\Delta k'/m\pi$. Thus, in this situation, (4.44) becomes

$$A_{2\omega,ideal} \approx i\Gamma g_1 d_{eff} \frac{2}{m\pi} L . \tag{4.45}$$

Comparing this expression for the second harmonic field to Eq. (4.39), it is observed that the effective nonlinearity of SHG with a

perfect m^{th} order QPM structure is reduced by a factor of $2/m\pi$ compared to conventionally phasematched SHG. Thus, the effective nonlinear coefficient d_Q of QPM interactions is related to d_{eff} by:

$$d_Q = \frac{2d_{eff}}{m\pi} \tag{4.46}$$

Phasematching tolerances for QPM with an ideal grating

The phasematching tolerances for QPM structures may be found in a similar way as for birefringent phasematching, see section 4.3.1 and Eq. (4.35). The main difference is that the phasematching condition for QPM involves a term that accounts for the periodic domain-inversion. For QPM the total wave vector mismatch is defined as [86]:

$$\Delta k \equiv k_{2\omega} - 2k_{\omega} - K_m \tag{4.47}$$

where $K_m = 2\pi m/\Lambda$ is the grating vector of the m^{th} order QPM grating and Λ is the period of the poling, see Fig. 4.9. Thus, the effective mismatch Δk of the QPM interaction is shifted by an amount K_m with respect to the the mismatch $\Delta k'$ of conventional phase matching. Below we briefly present the equations describing the wavelength and temperature phasematching tolerances in QPM interactions.

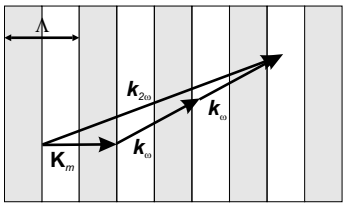

Figure 4.9. *The effective mismatch of a QPM interaction is shifted by an amount K_m (the grating vector) with respect to the mismatch of conventional phasematching. Λ is the period of the poling and m is the order of the phasematching.*

The wavelength tolerance in QPM SHG The wavelength tolerance for QPM interactions is given by [69, 86]:

$$\Delta\lambda_{FWHM} = \frac{1.39\lambda_{pm}}{\pi L}\left|\frac{1}{2}\frac{\partial n_{2\omega}}{\partial\lambda} - \frac{\partial n_{\omega}}{\partial\lambda} - \frac{n_{2\omega} - n_{\omega}}{\lambda_{pm}}\right|^{-1} \tag{4.48}$$

where the derivatives are evaluated at their respective wavelengths. The last term in this expression would vanish in the case of Type-I birefringent phase matching, where $n_{2\omega} = n_{\omega}$.

Temperature tolerance in QPM SHG The temperature tolerance for QPM interactions is given by [69, 86]:

$$\Delta T_{FWHM} = \frac{1.39\lambda_{pm}}{\pi L}\left|\left(\frac{\partial n_{2\omega}}{\partial T} - \frac{\partial n_{\omega}}{\partial T}\right) - \gamma(n_{2\omega} - n_{\omega})\right|^{-1} \tag{4.49}$$

where $\gamma \equiv L^{-1}\partial L/\partial T$ is the coefficient of linear thermal expansion. As before, for type-I birefringent phasematching, the last term disappears.

The derivatives of n with respect to λ and T are found from the relevant Sellmeir equations (e.g. for fluxgrown KTP, see [87]) and relevant temperature derivatives (for KTP see [88]), respectively.

4.3.3 Other Phasematching techniques

A number of other phase matching techniques are available. These include waveguide phasematching [89, 90], anomalous dispersion [91], counterpropagating waves [92–94], total internal reflection [81, 95, 96], and form birefringence [97, 98]. However, birefringent phasematching and QPM are far the most applied, and we will not deal with the remaining techniques.

4.4 Materials for SHG

In this section, some of the nonlinear materials used for SHG are reviewed with special emphasis on materials suited for blue-light generation and in particular potassium titanlyl phosphate, which is the material used for SHG in **Paper IV**.

4.4.1 Potassium titanyl phosphate - $KTiOPO_4$

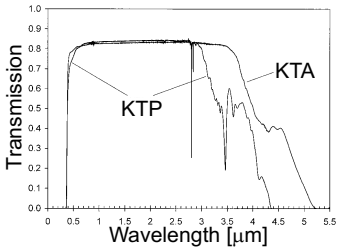

Figure 4.10. *Transmission window of KTP (and KTA). Adopted from [101].*

Potassium titanyl phosphate (KTP) was introduced in 1976 by Zumsteg *et al.* [99] and belongs to the family of isomorphic compounds with the general composition of $MTiOXO_4$, with X={P, As} and M={K, Rb, Tl, Cs (only for X = As)}. KTP exhibits the orthorhombic class $mm2$ point group symmetry at room temperature [100], and it posses a large nonlinearity, high damage threshold, and excellent thermal stability. It is transparent in the range 350 - 4500 nm, see Fig. 4.10 for transparency curve [101]. A typical morphology of the orthorhombic $mm2$ crystal is shown in Fig. 4.11, where the four families of crystallographic planes ({100}, {110}, {011}, {201}), constituting the fourteen facets, are outlined.

The properties of KTP depend on the method of growth. Mainly two methods are used: the hydrothermal method and the flux growth technique. The former method requires high pressure and high temperature in small chambers, which results in rather small crystals. The flux growth method, on the other hand, uses high temperatures at atmospheric pressure, which opens the possibility for larger crystal structures. Hydrothermally grown crystals have lower ionic conductivity and higher resistance to optical damage, such as "gray tracking" than flux grown materials. Gray tracking is a spectrally broad absorption that occurs with exposure to intense short-wavelength radiation [102, 103]. Also the Sellmeier

equations determined from measurements on crystals grown after the two methods are different.

Type-II birefringent phasematching is efficient in KTP [104, 105] and non-critically phasematched type-II interactions can exhibit remarkably large tuning ranges with respect to temperature and angle [106, 107]. The effective nonlinearity for type I phasematching, however, is too small for this interaction to be of general interest. This latter statement does not apply in the case of QPM, which is discussed below. In table 4.1 some of the important properties of KTP, including its d tensor, are collected.

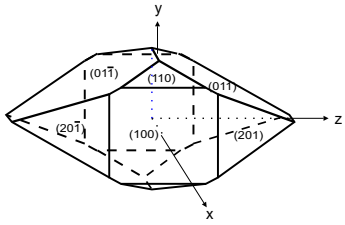

Figure 4.11. *Typical habit of the orthorhombic crystal. Such crystals exhibit fourteen facets belonging to four families of crystallographic planes, namely {100}, {110}, {011}, and {201}.*

Periodically poled KTP

Different methods have been proposed in order to form inverted-domain gratings in KTP. Periodic poling by the application of an electrical field (see section 4.3.2) is far the most applied method, and the method that we will focus on here. With this technique, $4\,\mu$m-period gratings have been induced in hydrothermally grown KTP using a periodic metal electrode [110]. A relatively low field of 2 kV/mm successfully poled a thick (1 mm) KTP crystal in ambient atmosphere pressure. Due to the larger ionic conductivity of flux grown crystals, electric-field poling of these structures is more difficult than for hydrothermally grown crystals. In 1997, Rosenman *et al.* suggested a method to overcome the difficulties and obtain domain-inversion by electric field-poling of flux grown KTP [111]. The method was demonstrated to produce first-order gratings at $6.9\,\mu$m-period in KTP yielding a high SHG efficiency [112]. This method has been applied extensively (see e.g. [113, 114]) ever since. The crystal used in **Paper IV** is a flux grown PPKTP crystal.

4.4.2 Other materials

Several other materials for SHG exist. Here a few materials, which all have been periodically poled, are mentioned.

(PP) Lithium niobate - $LiNbO_3$ (LN)

(PP)LN is a trigonal class $3m$ crystal and one of the most widely used nonlinear materials. Its nonlinearity is high with $d_{33} \simeq 25$ pm/V at 1064 nm [115]. The transparency ranges from 330 nm to 5500 nm so PPLN may be applied to a wide range of frequency conversions with its period matched to the wavelength of interest. The coercive field in LN is around 21 kV/mm, i.e. about ten times higher than for KTP. This results in a more difficult poling process and a more strict limit to the thickness of the crystal that can be poled as compared to KTP. Furthermore, the optical damage threshold is lower than for KTP [116].

Table 4.1. *KTP*

Refractive indices

Flux-grown material [87]

$n_x^2 = 2.16747 + \frac{0.83733}{1-0.04611\lambda^{-2}} - 0.01713\lambda^2$

$n_y^2 = 2.19229 + \frac{0.83547}{1-0.04970\lambda^{-2}} - 0.01621\lambda^2$

$n_z^2 = 2.25411 + \frac{1.06543}{1-0.05486\lambda^{-2}} - 0.02140\lambda^2$

Wavelength λ in μm.

Hydrothermal material [108]

$n_x^2 = 2.1146 + \frac{0.89188}{1-0.04352\lambda^{-2}} - 0.01320\lambda^2$

$n_y^2 = 2.1518 + \frac{0.87862}{1-0.04753\lambda^{-2}} - 0.01327\lambda^2$

$n_z^2 = 2.3136 + \frac{1.00012}{1-0.05679\lambda^{-2}} - 0.01679\lambda^2$

Wavelength λ in μm.

Temperature derivatives [88]

$\frac{\partial n_x}{\partial T} = (1.427\lambda^{-3} - 4.735\lambda^{-2} + 8.711\lambda^{-1} + 0.952)(10^{-6}/°\mathrm{C})$

$\frac{\partial n_y}{\partial T} = (4.269\lambda^{-3} - 14.761\lambda^{-2} + 21.232\lambda^{-1} - 2.113)(10^{-6}/°\mathrm{C})$

$\frac{\partial n_z}{\partial T} = (12.415\lambda^{-3} - 44.414\lambda^{-2} + 59.129\lambda^{-1} + 12.101)(10^{-6}/°\mathrm{C})$

Nonlinear properties

d tensor - Symmetry class $mm2$

$$\begin{bmatrix} 0 & 0 & 0 & 0 & d_{15} & 0 \\ 0 & 0 & 0 & d_{24} & 0 & 0 \\ d_{31} & d_{32} & d_{33} & 0 & 0 & 0 \end{bmatrix}$$

d coefficients [109]

	d_{il}				
	d_{15}	d_{24}	d_{31}	d_{32}	d_{33}
880 nm	2.04	3.92	2.76	4.74	18.5
1064 nm	1.91	3.64	2.54	4.35	16.9

(PP) Lithium tantalate - $LiTaO_3$ (LT)

(PP)LT has a high nonlinearity with $d_{33} = 13.8\,\mathrm{pm/V}$ [115]. This crystal is an interesting candidate for ultraviolet light generation since it is transparent down to 280 nm [117]. Optical damage threshold is higher than for LN [118], but the coercive field is equally high, i.e. around 21 kV/mm. Thus PPLT crystals are usually rather thin (~ 0.2 mm) (see e.g. [119]).

(PP) KTP isomorphs

Rubidium titanyl arsenate ($RbRiOAsO_4$ or RTA) may be the most important isomorph of KTP for blue/green light applications. Flux grown RTA has a ionic conductivity which is comparable to that of hydrothermally grown KTP, which makes RTA fairly easy to pole [120]. The largest nonlinear coefficient is $d_{33} = 15.8\,\mathrm{pm/V}$ [120]. Other isomorphs of KTP, such as KTA and RTP, have also been investigated. PPKTA [121] and PPRTP [122] have been reported, but neither of the materials have been investigated thoroughly in blue-light generation.

Chapter 5

Photodynamic therapy

Photodynamic therapy (PDT) is a modality that may be used for local treatment of precancerous and cancerous tumors. PDT relies on the coexistence of a photosensitive compound (a photosensitizer), oxygen, and light. The photosensitizer is administered to the patient, where it accumulates selectively in the cancerous tissue. Subsequent irradiation with non-ionizing radiation, such as laser light, causes a photochemical reaction to occur, which destructs the cancerous cells. The first clinical studies of PDT using hematoporphyrin derivative (HpD) took place during the 1960's [123, 124] and the field has been expanding ever since. Today, PDT is approved for various clinical applications and commercial drugs and light sources are available. Some of the most important features of PDT are high selectivity, fast healing rates, and the ability to treat the same tissue several times, if necessary. An important drawback is limited penetration of the therapeutic light. This disadvantage may be partly overcome by the development of photosensitizers, which are sensitive in the near-infrared wavelength range or by the use of interstitial PDT, where the therapeutic light is guided into the tumor using optical fibers. The laser systems described in **Papers I-II** were both developed for interstitial PDT and tested in preliminary clinical trials. The results from these trials are summarized in chapter 7. In this chapter, the basic mechanisms of PDT, and the parameters important for PDT are briefly discussed.

5.1 Mechanisms of action

The therapeutic light, which must match an absorption band of the photosensitizer, excites the photosensitizer molecule from its singlet ground state to its first excited singlet state. From here the molecule may transfer to its first excited triplet state. Though this transition is spin forbidden, it has a relatively high probability

of occurring due the small energy separation between the states. The final relaxation to the ground state is again spin forbidden, leading to a long life time ($\gtrsim 100\,\mu$s) and thus a high probability for interaction with the surrounding molecules. The excess energy of the photosensitizer may be transferred to oxygen molecules, which thereby are excited from their triplet ground state to one of the first excited singlet states, which are biologically active. Singlet oxygen is highly cytotoxic and its formation leads to degradation of the cancerous cells by various mechanisms.

One of the advantages of PDT over other existing tumor treatment modalities, such as radiation therapy or cryotherapy, is that the photosensitizer accumulates selectively in the diseased tissue. This means that irradiation of the healthy tissue occurs at low damage risk and that full treatment of precancerous or cancerous cells outside the visible tumor border can also be achieved. Other advantages count fast healing rates, modest scar formation, and the possibility for re-treatment several times if necessary. Finally, PDT is fairly uncomplicated to perform with few potential hazards involved. Pain is experienced in variable degree, but in general anaesthesia is not required.

5.1.1 Photosensitizers

A photosensitizer is often a fluorescent, tumor-selective compound. Numerous variants of photosensitizers for PDT exist, and only a few will be mentioned here. Some important parameters must be considered when synthesizing photosensitive compounds for PDT. It is important that they absorb light at wavelengths where the tissue is relatively transparent. In Fig. 5.1 the absorption coefficients of the major absorbers, the chromophores, in biological tissue are shown as a function of wavelength. Also shown is the absorption of a commonly used photosensitizer, Photofrin®. The area marked in gray between approximately 630 and 1300 nm is denoted "the tissue optical window". In the tissue optical window, the water absorption is low, and the blood absorption falls off. The absorption from melanoma in the skin, however, remains rater high. As apparent from Fig. 5.1, reasonable tissue penetration requires that the wavelength of the therapeutic light lies within the tissue optical window. Thus, the photosensitizer should have an absorption band in this window. For deeper penetration, and thus larger treatment volumes, the treatment wavelength should belong to the longer wavelength part of the window. However, the triplet state energies are lower for photosensitizers absorbing in this region and there is an upper limit for the generation of singlet oxygen. Photosensitizers absorbing at longer than approximately 800 nm cannot be used [125]. Here we will concentrate on the photosensitizer for which the laser systems in **Papers I-II** were developed.

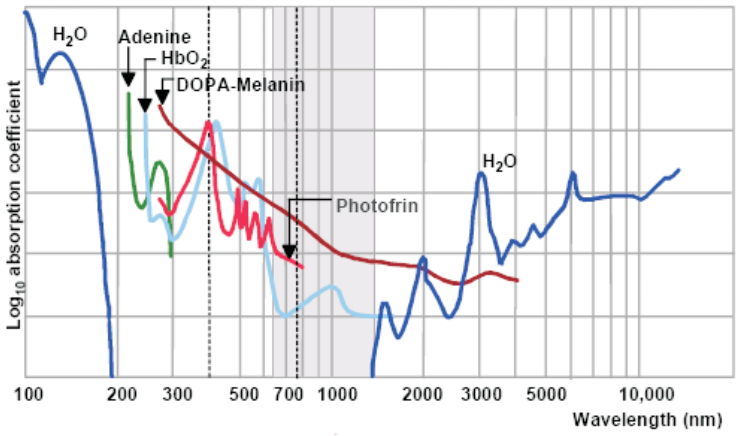

Figure 5.1. *Absorption coefficient as a function of wavelength for the major absorbers in biological tissue together with a commonly used porphyrin-based photosensitizer, Photofrin®. The area marked with gray is the "tissue optical window" in which the water absorption is low and the blood absorption falls off. The melanoma absorption remains rather high. The area marked by dashed lines represents the visible spectrum of light. Adopted from [126].*

The use of endogenous photosensitization is an interesting possibility in PDT. With this method, a precursor is administered to the patient and the photoactive compound is produced by the target cancerous tissues themselves. In 1987, Malik *et al.* [127] introduced the photoactive protoporphyrin IX (PpIX) induced by the precursor 5-aminolevulinic acid (ALA) as an endogenous photosensitizer for PDT. The method was fully developed by Kennedy and Pottier [128, 129] and soon thereafter adopted by the group at Lund University Medical Laser Centre [130]. PpIX has a strong absorption around 405 nm and a weaker absorption around 635 nm. In order to have maximum penetration depth, the red absorption band is frequently used for PDT. However, by irradiation with blue light, an easily recognizable, dual-peaked, red fluorescence may be excited that can be used for diagnostic purposes (see chapter 6). The dual-peaked fluorescence from PpIX is emitted at 635 nm and 700 nm. Today, ALA-PDT is one of the most widely used variations of PDT.

Accumulation of ALA-induced PpIX

ALA is a naturally occurring, 5-carbon, straight-chain amino acid, see Fig. 5.2. It is required for synthesis of haem, which is the porphyrin molecule PpIX with an iron atom incorporated into its core. PpIX (see Fg. 5.3) is thus the last molecule in the haem

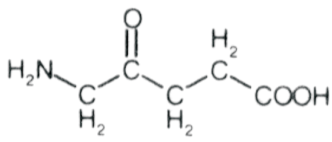

Figure 5.2. *Chemical structure of ALA.*

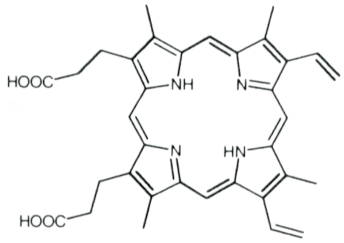

Figure 5.3. *Chemical structure of PpIX.*

cycle before the incorporation of iron by the action of the enzyme ferrochelatase. The haem biosynthetic pathway is illustrated in Fig. 5.4. The production of PpIX is regulated by a feedback mechanism, but when ALA is exogenously supplied, the negative feedback on the enzyme δ-aminolevulinic acid synthase, which catalyzes the formation of ALA and is considered to have a main regulatory function in the synthesis, is bypassed. Furthermore, the capacity of ferrochelatase is exceeded. Finally, some pre-malignant and malignant lesions show a reduced activity of ferrochelatase, and an increased activity of the enzyme, porphobilinogen deaminase, catalyzing the third step [131, 132]. These features contribute to a build-up of PpIX in malignant tissue, as compared to normal tissue, upon ALA administration [133].

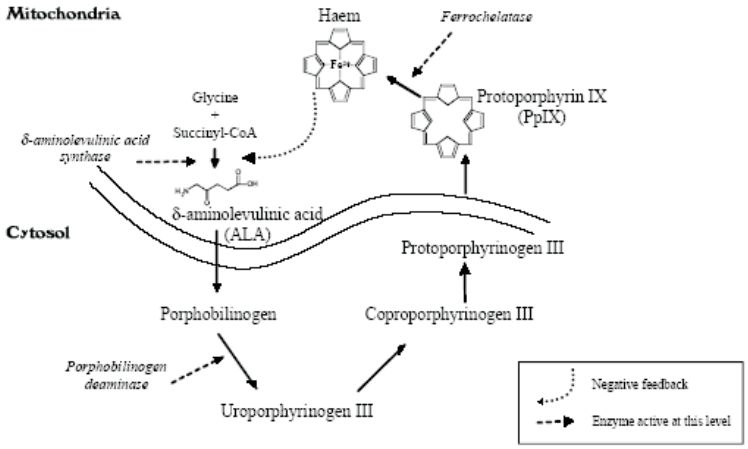

Figure 5.4. *Biosynthetic pathway of haem. When ALA is supplied in excess, an accumulation of PpIX in the diseased tissue occurs. This is partly due to changes in the enzymatic activities of porphobilinogen deaminase and ferrochelatase in the cycle. From [125].*

The kinetics of the PpIX build-up vary with tumor location and the administration method of ALA. For applications in dermatology, where ALA is mixed and supplied as a cream, increased permeability of the diseased skin, enhances the selectivity of the ALA uptake. In most other cases, ALA is diluted in juice and orally administrated, but intravenous administration is also a possibility. Typically, the selectivity and build-up of PpIX is sufficient for the treatment to begin after a couple of hours. The fluorescence emission from PpIX is maximized after 4-6 hours [134] and it is usually cleared after 24 hours.

In order to increase penetration depth in topical applications of the hydrophilic ALA, esterified versions have been investigated

[135, 136]. It has been verified that by attachment of lipophilic carbon chains to ALA, a deeper penetration and a reduced accumulation time can be achieved. Studies have been performed to establish the optimal length of the attached carbon chain, and they show that the PpIX formation rate is higher for long chained ALA esters than for short chain ALA esters [137]. However, if the chain is too long, ALA may get trapped in the upper layers of the lesion. The studies in [138] show that methyl-esterified ALA accumulates more selectively than ALA in basal cell carcinomas.

5.1.2 Photo-oxidation

The generation of molecular oxygen in its excited single state is believed to be the primary cause of cell-damage in connection with PDT. This highly reactive oxygen species is generated by transfer of energy from the photosensitizer in its excited triplet state to molecular oxygen. In the transfer, the photosensitizer relaxes to its ground state from where it again is prone to excitation under the influence of the therapeutic light. In this way the cycle can be repeated. Singlet molecular oxygen reacts rapidly with various cellular components, such as unsaturated lipids, proteins, nucleic acids etc.

The diffusion length of singlet oxygen in biological tissue is around 0.01-0.04 μm [139] which is less than one percent of the diameter of a red blood cell ($\sim 7\,\mu$m). This indicates that it is the localization of the photosensitizer that determines the type of damage induced in the tissue during treatment. If the photosensitizer is lipophilic, it will accumulate in the plasma and organellar membranes of cells and the photo-oxidation may result in a direct rupture of the membranes and inactivation of the enzymes and receptors affiliated with that membrane. Hydrophilic photosensitizers, on the other hand, may accumulate in lysosomes and endosomes [140, 141], such that photo-oxidation results in the release of lysosomal enzymes in the cytoplasm. In this case another mechanism of tissue damage is induced [140]. Studies show that the probability of cell damage per quantum of absorbed energy is higher for lipophilic than for hydrophilic photosensitizers, indicating that the membranes are more vulnerable to treatment.

As for the case of ionizing radiation therapy, well oxygenated tissue is more vulnerable to cell destruction and thus to treatment than tissue with low oxygen content. Limitations in oxygen can occur during treatment either due to vascular damage, or to the fact that oxygen is consumed during treatment. When using oral or intravenous administration of the photosensitizer, a large amount will accumulate in the endothelial cells of the blood vessels, which may suffer permanent damage [142, 143]. Vascular damage results in a restricted blood perfusion in the tumor, and measurements of blood perfusion during treatment indeed indicate

these vascular effects [144]. Studies have been performed in which the treatment has been fractionated in various ways in order for the oxygen content to increase. In some cases fractionation leads to an improvement in treatment efficiency, but in others it does not imply a significant difference from continuous treatment.

5.1.3 Therapeutic light

Coherent light sources, such as lasers, as well as incoherent light sources, such as filtered lamps or LEDs, are used for PDT. Due to their narrow bandwidth, lasers are able to minimize hyperthermal effects during PDT since they can be confined to the absorption band of the photosensitizer. Heating of the tissue due to absorption can thus be minimized by decreasing the light dose absorbed by non-PDT-active chromophores. Furthermore, the spatial properties of lasers makes them suitable for fiber coupling. Fiber guidance of the light facilitates the treatment of body-cavities using endoscopes or interstitial PDT, where fibers are inserted into the tumor using needles. LEDs and filtered lamps, such as Xenon lamps, may be used for superficial PDT, especially of larger lesions, where fiber guidance of the therapeutic light is unnecessary. Here we will focus on laser sources, which may be used for superficial and interstitial PDT in addition to PDT of body-cavities.

In the beginning of the nineties, the typical lasers for PDT were Argon-ion or Copper-vapor laser pumped dye lasers in addition to frequency doubled Nd:YAG laser pumped dye lasers. These lasers are large, expensive, and complicated systems which require frequent service. Furthermore, they have a high electrical energy consumption, and need extensive water cooling. An advantage is that, by using appropriate dyes, these lasers can be used for PDT with several different photosensitizers. However, the dye introduces yet another disadvantage, since it has to be exchanged regularly in order to maintain high output power.

Diode lasers are compact, easy to operate, requires no water cooling, and are available at a reasonable cost. They are thus attractive in a clinical environment. As described in chapter 2, diode lasers are available at very high powers in the near-infrared. However, at these wavelengths no photosensitizers are available. In the late nineties, diode laser systems emitting at 635 nm for ALA-PDT became commercially available. These laser systems deliver approximately 2 W through a fiber with core diameter of 400 μm or more. Today, diode lasers are the most important laser light sources for PDT. They are available at several wavelengths matching various photosensitizers. Some of the important photosensitizers, which have commercial diode laser sources available at their absorption wavelengths for PDT are collected in table 5.1. Common for all the diode laser sources for PDT, is that the therapeutic light is delivered through relatively thick optical fibers with

core diameters of 400 μm or more (See e.g. [145]). This is due to the poor spatial coherence of diode lasers, as discussed in chapter 2, and it sets a limitation for the procedure of interstitial treatments, where a thinner treatment fiber may be the optimal choice (see e.g. [146]). By using a thinner treatment fiber with the commercial systems, a considerable amount of output power is lost. One of the aims of this Ph.D. work was to realize diode laser systems for ALA-PDT delivering the therapeutic light through thin optical fibers without discarding a large fraction of optical power from the diode laser. Commercial diode laser systems for PDT are available from numerous companies, such as Diomed, Biolitec Inc. (CeramOptec), Coherent Inc., and Carl Zeiss.

Table 5.1. *Some of the photosensitizers, which have commercial diode laser sources available at their excitation wavelengths for PDT. HpD: Hematoporphyrin derivative, PpIX: Protoporphyrin IX, mTHPC: Meso-tetrahydroxyphenyl chlorin, BPD-MA: Benzoporphyrin Derivative-monoacid Ring A, Lu-Tex: Lutetium texaphyrin.*

Sensitizer	Tradename	Wavelength
HpD	Photofrin®	630 nm
PpIX	ALA	635 nm
mTHPC	Foscan®	652 nm
BPD-MA	Verteporfin	690 nm
Lu-tex	LUTRIN®	732 nm

5.2 Clinical applications

PDT can be applied in the treatment of various diseases [147], such as psoriasis, age-related macula degeneration, and diabetic retinopathy. In this work, we focus on its ability to treat cancerous and pre-cancerous lesions, such as skin cancers and deeper-lying solid tumors, or cancers in body-cavities.

5.2.1 Superficial PDT of skin cancers

The laser system described in **Paper II** was used in the treatment of superficial basal cell carcinomas (BCC) (see chapter 7, section 7.1.2) and compared to a conventional treatment. BCC is not the most malignant type of skin cancer, but it is the most common type of cancer and thus constitutes a considerable health risk to a large segment of the world population. PDT is used for the treatment of BCCs in many clinics. However, conventional treatments such

as excision (surgically removing the cancerous lesion), curretage (scraping), electrocautery (burning away the abnormal cells with an electric rod), and cryosurgery (freezing the site with carbon dioxide or nitrous oxide) are still widely used. In Ref. [148] PDT is compared to cryotherapy in a phase III clinical trial. The cure rates are comparable, but the healing rates and cosmetic outcome for the lesions treated with PDT are clearly superior to the results obtained with cryotherapy. The results obtained with the laser from **Paper II** in PDT of BCC show a similar tendency. Here the PDT was compared to electrocautery and curretage (see section 7.1.2), and again the results with PDT were superior in terms of healing rate and cosmetic outcome, while the cure rates were equally successful.

5.2.2 Interstitial PDT of deeper-lying solid tumors

When treating thick lesions or deeply localized solid tumors, superficial treatment may not be sufficient, and interstitial PDT must be applied. The first system for combined light dosimetry measurements and interstitial PDT at Lund University Medical Laser Centre was presented in 1996 [149–151], which splits up the therapeutic light into several optical fibers. The lay-out of the system is shown in Fig. 5.5. This system facilitates the use of three or six independent treatment fibers, which are inserted into the tumor so that the therapeutic light attacks the tumor from different positions. Optimal positions, depending on tumor topography, are calculated using dosimetry software, which has been developed for the system. The laser unit used for treatment (e.g. the Ceralas

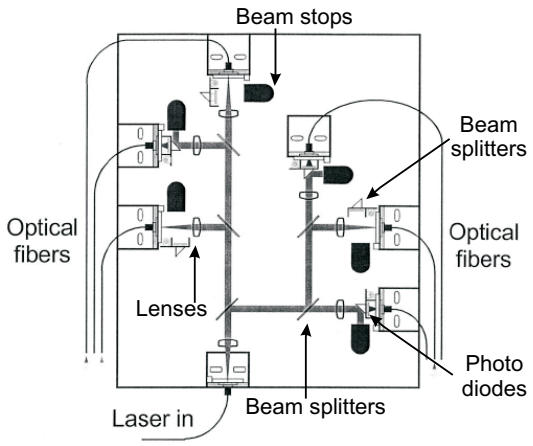

Figure 5.5. *Setup of the beam-splitting light-flux-measureing unit for interstitial PDT at Lund University Medical Laser Centre. Each fiber is used both for delivery of therapeutic light and for collection of light from the tumor in order to measure fluence rates for diagnostics purposes. Adopted from [151].*

PDT635, CeramOptec) is coupled through a fiber into the system where it is divided into six different pathways, each containing an equal amount of light, by appropriate choice of beam splitters. The light fluence rates at the individual fiber tip locations in the tumor are measured for dosimetry purposes. This is realized using six independent photodiodes, which can be rotated into the light path of the incoming light from the treatment fibers (see Fig. 5.5). In this way, each fiber both delivers and collects light. A computer with a dosimetry software is used to control and automatically operate the beam-splitting unit. The programme also performs necessary dosimetry calculations. It calculates the optical fiber positions and minimum treatment time using given tissue optical parameters, as well as the tumor size and shape, light dose for successful treatment and output powers from the fibers.

For some purposes it may be an advantage to use treatment fibers which are thinner than the fiber provided by the commercial treatment laser. However, if the six treatment fibers in Fig. 5.5 are thinner than the input fiber, therapeutic light will be lost. The laser systems described in **Papers I-II** were developed to facilitate the use of optical fibers with core-diameters around 50 μm in connection with interstitial PDT at Lund University Medical Laser Centre. However, the power obtained in the preliminary laser systems was too low in order to obtain complete treatment of the rather large tumors involved in the interstitial PDT trials (see chapter 7, section 7.1.1). Therefore, one of the laser systems was tested in the superficial PDT treatments mentioned above, to verify their ability to be used in connection with PDT. Today, 635 nm laser diodes of the kind used in the developed laser systems, are available with twice the output power of the ones used in the original work.

Chapter 6

Laser-induced fluorescence diagnostics

In 1852, Stokes described the phenomenon of fluorescence from fluorite [152]. Almost 60 years later, fluorescence was observed in animal tissue exposed to UV radiation [153]. Today, laser-induced fluorescence diagnostics is a powerful technique to be used in optical characterization of tissue. With this method, the need for invasive and time consuming biopsies may be reduced and in some applications replaced by noninvasive optical techniques. Fluorescence diagnostics is a natural companion of PDT since the photosensitizers, which accumulate in the diseased tissue, are frequently highly fluorescent. They thus act as fluorescent tumor markers applicable for diagnosis, in addition to precursors for cell damage when activated by light. The work described in **Paper IV** was initiated in order to accomplish a diode laser based system for laser-induced fluorescence imaging of malignant tissue.

6.1 Basic principles

The basic mechanisms of laser-induced fluorescence (and partly of PDT) are shown in Fig. 6.1. When a photosensitizer molecule is irradiated with light matching an absorption band, it is excited from its singlet ground state S_0 to a higher singlet state S_n. The energy levels of molecules consists of a large number of vibrational states with rotational sub levels. This is in contrast to atoms, which have sharp electronic levels. The excitation of the photosensitizer may occur to a higher vibrational singlet state S_n, but it rapidly decays to the lowest rotational-vibrational state by internal conversion (IC). The energy lost from this decay is transferred to surrounding molecules or converted to heat. Now the molecule either relaxes to its ground state by a non-radiative transition (in-

ternal conversion) or a photon is emitted as it returns to S_0. In the latter case, the emitted radiation is known as fluorescence, and it is shifted towards the red (Stokes shift) compared to the excitation wavelength. Since the ground state also contains sub levels, the fluorescence radiation is broad banded. As indicated in the middle part of Fig. 6.1, the excited molecule may transfer to the triplet system (intersystem crossing - IX), even though this transition is spin-forbidden. It occurs because of the small energy separation between the states. From the lowest triplet state, the molecule may relax to its ground state under the emission of a photon. However, this transition is again spin-forbidden, which results in a long-lived, meta-stable lowest triplet-state. When a molecule relaxes from the first excited triplet state to its singlet ground state under the emission of a photon, the emitted radiation is called phosphorescence.

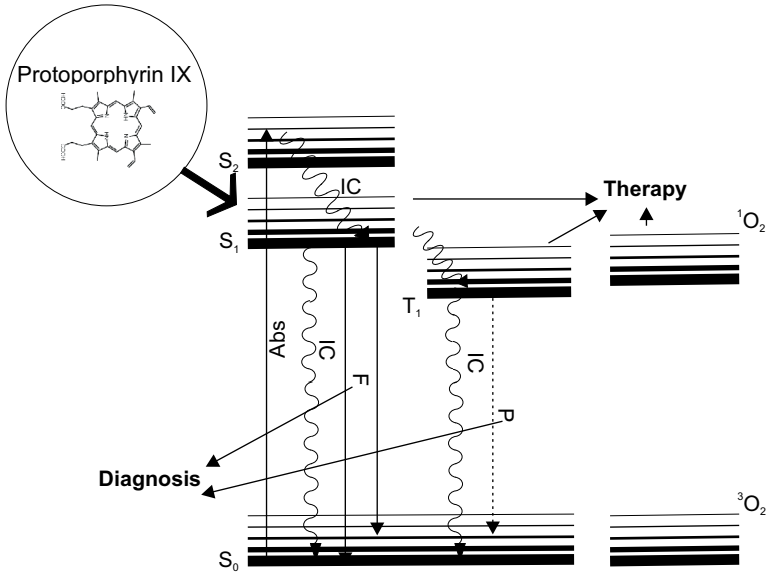

Figure 6.1. *Simplified diagram showing the decay paths from an excited state of a (photosensitizer) molecule. S_n: Singlet states; T_n: Triplet states; Abs: Absorption; F: Fluorescence; P: Phosphorescence; $^3O_2$: Triplet oxygen (ground state); $^1O_2$: Singlet (excited) oxygen.*

To the right in the figure, the triplet ground state $^3O_2$ and the excited singlet state $^1O_2$ of molecular oxygen are shown. The arrows indicate the possibility for transfer of energy from the excited states of the photosensitizer to the surrounding molecular oxygen, whereby the mechanisms of PDT are initiated (see chapter 5). Other arrows indicate that the emitted radiation can be used for diagnostics.

6.2 Tissue autofluorescence

As indicated in the introduction to this chapter, mammalian tissue emits fluorescence when irradiated with UV (or near UV) radiation. The emitted fluorescence is a broad-band blue-green radiation centered around $\sim 490\,\text{nm}$, and denoted tissue *autofluorescence*. An example of a tissue autofluorescence spectrum is shown in Fig. 6.2(a), which has been recorded in connection with a PDT treatment of a skin cancer at Lund University Medical Laser Centre just before the application of ALA. The spectrum is recorded 10 mm outside the visible boundary of the lesion. For comparison, Fig. 6.2(b) shows the fluorescence spectrum recorded in the center of the malignant lesion four hours after the application of ALA. The latter spectrum shows the dual peaked fluorescence of the ALA-induced tumor marker PpIX in addition to to the autofluorescence. The fluorescence from the tumor marker is easy distinguished from the autofluorescence. The autofluorescence originates from the endogenous fluorophores in tissue, such as tryptophan, elastin, collagen, β-carotene, NADH, and endogenous porphyrins. The complex composition and nature of living tissue, makes the interpretation of autofluorescence spectra difficult. Furthermore, absorption by the tissue chromophores (see section 5.1.1) of the excitation light and of the emitted fluorescence may cause attenuation and distortion of the observed fluorescence signal. The dominating contributor in the autofluorescence spectrum, is determined by the excitation wavelength, such that e.g. NADH is dominating for excitation at 365 nm (Mercury line) and collagen/elastin dominates for excitation wavelengths around 337 nm (nitrogen laser). Although the autofluorescence is broad-banded, a wavelength shift towards the red part of the spectrum has been observed for some types of malignant tumors [154]. Furthermore, malignant and premalignant lesions are characterized by a decreased overall autofluorescence intensity as compared to normal tissue [155].

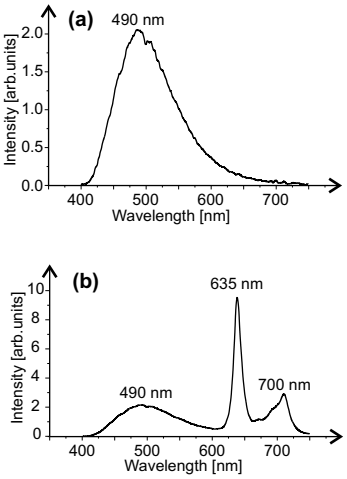

Figure 6.2. *Fluorescence spectra from (a) endogenous fluorophores in tissue (tissue autofluorescence) and (b) PpIX in tissue. PpIX emits its fluorescence at 635 nm and 700 nm. In (b) some autofluorescence is present since the spectrum has been recorded in living tissue.*

6.3 Instrumentation

When choosing the instrumentation, for fluorescence diagnostic measurements, several factors must be considered. First, the excitation wavelength and an appropriate light source must be determined. Moreover, the detection principles must also be evaluated and adopted into a clinical environment. The instrumentation may be intended for either point-monitoring, where the fluorescence from a single spot is recorded, or for imaging, where a larger area, such as the entire lesion, is considered.

6.3.1 Excitation light sources

The choice of wavelength for an excitation source depends on whether the target is the tissue autofluorescence (or one of its components) or the excitation of fluorescence from a tumor marker, such as the endogenous photosensitizer ALA-induced PpIX. Excitation light sources for fluorescence diagnostics can be divided into two groups: lamps and lasers. The broad-band near-UV Xenon lamp may be filtered to yield an appropriate excitation wavelength. Also one of the discrete lines, such as the 405 nm line for excitation of PpIX fluorescence or the 365 nm line for excitation of autofluorescence (especially NADH), from the Mercury lamp is an option.

Alternatively, lasers can be used. These light sources are attractive for fluorescence diagnostics due to their high intensity in a narrow wavelength range and due to the possibility for fiber guidance of the excitation light, such that endoscopical sites becomes accessible. A lot of possibilities are available. Continuous wave sources, such as the Krypton-Ion or the Helium-Cadmium lasers have several appropriate lines for fluorescence diagnostics (e.g. 337 nm and 407 nm in the former case or 325 nm and 442 nm in the latter). Pulsed lasers in the near-IR are interesting, since high peak powers can be obtained and used for higher harmonics generation with high efficiencies by pumping nonlinear crystals (see chapter 4 and remember $P_{2\omega} \propto P_{\omega}^2$). Thereby high intensities in the UV-blue may be generated for fluorescence excitation. Furthermore, by applying a pulsed excitation source, the detection may be gated, such that the influence of ambient light in a clinical environment can be suppressed during measurement (see section 6.3.2). Examples of pulsed sources based on this technology are the frequency tripled Nd:YAG laser (355 nm) for excitation of autofluorescence, the frequency doubled alexandrite laser (390 nm), the UV eximer laser (308 nm), and the nitrogen laser (337 nm), which may be used to pump a dye in order to obtain the right wavelength for the purpose. The eximer laser is large and contain dangerous gases, which make it unappropriate for clinical uses. However, high pulse energies can be obtained, which makes it a candidate for fluorescence imaging (see section 6.3.2). Finally, diode lasers may be used for fluorescence diagnosis. Diode lasers are far more simple, compact, and easy to operate than any of the lasers mentioned above. As discussed in chapter 2, GaN-based diode lasers emitting in the UV-blue recently became available. In [156] a compact diode laser-based system is described for point-monitoring purposes. The system employs an integrated spectrometer for the monitoring of the collected fluorescence. One drawback is that the system does not provide gated detection. There are, to my knowledge, no examples of diode laser-based systems for fluorescence imaging.

6.3.2 Detection principles

As indicated above, two methods, point-monitoring and imaging, exists for detecting the excited fluorescence. There are no commercial point-monitoring systems available. However, the imaging systems, which are more interesting in a clinical perspective since they provide more information, exists in several commercial variants (e.g. HyperSpectral Diagnostic Imaging®, Science and Technology Int., Honolulu, HI, USA; Cerviscan™, LifeSpex Inc., Bothell, WA, USA; LIFE, Xillix Technologies Corp, Richmond, BC, Canada; D-Light/AF system, Karl Storz, Tuttlingen, Germany). Common for these systems are their comprehensive sizes and weights. In addition they lack the implementation of an automatic real-time evaluation system. Some of the systems provide the raw image of the fluorescence to be evaluated by the clinician while others use complicated algorithms in order to outline the borders and areas of lesions.

Several systems for laser-induced fluorescence diagnostics have been developed at Lund University Medical Laser Centre. For point-monitoring measurements for diagnostic purposes of malignant and premalignant lesions, a nitrogen laser (3 ns at 10 Hz) is usually employed. It is either used alone (autofluorescence) for in combination with a dye laser tuned to 405 nm (PpIX) [157, 158]. In the system developed in Lund, the excitation light and the emitted fluorescence are transmitted through the same 600 μm fiber. A dicroic mirror and an optical filter separates the fluorescence from scattered excitation light. The collected fluorescence is dispersed in a spectrometer and detected with an intensified CCD camera. Also the newly developed diode laser-based system has been used in clinical measurements [156]. Again, a 600 μm fiber is used for both excitation light and collection of fluorescence. A CCD detects the dispersed fluorescence with a resolution of 5 nm, which is adequate for the medical monitoring.

For fluorescence imaging purposes, a frequency doubled alexandrite laser tuned to 390 nm is useful for pulsed excitation below 400 nm. In the system developed at Lund University Medical Laser Centre such a laser is employed. The pulse energy of the system is around 1 mJ, which is approximately a factor of 10^3 more than for the point monitoring system, in order to obtain real-time imaging of entire lesions. The alexandrite laser is large and heavy (> 200 kg) and in addition it needs water cooling. Multi-color fluorescence imaging is possible via simultaneous acquisition of spatially identical images, using different optical bandpass filters [159]. The system is shown in Fig. 6.3. It uses beam splitting optics to produce four identical images, each of which are filtered in separate wavelength bands. The four images are then captured on the same image-intensified CCD camera, the gating of which is synchronized with the excitation light source. A color video camera

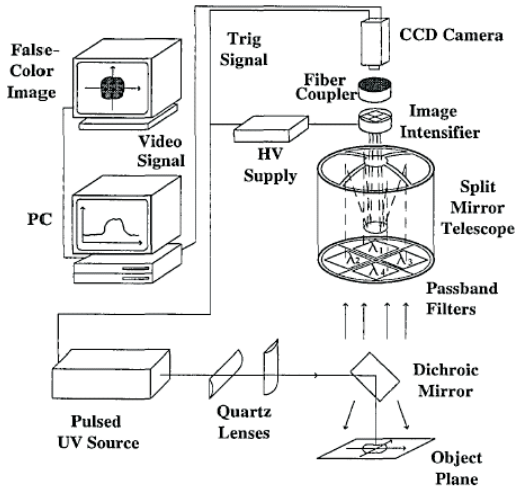

Figure 6.3. *Multi-color fluorescence system at Lund University Medical Laser Centre. The excitation light source is currently a frequency doubled alexandrite laser at 390 nm. From [159].*

record the ordinary white light reflection image, which finally can be mixed with the fluorescence images. Usually three wavelength bands are applied: One that is related to the photosensitizer fluorescence (i.e. red band), one related to the autofluorescence (i.e. blue-green band), and one band in the green-yellow, which is used for subtraction of that part of the autofluorescence signal which overlaps the photosensitizer spectrum (see also Fig. 6.2). An optimized contrast function is then defined by appropriate relations of the intensity in the various bands, which yields a measure for the malignancy in the tissue. High values of the intensity in the red band and low values in the blue-green indicates malignant tissue, as discussed previously. The final image, which is a mixture of the white-light image and the fluorescence images, is updated in real-time at a rate of up to eight images per second. See e.g. [159] for clinical measurements using this system in connection with ALA-PDT.

It would be interesting to develop a compact, easy to operate, diode laser-based fluorescence imaging system for medical diagnostic applications. This was indeed the intention when the project described in **Paper IV** was initiated. However, the first generation system was not pulsed and did not provide enough power to be used for imaging purposes. Results from the experiments concerning pulsing of diode lasers suggest that shorter pulses and higher peak power may still be obtainable (see section 2.6.4), and more work is thus necessary in this area.

6.4 Clinical applications

As indicated above, laser-induced fluorescence has the ability to be used for diagnosis of malignant tissue. The autofluorescence is usually lower in malignant tissue than in healthy tissue and the contrast may be enhanced by the use of fluorescent tumor markers, such as ALA-induced PpIX. In the case of skin lesions, such as BCCs, this may then be used in the delineation of tumor boundary, which is not always possible to discriminate for the unaided eye. In connection with PDT and interstitial PDT, the fluorescence detection can be used as a real-time indicator for the photosensitizer accumulation before and consumption during the treatment.

In chapter 7 the clinical possibilities of the blue diode laser-based system developed during this Ph.D. is evaluated. Suggestions for further development and possibilities for clinical implementation in connection with a fluorescence imaging system will be discussed.

Chapter 7

Diode laser-based systems for PDT and laser-induced fluorescence diagnostics

The diode laser systems described in **Papers I-II** were tested in preliminary clinical trials involving interstitial PDT and superficial PDT, respectively. The interstitial PDT was performed at the University Hospital in Lund (SE) using the system from **Paper I** in the treatment of colon adenocarcinomas inoculated into the hind legs of rat. The PDT was performed at Marselisborg Hospital in Århus (DK) using the system from **Paper II** in the treatment of superficial BCC in human. The results from these clinical trials are discussed in section 7.1. Unfortunately, no clinical trials involving laser-induced fluorescence diagnostics, using the blue diode laser-based system described in **Paper IV**, were performed. In section 7.2, an evaluation of the clinical possibilities of this system are given.

7.1 Diode laser systems for PDT

Two diode laser systems for ALA-PDT were developed. The first generation system (**Paper I**) was based on a single broad area laser at 635 nm exposed to phase conjugate feedback. The second generation system (**Paper II**) was based on the coupling of two identical external-cavity laser diode systems, such that the output power was approximately doubled as compared to the first system. In the following sections, the clinical results using these two systems, are described.

7.1.1 Interstitial PDT of colon adenocarcinomas

Preliminary experimental animal trials were performed at The Department of Oncology, Lund University Hospital, Lund in collaboration with Dr.med. K. Svanberg. The trials were performed using the first generation system described in **Paper I**. Unfortunately, the output power from this system (through a 50 μm core-diameter fiber) was only 80 mW. This turned out not to be sufficient for complete treatment within a reasonable period of time of the large tumors involved in the interstitial PDT trials. However, two treatments were initiated and they are shortly reviewed here.

Animals and drug

Two Wistar/Furth rats (Rat I and Rat II), with colon adenocarcinoma inoculated into the muscles of each hind leg, were treated. More rats were included in the trial, but they were treated with a conventional laser source (CeramOptec, Ceralas PDT635 through an optical fiber with core-diameter of 600 μm). The sizes of the tumors were approximately 3 cm^3 each. One tumor was treated with interstitial ALA-PDT, while the other served as a control tumor for histopathological and statistical tumor examination. The rats were injected intra peritoneally with ALA at a dose of 100 mg/kg body weight 3 hours before treatment. Both animals were under general anaesthesia during the procedure. They were put to sleep using chloral hydrate and Temgesic was used for pain relief.

Interstitial PDT system

Interstitial PDT was performed using the multiple-fiber system shown in Fig. 5.5. The light source from **Paper I** delivered the therapeutic light through a 50 μm optical fiber. The total output power from the fiber of this system was only around 80 mW, which was insufficient to completely treat the large tumors within a reasonable time period. When the conventional laser system is coupled into the multiple-fiber system, approximately 50-160 mW is extracted from each of the 6 fibers [146]. This results in a treatment time around 5-40 minutes depending on light dose, tumor geometry and amount of power in the treatment fibers.

Interstitial PDT procedure

After 3 hours of build-up of PpIX following the injection of ALA, the animals were treated with interstitial PDT. The skin covering the tumors was shaved to avoid hair in the operating field. Three treatment fibers were carefully placed in the calculated positions. Also, a fiber for fluorescence measurements using the nitrogen-laser pumped dye laser with an excitation wavelength of 405 nm (see section 6.3.2) was inserted. Fig. 7.1 shows a picture of the

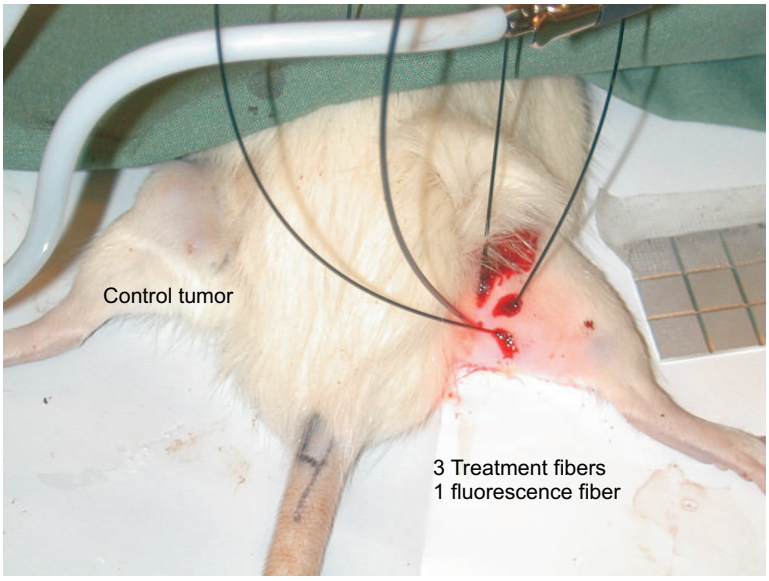

Figure 7.1. *Interstitial PDT treatment of colon adenocarcinoma in muscle of rat hind leg. Here three treatment fibers and one fiber for fluorescence measurements are used.*

treatment situation. The first rat was treated for 15 minutes and the second rat was treated for 30 minutes. The treatment duration was limited due to the hazards of prolonged anaesthesia. For a successful treatment the treatment time should have been much longer (several hours), due to the low power of the laser. The treatment was interrupted in time intervals of 30 seconds to measure the light fluence rate and the photo bleaching of PpIX within the tumor. The animals were sacrificed three days post treatment and both control and treated tumors were removed for histopathological examination.

Laser-induced fluorescence

The fluorescence spectra were obtained and recorded in the wavelength range 400-800 nm using the system described in section 6.3.2. The fluorescence from twenty laser pulses was integrated to obtain spectra with high signal-to-noise ratios. The recorded spectra were displayed on a screen and stored in a computer for subsequent evaluation. Fluorescence spectra were acquired just before and every 30 seconds during the treatment. For illustration, the first six fluorescence measurements obtained from Rat I are shown in Fig. 7.2. The uppermost curve corresponds to $t = 0$ sec and the lowest curve corresponds to $t = 150$ sec. It is observed that the photosensitizer is bleached during treatment.

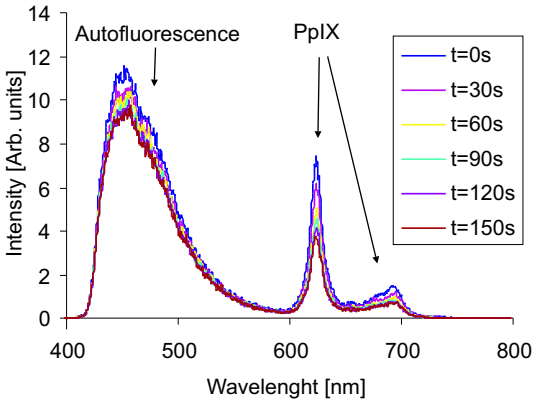

Figure 7.2. *Laser-induced fluorescence measurements before and during PDT treatment. The fluorescence is measured every 30 seconds during treatment. Uppermost curve corresponds to 0 sec, lowest curve to 150 sec. It is observed that the PDT treatment bleaches the photosensitizer away.*

Tumor volume change

The tumor sizes were measured with sliding callipers just before the treatment and again when the animals were sacrificed and the tumors removed. The tumor volumes were calculated from the approximative formula $\frac{4}{3}\pi(a \times b^2)$, where a is the half-width of the maximum tumor dimension, and b is the half-width of the minimum dimension of the tumor. The measured tumor volumes before and after treatment are shown in Table 7.1.

Table 7.1. *Measured tumor volumes pre and 3 days post interstitial PDT treatment.*

Rat no.	Volume of treated tumor	Volume of control tumor
PRE		
I	$3.3\,\mathrm{cm}^3$	$5.0\,\mathrm{cm}^3$
II	$2.8\,\mathrm{cm}^3$	$4.1\,\mathrm{cm}^3$
3 DAYS POST		
I	$5.7\,\mathrm{cm}^3$	$5.9\,\mathrm{cm}^3$
II	$4.1\,\mathrm{cm}^3$	$3.8\,\mathrm{cm}^3$

The growth rates of the individual tumors were calculated by forming the ratio between tumor volume 3 days post treatment and tumor volume pre treatment. This value was used as an estimation (normally together with the histopathological examination) of the therapeutic efficiency. The volume increase/decrease of the four

tumors are shown in Table 7.2.

Table 7.2. *Change in tumor volumes.*

Rat no.	Treated tumor	Control tumor
I	+ 73 %	+ 18 %
II	+ 46 %	- 7 %

Unfortunately, but as expected, these results are not encouraging. Both treated tumors show a profound growth during the three days after treatment. The volume increment of the treated tumors is due to the insufficient treatment power and the short treatment time. To improve the performance of the laser system, power must be increased. Possibilities for this are discussed in section 7.1.3.

Photobleaching

Despite the poor results regarding tumor volume reduction, the laser-induced fluorescence measurements indicate that the PpIX was partly bleached away as a result of the PDT treatment. Fig. 7.3 shows the photo bleaching of the 635 nm peak of the PpIX fluorescence during treatment (15 min.). The remainder of PpIX fluorescence indicate that the treatment time should have been longer or that a more powerful laser is needed.

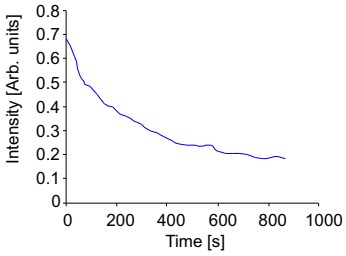

Figure 7.3. *Photo bleaching of the PpIX 635 nm fluorescence peak measured with laser-induced fluorescence during the interstitial PDT treatment.*

7.1.2 PDT of superficial BCC

The treatments were performed at The Department of Dermatology, Marselisborg Hospital, Århus in collaboration with Dr.med. H. Sølvsten and Prof.dr.med. P. Bjerring.

Lesions

The patient, a 37 year old male, had three lesions on the shoulder, diagnosed as superficial BCCs, see picture in Fig. 7.4 (a). One lesion was treated with PDT and had a diameter of 1 cm (upper lesion in the picture). A safety margin of 7 mm was used around the lesion, which resulted in an irradiation area with a radius of 12 mm, or a total treatment area of 4.5 cm^2. The remaining two lesions had similar areas and were treated with a conventional modality.

Treatment procedures

Biopsies were taken from the lesions. ALA was mixed in a oil-in-water emulsion to a 20 % concentration which was applied to the

lesion that should be treated with PDT. Two lesions were treated with electrocautery and curretage (see section 5.2.1). The PDT-irradiation procedure was performed 4 hours after the application of ALA. The polarization coupled diode laser system was used as the light source. The laser was irradiating at 635 nm and the light was conducted through a 200 μm optical fiber. The intensity profile of the output from the fiber was verified to be top hat-like so that a uniform light intensity was applied to the treatment area. By adjusting the distance between the fiber tip and the patient, the size of the light field could be varied. A total light dose of 60 J/cm^2 was supplied in a single illumination session. The fluence rate was kept low with a value of 56 mW/cm^2, ensuring minimal light-induced thermal effects on the tissue. The total treatment time was 18 min, since:

$$\text{Dose}\,[\text{J/cm}^2] = \text{Fluence rate}\,[\text{W/cm}^2] \times \text{Treatment time}\,[\text{s}]\,. \tag{7.1}$$

Preferably, the treatment time should be shorter. This could be accomplished e.g. by using a fluence rate of 100 mW/cm^2, which is still below any hyperthermal rate, and which would result in at treatment time of 10 min. However, since the maximum output power through the fiber from our laser system was 250 mW, this was not possible.

Tolerability assessment

Pain and discomfort
During the PDT procedure no conventional local anesthesia was supplied to the patient. However, the patient did experience pain during the light exposure. These sensations were simply and readily relieved by spraying with water of about 15-20°C.

Course of healing
The course of healing was followed by 1-month, 3-months, and 12-months follow-up visits, see Fig. 7.4 (b) and (c) for the latter two. Full remission was observed in all three lesions at all follow-ups. The lesion treated with PDT was healing faster than the remaining two.

Cosmetic outcome
The cosmetic outcome can be evaluated from the 12-months follow-up (Fig. 7.4 (c)). Treatment of these three lesions was in favor for PDT, which resulted in better outcome than electrocautery and curretage. There is almost no scar formation and only a slight hyper-pigmentation where the PDT procedure was conducted. Furthermore, the skin is smooth and even. In the case of the other two treatment areas, where electrocautery and curretage has been applied, the skin show both scar formation and hyper-pigmentation.

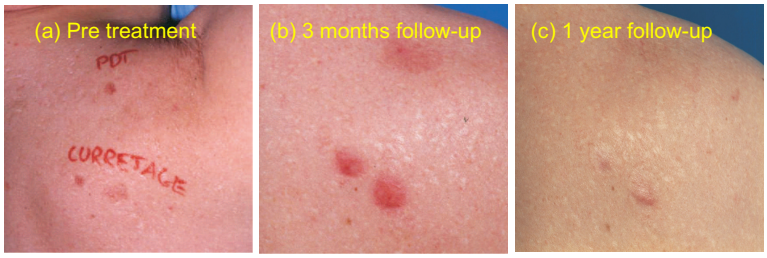

Figure 7.4. *Treatment of superficial BCCs at Marselisborg Hospital in Århus with PDT using the laser system from* ***Paper II*** *compared to electrocautery combined with curretage. (a) Pre treatment, (b) Three months follow-up, (c) One year follow-up.*

7.1.3 Clinical evaluation of PDT systems

As is apparent from the description of the preliminary trials, the power output of the diode laser systems for PDT must be increased in order for them to become interesting for interstitial PDT. The power should be comparable with the power from the commercially available PDT lasers. These lasers have output powers in the range of 1-2 W through 400-800 μm core diameter fibers. Thus, an output power around 1 W through a 50-100 μm fiber is desirable. The power of the first generation system was far too low to treat the large, solid adenocarcinomas in the interstitial PDT trial. The second generation system was successful in the treatment of superficial BCCs, although the treatment time was longer than desired.

Today, broad-area laser diodes at 635 nm are available with twice the output power of the diodes used in the second generation, polarization coupled system for PDT. Implementation of the novel laser diodes will result in a laser system capable of yielding at least 0.5 W through a 50 μm fiber ($2 \times 0.5 \times 0.7 \times 0.8$ assuming that 70 % is extracted in the output beam and 80 % is coupled through the fiber). Such a system is indeed interesting for superficial PDT of thin lesions (but in this case there is no need for a thin fiber) and it may be sufficient for treatment of some solid tumors.

However, a better way to accomplish a suitable diode laser-based system for interstitial PDT may be to construct a system with six independent external-cavity diode lasers, each coupled to separate treatment fibers. With such a system, several hundreds of mW can be extracted through each treatment fiber. The treatment fibers may be as thin as desired, and even single-mode.

In conclusion, several possibilities exist for the development of a compact diode laser-based system meeting the requirements for interstitial PDT.

7.2 Frequency doubled diode laser system for laser-induced fluorescence diagnostics

In **Paper IV** a diode laser system at 405 nm is described, which is based on frequency doubling of an external-cavity laser diode with double grating feedback (**Paper III**). The work leading to the design and construction of this system was initiated in order to design a diode laser-based system for laser-induced fluorescence imaging in connection with ALA-PDT. Such a system should be pulsed with a maximum pulse width of 1 μs and a repetition rate around 25-50 Hz [45]. The pulse energy of an existing system at Lund University Medical Laser Centre is on the order of 1 mJ for the frequency doubled alexandrite laser (imaging) and 1-2 μJ for the nitrogen laser-pumped dye laser (point-monitoring). The system described in **Paper IV** does not match these specifications in its current form. The laser system is not yet pulsed and the output power is still too low. Therefore, it is premature to test this system in a clinical setup. However, by further development of a second generation, pulsed system, it may be ready for clinical trials.

7.2.1 Evaluation of clinical possibilities

The blue output power must be increased and the system must be pulsed to have clinical relevance. Operating the pump laser in pulsed mode will lead to an increase in SHG efficiency due to the high peak powers. However, this experiment remains to be completed. Table 7.3 collects estimations of the parameters obtainable for a pulsed system based on the experiments described in chapter 2, section 2.6.4 and in **Paper IV** assuming a repetition rate of 50 Hz and a pulse length of 1 μs.

Table 7.3. *Estimations of obtainable peak powers (P_p), pulse energies (E), and average powers (P_{av}) of the frequency doubled diode laser system in its current form. ω and 2ω refer to the fundamental (810 nm) beam and the second harmonic (405 nm) beam, respectively.*

P_p^{ω} [W]	$P_{p,out}^{\omega}$ [W]	$\times P_{cw,out}^{\omega}$ [-]	$P_p^{2\omega}$ [mW]	E^{ω} [μJ]	$E^{2\omega}$ [μJ]	P_{av}^{ω} [mW]	$P_{av}^{2\omega}$ [μW]
15	7.5	19	180	7.5	0.2	0.4	10
20	10	25	312	10	0.3	0.5	15

$P_{p,out}^{\omega}$ is the near-infrared peak power available for pumping the KTP crystal assuming that 50 % of the power is coupled out of the

system; "$\times$ $P^{\omega}_{cw,out}$" is $P^{\omega}_{p,out}$ divided by the cw power of approximately 400 mW (from **Paper IV**); $P^{2\omega}_{p} = (\times P^{\omega}_{cw,out})^2 \times 0.5\,\mathrm{mW}$ is the estimate of obtainable blue peak power, since a pump power around 400 mW yields a second harmonic power around 0.5 mW (see **Paper IV**). From these estimations, it is apparent that if the system is pulsed in its current form, it may be used for point-monitoring purposes. However, for fluorescence imaging purposes the average power must be increased more than is possible with the system in its current form. The second harmonic power may be increased by using an AR coated BAL so that the external-cavity diode can be driven at higher currents without destruction of the improved coherence. Furthermore, a BAL with higher output power than the one used in this work may be applied. We may also use a grating with lower diffraction efficiency, thus increasing the amount of power in the zeroth order output beam of the double grating feedback laser. Finally, the results may be improved in terms of blue output power by implementing the nonlinear crystal in a resonator enhanced setup.

The simplest solution is to apply the new high-power GaN diode lasers at 405 nm for laser-induced fluorescence diagnostics. As mentioned in chapter 2, section 2.3.3, an engineering sample with an output power of 60 mW and an estimated lifetime that exceeds a couple of thousands hours has recently become available from the Japanese company Nichia. Such a sample should be tested for the application and it should be verified whether these lasers are capable of meetinig the specifications with respect to pulsing and pulse energy. It is estimated (but not guaranteed) by Nichia that a peak power of approximately twice the cw power can be extracted from the laser if it is pulsed [31]. Assuming a peak power around 120 mW from the Nichia diode yields a pulse energy of 0.12 μJ and an average power of 6 μW if the repetition rate and the pulse length are 50 Hz and 1 μs, respectively. These numbers are lower than for the pulsed external-cavity diode laser system. The estimations are uncertain and have not been experimentally verified.

To conclude, a diode laser-based system for laser-induced fluorescence imaging may be constructed by a frequency doubled external-cavity diode laser system. With such a system, the specifications may be obtained by improving the current system using one or more of the suggestions mentioned above. If pulsed, the blue GaN diode may be suitable for point-monitoring purposes. However, the power is still too low, even in pulsed mode, for the laser to be used for imaging purposes, where a pulse energy of at least 0.5 mJ is necessary.

As a final remark it should be mentioned that the double grating feedback system has interesting potential for efficient generation of UV light, since the double grating feedback scheme also applies to lower, e.g. red or green, wavelengths. Such a laser would

be interesting, e.g. as a source for disinfection of catheters with UV light. This application employs the germicidal effectiveness of UV which relies on the fact that light around 200-300 nm (the "germicidal range") is absorbed by DNA with a peak effectiveness around 260 nm. This causes disruption in the DNA chain so that when the cell undergoes mitosis (cell division) the replication of DNA is inhibited. In this way bacteria may be removed effectively from catheters. UV light has many commercial applications in society. The major ones are: UV disinfection of water and air, UV curing of inks and coatings, UV disinfection of foods, UV-based advanced oxidation destruction of pollutants in water and air.

Acknowledgements

First of all, I would like to thank my supervisors at Risø, Peter E. Andersen and Paul Michael Petersen, for motivation and inspiration throughout the years. I have enjoyed our many fruitful discussions, the scientific as well as the personal ones. Furthermore, my gratitude is directed towards my supervisors from Lund: Stefan Andersson-Engels, for his inspiration, and good spirits, and Katarina Svanberg for introducing me to the clinical aspect of my work and for her colorful and caring nature. My sincere gratitude to all of you for the understanding, support, and space given to me in the dark and difficult times around my fathers disease and depart from this life. It meant a lot to me.

I have been fortunate to enjoy a collaboration with prof.dr.med. Peter Bjerring and dr.med. Henrik Sølvsten from Marselisborg Hospital. I learned a lot from our clinical collaboration and for that I am grateful.

Thanks to former and present fellow students at Risø and from Lund, without whom the past couple of years would not have been the same: Frederik D. Nielsen, Bo T. Christensen, Peter Lodahl, Steven R. Kitchen, Kim G. Jespersen, Per Malm, Jesper Holm, Søren Blaaberg, Sussie Juul Jensen, Thomas Nikolajsen, Niels Kjærgaard, Morten Bache, Maria Stenberg, Sara Pålsson, and Marcelo Soto Thompson. The rest of my colleagues at OPL also receive my gratitude for decent behavior and good spirits. Especially, Lone Astradsson, for keeping me in good shape, Christian Pedersen for inspiring scientific discussions and for training my crystals when they were lazy, and Bitten Skaarup for proofreading parts of this manuscript. My appreciations to the competent technical staff at OPL: Bjarne Sass, for his skilful work and cheerfulness; Jess Thorsen, and Finn Pedersen, for their help with the electronics. My roommate, Frederik D. Nielsen, deserves a special thanks for many interesting discussions on life, science, and beyond.

Finally, I would like to express my most sincere gratitude towards my mother, my brother, and my beloved Anders for their infinite support and love and for their patience with me. Thank

you, Anders, for rewarding discussions on the biological aspects of my work and for always being there for me.

This research project was supported by the Danish Technical Research Council, grant number 9901433.

Comments on the Papers

The work performed during this Ph.D. has resulted in the preparation of six scientific papers. The contents of these papers and the authors contributions to them are summarized below.

The prototype PDT laser was developed and is described in **Paper I**. The author developed the laser system, prepared the manuscript, and brought the laser system to the university hospital in Lund. Here she participated in preliminary clinical trials in connection with interstitial PDT treatments of solid tumors in rat. The results from these trials are not published, but are described in this thesis in Ch. 7. It was quickly realized that in order to obtain an effective treatment, the power of the system should be increased. Thus, a second generation system was developed, which couples the output from two separate external-cavity laser diodes by means of polarization coupling. This work is published in **Paper II**. The author developed the laser system yielding the results described in this paper and prepared the manuscript. The second generation system was brought by the author to Marselisborg hospital for clinical testing. In this clinical trial, PDT treatment using the second generation PDT laser was compared to a conventional treatment of skin cancer in human. The results from these trials have not been published, but can be found in this thesis in Ch. 7. Following this, the focus was shifted towards the development of a diode laser system for laser-induced fluorescence diagnostics. For this purpose a novel external-cavity configuration was suggested and developed by the author. The novel scheme improved the spatial and temporal coherence of a broad area laser, which then could be used for second harmonic generation, such that the desired wavelength for fluorescence diagnostics could be generated. The novel external-cavity system, which was intended to constitute the pump laser, is described in **Paper III**, which has been prepared by the author. Finally, the second harmonic generation was carried out using the developed pump laser described in **Paper III**. The first results from this work is presented in **Paper IV**, which has been prepared by the author. A lot of different external-cavity configurations have been tested during this Ph.D. work. Sometimes it was observed that the single output lobe os-

cillation was preserved even though the spatial filter was removed from the cavity. Similar observations had been made earlier and a theory explaining these findings was developed. This theory is presented in **Paper VI**. The author have contributed to this work with experimental measurements and help with the manuscript preparation. Finally **Paper V** is somewhat beyond the scope of this thesis. This paper is an example of the versatility of the external-cavity feedback laser diodes. The laser system described in **Paper V** was developed for display purposes, but the main core of the system is similar to (half of) the PDT laser described in **Paper II**. The author contributed to this work with experiments and help with the manuscript preparation.

Bibliography

1. R. N. Hall, G. E. Fenner, J. D. Kingsley, T. J. Soltys, and R. O. Carlson, *Coherent Light Emission From GaAs Junctions*, Phys. Rev. Lett. **9,** 366–368 (1962).
2. M. I. Nathan, W. P. Dumke, G. Burns, F. H. Dill Jr., and G. Lasher, *Stimulated emission of radiation from GaAs p-n junctions*, Appl. Phys. Lett. **1,** 62–64 (1962).
3. T. M. Quist, R. H. Rediker, R. J. Keyes, W. E. Krag, B. Lax, A. L. Whorter, and H. J. Ziegler, *Semiconductor maser of GaAs*, Appl. Phys. Lett. **1,** 91–92 (1962).
4. G. P. Agrawal and N. K. Dutta, *Semiconductor lasers*, 2nd ed. (Van Nostrand Reinhold, New York, USA, 1993).
5. P. Unger, in *High-Power Diode Lasers: Fundamentals, Technology, Applications*, 78 ed., R. Diehl, ed., (Springer-Verlag, Berlin, Germany, 2000).
6. A. Jakubowicz, *Material and Fabrication-Related Limitations to High-Power Operation of GaAs/AlGaAs and InGaAs/AlGaAs Laser Diodes*, Mat. Sci. Eng. B **44,** 359–363 (1997).
7. J. Hendrix, G. Morthier, and R. Baets, *Influence of Laser Parameters and Unpumped Regions Near the Facets on the Power Level for Catastrophic Optical Damage in Short Wavelength Lasers*, IEE Proc.-Optoelectron. **144,** 109–114 (1997).
8. M. Chi, B. Thestrup, and P. M. Petersen, *Improvement of the beam quality of a 1000 µm wide broad-area diode laser with self-injection phase locking in an external cavity*, In *High-Power Diode Laser Technology and Applications II*, M. S. Zediker, ed., To appear in Proc. SPIE 5336 (2004).
9. G. H. B. Thompson, *A theory for filamentation in semiconductor lasers including the dependence of dielectric constant on injected carrier density*, Optoelectronics **4,** 257–310 (1972).
10. J. M. Verdiell and R. Frey, *A Broad-Area Mode-Coupling Model for Muliple-Stripe Semiconductor Lasers*, IEEE J. Quan. Elec. **26,** 270–279 (1990).
11. G. E. amd A. Bärwolff amd J. Sebastian and J. Tomm, in *High-Power Diode Lasers: Fundamentals, Technology, Applications*, 78 ed., R. Diehl, ed., (Springer-Verlag, Berlin, Germany, 2000).
12. M. Jansen, P. Bournes, P. Corvini, F. Fang, M. Finander, M. Hmelar, T. Johnston, C. Jordan, R. Nabiev, J. L. Nightingale, M. Widman, H. Asonen, J. Aarik, A. Salokatve, J. Nappi, and K. Rakennus, *High performance laser diode bars with aluminum-free active regions*, Opt. Express **4,** 3–11 (1999).
13. U. Brauch, P. Loosen, and H. Opower, in *High-Power Diode Lasers: Fundamentals, Technology, Applications*, 78 ed., R. Diehl, ed., (Springer-Verlag, Berlin, Germany, 2000).
14. S. Adachi, *Physical properties of III-V semiconductor compounds: InP, InAs, GaAs, GaP, InGaAs, and InGaAsP* (Wiley, New York, USA, 1992).

15. S. L. Yellen, A. H. Shepard, R. J. Dalby, A. Baumann, H. B. Serreze, T. S. Guido, R. Soltz, K. J. Bystrom, C. M. Harding, and R. G. Waters, *Reliability of GaAs-based semiconductor diode lasers: 0.6 - 1.1 μm*, IEEE J. Quantum Electron. **29,** 2058–2067 (1993).
16. J. S. Roberts, J. P. R. David, L. Smith, and P. L. Tihanyi, *The influence of trimethylindium impurities on the performance on InAlGaAs single quantum well lasers*, J. Cryst. Growth **195,** 668–675 (1998).
17. L. J. Mawst, A. Bhattacharya, J. Lopez, D. Botez, and D. Z. Garbuzov, *8 W CW front-facet power from broad-waveguide Al-free 980 nm diode lasers*, Appl. Phys. Lett. **69,** 1532–1535 (1996).
18. C. H. Chen, S. A. Stockman, M. Peanasky, and C. P. Kuo, in *High brightness light emitting diodes, semiconductors and semimetals*, G. B. Stringfellow and M. G. Crawford, eds., (Academic Press, San Diego, CA, USA, 1997), Vol. 48.
19. S. Nakamura, *The blue laser diode* (Springer-Verlag, Heidelberg, Germany, 1997).
20. S. Chichibu, T. Azuhata, T. Sota, and S. Nakamura, *Spontaneous emission of localized excitons in InGaN single and multiquantum well structures*, Appl. Phys. Lett. **69,** 4188–4190 (1996).
21. S. D. Lester, F. A. Ponce, M. G. Craford, and D. A. Steigerwald, *High dislocation densities in high efficiency GaN-based light-emitting diodes*, Appl. Phys. Lett. **66,** 1249–1251 (1995).
22. S. Nakamura, M. Senoh, S. Nagahama, N. Iwasa, T. Yamada, T. Matsushita, H. Kiyoku, Y. Sugimoto, T. Kozaki, H. Umemoto, M. Sano, and K. Chocho, *High-power, long-lifetime InGaN/GaN/AlGaN-based laser diodes grown on Pure GaN substrates*, Jpn. J. Appl. Phys. **37,** 309–312 (1998).
23. A. Usui, H. Sunakawa, A. Sakai, and A. Yamaguchi, *Thick GaN epitaxial growth with low dislocation density by hydride vapor phase epitaxy*, Jpn. J. Appl. Phys. **36,** 899–902 (1997).
24. O. H. Nam, M. D. Bremser, T. Zheleva, and R. F. Davis, *Lateral epitaxy of low defect density GaN layers via organometallic vapor phase epitaxy*, Appl. Phys. Lett. **71,** 2638–2640 (1997).
25. S. Chichibu, T. Azuhata, T. Sota, and S. Nakamura, *Luminescences from localized states in InGaN epilayers*, Appl. Phys. Lett. **70,** 2822–2824 (1996).
26. Y. Narukawa, Y. Kawakami, S. Fujita, S. Fujita, and S. Nakamura, *Recombination dynamics of localized excitons in $In_0.20Ga_0.80N$-$In_0.50Ga_0.95N$ multiple quantum wells*, Phys. Rev. B **55,** 1938–1941 (1997).
27. Y. Narukawa, Y. Kawakami, M. Funato, S. Fujita, S. Fujita, and S. Nakamura, *Role of self-formed InGaN quantum dots for exciton localization in the purple laser diode emitting at 420nm*, Appl. Phys. Lett. **70,** 981–983 (1997).
28. S. Chichibu, K. Wada, and S. Nakamura, *Spatially resolved cathodoluminescence spectra of InGaN quantum wells*, Appl. Phys. Lett. **71,** 2346–2348 (1997).
29. S. Nakamura, *Current status and future prospects of InGaN-based laser diodes*, JSAP International pp. 5–17 (2000).
30. S. Nakamura, *The roles of structural imperfections in InGaN/GaN/AlGaN-based laser diodes grown on GaN substrates with a fundamental transverse mode*, Science **281,** 956–961 (1998).
31. I. Toshiaki, Nichia Corp., Tokyo, Japan. Personal conversation (2004).
32. M. Osinski and J. Buus, *The Linewidth Broadening Factor in Semiconductor Lasers - an Overview*, IEEE J. Quan. Elec. **23,** 9 (1987).
33. G. Agrawal, *Fast-Fourier-transform based beam-propagation model for stripe-geometry semiconductor lasers*, J. Appl. Phys. **56,** 3100–3109 (1984).
34. J. R. Marciante and G. P. Agrawal, *Controlling filamentation in broad-area semiconductor lasers and amplifiers*, Appl. Phys. Lett. **69,** 593–595

(1996).
35. J. R. Marciante and G. P. Agrawal, *Spatio-Temporal characteristics of Filamentation in Broad-Area Semiconductor Lasers*, IEEE J. Quantum Electron. **33,** 1174–1179 (1997).
36. J. R. Marciante and G. P. Agrawal, *Spatio-Temporal characteristics of Filamentation in Broad-Area Semiconductor Lasers: Experimental Results*, IEEE Photon. Technol. Lett. **10,** 54–56 (1998).
37. D. Mehuys, P. Lang, M. Mittelstein, J. Salzman, and A. Yariv, *Self-Stabilized Nonlinear Lateral Modes of Broad Area Lasers*, IEEE J. Quantum Electron. **23,** 1909–1920 (1987).
38. R. M. R. Pillai and E. M. Garmire, *Paraxial-misalignment insensitive external-cavity semiconductor-laser array emitting near-diffraction limited single-lobed beam*, IEEE J. Quantum Electron. **32,** 996–1008 (1996).
39. *Laser diode technical note 1; Beam circularization and astigmatism-correction*, Coherent Inc., Auburn group, CA, USA, http://www.coherentinc.com/Downloads/LaserDiodeTechNote1.pdf.
40. J. M. Verdiell, H. Rajenback, and J. P. Huignard, *Array modes of multiple-stripe diode lasers: A broad-area mode coupling approach*, J. Appl. Phys. **66,** 1466–1468 (1989).
41. X. Tang, J. P. van der Ziel, and A. K. Chin, *Characterization of the array modes of high-power gain-guided GaAs single-quantum-well laser arrays*, IEEE J. Quantum Electron. **32,** 1417 (1996).
42. *Laser diode operator's manual & technical notes*, SDL (now JDS Uniphase), San Jose, CA, USA.
43. D. Hodgson, K. Noonan, B. Olsen, and T. Orosz, *Pulsing a laser diode*, 2002, application note No. 11 from Lightwave, http://www.ilxlightwave.com/productData/appnotes/Application%20 Note%2011%20 for%20web.PDF.
44. P. W. Milonni and J. H. Eberly, *Lasers* (John Wiley and Sons, Inc., N.Y., USA, 1988).
45. S. Andersson-Engels, Physics Department, Lund Institute of Technology, Sweden. Personal conversation (2004).
46. R. M. R. Pillai, Ph.D. thesis, University of Southern California, 1995.
47. P. M. Fishbane, S. Gasiorowicz, and S. T. Thornton, *Physics for scientists and engineers, extended* (Prentice-Hall International Editions, New Jersey, USA, 1993).
48. E. Samsøe, P. Malm, P. E. Andersen, P. M. Petersen, and S. Andersson-Engels, *Improvement of brightness and output power of high-power laser diodes in the visible spectral region*, Opt. Commun. **219,** 369–375 (2003).
49. I. Ikushima and M. Maeda, *Lasing spectra of semiconductor lasers coupled to an optical fiber*, IEEE J. Quantum Electron. **15,** 844–845 (1979).
50. C. J. Chang-Hasnain, J. Berger, D. R. Scifres, W. Streifer, J. R. Whinnery, and A. Dienes, *High power with high efficiency in a narrow single-lobed beam from a laser array in an external cavity*, Appl. Phys. Lett. **50,** 1465–1467 (1987).
51. V. Raab and R. Menzel, *External resonator design for high-power laser diodes that yields 400 mW of TEM_{00} power*, Opt. Lett. **27,** 167–169 (2002).
52. B. Thestrup, M. Chi, B. Sass, and P. M. Petersen, *High brightness laser source based on polarization coupling of two diode lasers with asymmetric feedback*, Appl. Phys. Lett. **82,** 680–682 (2003).
53. M. Løbel, Ph.D. thesis, Risø National Laboratory, 1998.
54. E. Hecht and A. Zajac, *Optics*, sixth ed. (Addison-Wesley Pub., 1974).
55. M. G. Littman and H. J. Metcalf, *Spectrally narrow pulsed dye laser without beam expander*, Appl. Opt. **17,** 2224–2227 (1978).
56. H. Li, C. Wu, M. B. Snipes Jr., and J. G. McInerney, *Widely tunable, high power external cavity semiconductor lasers*, In *Laser Diode Technology and Applications IV*, D. Renner, ed., Proc. SPIE **1634,** 532–537 (2001).
57. E. Samsøe, P. E. Andersen, S. Andersson-Engels, and P. M. Petersen, *Improvement of spatial and temporal coherence of a broad area laser*

diode using an external-cavity design with double grating feedback, Opt. Express **12,** 609–616 (2004).
58. S. M. MacCormack and J. Feinberg, *High-brightness output from a laser-diode array coupled to a phase-conjugating mirror*, Opt. Lett. **18,** 211–213 (1993).
59. M. Løbel, P. M. Petersen, and P. M. Johansen, *Single-mode operation of a laser-diode array with frequency-selective phase-conjugate feedback*, Opt. Lett. **23,** 825–827 (1998).
60. E. Samsøe, P. Petersen, P. Andersen, S. Andersson-Engels, and K. Svanberg, *A novel diode laser system for photodynamic therapy*, In *LaserTissue Interactions, Therapeutic Applications, and Photodynamic Therapy*, R. Birngruber and H. V. Bergh, eds., Proc. SPIE **4433,** 134–139 (2001).
61. J. Feinberg, *Self-pumped, continous-wave phase conjugator using internal reflections*, Opt. Lett. **7,** 486–488 (1982).
62. S. J. Jensen, M. Løbel, and P. M. Petersen, *Stability of the single-mode output of a laser diode array with phase conjugate feedback*, Appl. Phys. Lett. **76,** 535–537 (2000).
63. M. Løbel, P. M. Petersen, and P. M. Johansen, *Tunable single-mode operation of a high-power laser-diode array by use of an external cavity with a grating and a photorefractive phase-conjugate mirror*, J. Opt. Soc. Am. B **15,** 2000–2005 (1998).
64. A. L. Schawlow and C. H. Townes, *Infrared and optical masers*, Phys. Rev. **112,** 1940–1949 (1958).
65. T. H. Maiman, *Stimulated optical radiation in ruby*, Nature **187,** 493–494 (1960).
66. P. A. Franken, A. E. Hill, C. W. Peters, and G. Weinreich, *Generation of optical harmonics*, Phys. Rev. Lett **7,** 118–119 (1961).
67. L. M. Magid, *Electromagnetic fields, energy, and waves* (John Wiley & Sons, Inc., New York, USA, 1972), Chap. 9.
68. P. M. Petersen and T. Skettrup, *Ulineær optik* (Polyteknisk forlag, Lyngby, DK, 1994).
69. W. P. Risk, T. R. Gosnell, and A. V. Nurmikko, *Compact blue-green lasers* (Cambridge University Press, Cambridge, UK, 2003).
70. D. A. Kleinman, *Nonlinear dielectric polarization in optical media*, Phys. Rev. **126,** 1977–1979 (1962).
71. R. W. Boyd, *Nonlinear optics* (Academic Press, San Diego, CA, USA, 1992).
72. P. D. Maker, R. W. Terhune, M. Nisennoff, and C. M. Savage, *Effects of dispersion and focusing on the production of optical harmonics*, Phys. Rev. Lett. **8,** 21–22 (1962).
73. R. L. Sutherland, *Handbook of nonlinear optics* (Marcel Dekker, inc., New York, NY, USA, 1996).
74. G. D. Boyd and D. A. Kleinman, *Parametric interaction of focused Gaussian light beams*, J. Appl. Phys. **39,** 3597–3639 (1968).
75. F. M. Librecht and J. A. Simons, *Second harmonic generation in birefringent crystals by a Gaussian beam with an elliptical cross section*, IEEE J. Quantum Electron. **11,** 850–852 (1975).
76. A. Steinbach, M. Rauner, F. C. Cruz, and J. C. Bergquist, *CW second harmonic generation with elliptical Gaussian beams*, Opt. Commun. **123,** 207–214 (1996).
77. W. H. Carter, *Electromagnetic field of a Gaussian beam with an elliptical cross section*, J. Opt. Soc. Am. **62,** 1195–1201 (1972).
78. G. D. Boyd, A. Ashkin, J. M. Dziedzic, and D. A. Kleinman, *Second-harmonic generation of light with double refraction*, Phys. Rev. **137,** 1305–1320 (1965).
79. J. E. Bjorkholm, *Optical second-harmonic generation using a focused Gaussian laser beam*, Phys. Rev. **142,** 126–136 (1966).
80. Y. Uematsu, *Nonlinear optical properties of $KNbO_3$ single crystal in the orthorhombic phase*, Jpn. J. appl. Phys. **13,** 1362–1368 (1974).
81. J. A. Armstrong, N. Bloembergen, J. Ducuing, and P. S. Pershan, *In-*

teractions between light waves in a nonlinear dielectric, Phys. Rev. **127,** 1918–1939 (1962).
82. N. Bloembergen and A. J. Sievers, *Nonlinear optical properties of periodic laminar structures*, Appl. Phys. Lett. **17,** 483–486 (1970).
83. C. F. Dewey Jr. and L. O. Hocker, *Enhanced nonlinear optical effects in rotationally twinned crystals*, Appl. Phys. Lett. **26,** 442–444 (1975).
84. M. Okada, K. Takizawa, and S. Ieiri, *Second harmonic generation by periodic laminar structure of nonlinear optical crystal*, Opt. Commun. **18,** 331–334 (1976).
85. D. E. Thompson, J. D. McMullen, and D. B. Anderson, *Second-harmonic generatioin in GaAs "stack of plates" using high-power CO_2 laser radiation*, Appl. Phys. Lett. **29,** 113–115 (1976).
86. M. M. Fejer, G. A. Magel, D. H. Jundt, and R. L. Byer, *Quasi-phase-matched second harmonic generation: Tuning and tolerances*, IEEE J. Quantum Electron. **28,** 2631–2654 (1992).
87. T. Y. Fan, C. E. Huang, B. Q. Hu, R. C. Eckardt, Y. X. Fan, R. L. Byer, and R. S. Feigelson, *Second harmonic generation and accurate index of refraction measurements in flux-grown $KTiOPO_4$*, Appl. Opt. **26,** 2390–2394 (1987).
88. W. Wiechmann, S. Kubota, T. Fukui, and H. Masuda, *Refractive-index temperature derivatives of potassium titanyl phosphate*, Opt. Lett. **18,** 1208–1210 (1993).
89. W. K. Burns and R. A. Andrews, *"Noncritical" phase matching in optical waveguides*, Appl. Phys. Lett. **22,** 143–145 (1973).
90. J. D. Bierlein, D. B. Laubacher, J. B. Brown, and C. J. van der Poel, *Balanced phase matching in segmented $KTiOPO_4$ waveguides*, Appl. Phys. Lett. **56,** 1725–1727 (1990).
91. T. C. Kowalczyk, K. D. Singer, and P. A. Cahill, *Anomalous dispersion phase-matched second harmonic generation in poled polymer waveguides*, Proc. SPIE **2700,** 152–163 (1996).
92. R. Normandin and G. I. Stegeman, *Nondegenerate four-wave mixing in integrated optics*, Opt. Lett. **4,** 58–59 (1979).
93. R. Normandin, S. Ltourneau, F. Chatenoud, and R. L. Williams, *Monolithic communications systems*, IEEE J. Quantum Electron. **27,** 1520–1530 (1991).
94. D. Vakhshoori and S. Wang, *Intergrable semiconductor optical correlator, parametric spectrometer for communication systems*, IEEE J. Lightwave Tech. **9,** 906–917 (1991).
95. G. D. Boyd and C. K. N. Patel, *Enhancement of optical second-harmonic generation (SHG) by reflection phase matching in ZnS and GaAs*, Appl. Phys. Lett. **8,** 313–315 (1966).
96. H. Komine, W. H. Long, Jr., J. W. Tully, and E. A. Stappaerts, *Quasi-phase-matched second-harmonic generation by use of a total-internal-reflection phase shift ini gallium arsenide and zinc selenide plates*, Opt. Lett. **23,** 661–663 (1998).
97. J. P. van der Ziel, *Phase-matched harmonic generation in a laminar structure with wave propagation in the plane of the layers*, Appl. Phys. Lett. **26,** 60–61 (1975).
98. A. Fiore, V. Berger, E. Rosencher, S. Crouzy, N. Laurent, and J. Nagle, *$\Delta n = 0.22$ birefringence measurement by surface emitting second harmonic generation in selectively oxidized GaAs/AlAs optical waveguides*, Appl. Phys. Lett. **71,** 2587–2589 (1997).
99. F. C. Zumsteg, J. D. Bierlein, and T. E. Gier, *$K_x Rb_{1-x} TiOPO_4$: A new nonlinear optical material*, J. Appl. Phys. **47,** 4980–4985 (1976).
100. L. K. Cheng and J. D. Bierlein, *KTP and isomorphs-recent progress in device and material development*, Ferroelectrics **142,** 209–228 (1993).
101. G. Hansson, H. Karlsson, S. Wang, and F. Laurell, *Transmission measurements in KTP and isomorphic compounds*, Appl. Opt. **39,** 5058–5069 (2000).
102. M. Roth, N. Angert, M. Tseitlin, and A. Alexandrovsk, *On the optical*

quality of KTP crystals for nonlinear optical and electro-optic applications, Opt. Materials **16,** 131–136 (2001).
103. B. Boulanger, I. Rousseau, J. P. Feve, M. Maglione, B. Menaert, and G. Marnier, *Optical studies of laser-induced gray-tracking in KTP*, IEEE J. Quantum Electron. **35,** 281–286 (1999).
104. Y. S. Liu, D. Dentz, and R. Belt, *High-average-power intracavity second-harmonic generation using $KTiOPO_4$ in an acousto-optically Q-switched Nd:YAG laser oscillator at 5kHz*, Opt. Lett. **9,** 76–78 (1984).
105. T. A. Driscoll, H. J. Hoffman, R. E. Stone, and P. E. Perkins, *Efficient second-harmonic generation in KTP crystals*, J. Opt. Soc. Am. B **3,** 683–686 (1986).
106. V. M. Garmash, G. A. Ermakov, N. I. Pavlova, and A. V. Tarasov, *Efficient second-harmonic generation in potassium titanate-phosphate crystasl with noncritical phasematching*, Sov. Tech. Phys. Lett. **12,** 505–506 (1986).
107. W. P. Risk, R. N. Payne, W. Lenth, C. Harder, and H. Meier, *Noncritically phase-matched frequency doubling using 994 nm dye and diode laser radiation in $KTiOPO_4$*, Appl. Phys. Lett. **55,** 1179–1181 (1989).
108. H. Vanherzeele, J. D. Bierlein, and F. C. Zumsteg, *Index of refraction measurements and parametric generation in hydrothermally grown $KTiOPO_4$*, Appl. Opt. **27,** 3314–3316 (1988).
109. H. Vanherzeele and J. D. Bierlein, *Magnitude of the nonlinear-optical coefficients of $KTiOPO_4$*, Opt. Lett. **17,** 982–984 (1992).
110. Q. Chen and W. P. Risk, *Periodic poling of $KTiOPO_4$ using an applied electric field*, Electron. Lett. **30,** 1516–1517 (1994).
111. G. Rosenman, A. Skliar, M. Oron, and M. Katz, *Polarization reversal in $KTiOPO_4$ crystals*, J. Phys. D, Appl. Phys. **30,** 277–282 (1997).
112. M. Oron, M. Katz, D. Eger, G. Rosenman, and A. Skliar, *Highly efficient blue light generation in flux grown $KTiOPO_4$ periodically poled by an electric field*, Electron. Lett. **33,** 807–809 (1997).
113. A. Englander, R. Lavi, M. Katz, M. Oron, D. Eger, E. Lebiush, G. Rosenman, and A. Skliar, *Highly efficient doubling with a high-repetition-rate diode-pumped laser with bulk periodically poled KTP*, Opt. Lett. **22,** 1598–1599 (1997).
114. A. Arie, G. Rosenman, A. Korenfeld, A. Skliar, M. Oron, M. Katz, and D. Eger, *Efficient resonant frequency doubling of a cw Nd:YAG laser in bulk periodically poled $KTiOPO_4$*, Opt. Lett. **23,** 28–30 (1998).
115. I. Shoji, T. Kondo, A. Kitamoto, M. Shirane, and R. Ito, *Absolute scale of second-order nonlinear-optical coefficients*, J. Opt. Soc. Am. B **14,** 2268–2294 (1997).
116. H. Karlsson, Ph.D. thesis, The Royal Institute of Technology, Stockholm, Sweden, 1997.
117. S. Kase and K. Ohi, *Optical absorption and interband Faraday rotation in $LiTaO_3$ and $LiNbO_3$*, Ferroelectrics **8,** 419–420 (1974).
118. G. L. Tangonan, M. K. Barnoshi, J. F. Lotspeich, and A. Lee, *High optical power capabilities of Ti-diffused $LiTaO_3$ waveguide modulator structures*, Appl. Phys. Lett. **30,** 238–239 (1977).
119. J.-P. Meyn and M. M. Fejer, *Tunable ultraviolet radiation by second-harmonic generation in periodically poled lithium tantalate*, Opt. Lett. **22,** 1214–1216 (1997).
120. L. K. Cheng, L. T. Cheng, J. Galperin, P. A. Morris Hotsenpillar, and J. D. Bierlein, *Crystal growth and characterization of $KTiOPO_4$ isomorphs from the self-fluxes*, J. Cryst. Growth **137,** 107–115 (1994).
121. G. Rosenman, A. Skliar, Y. Findling, P. Urenski, A. Englander, P. A. Thomas, and Z. W. Hu, *Periodically poled $KTiOAsO_4$ crystals for optical parametric oscillation*, J. Phys. D, Appl. Phys. **32,** 49–52 (1999).
122. H. Karlsson, F. Laurell, and L. K. Cheng, *Periodic poling of $RbTiOPO_4$ for quasi phase matched blue light generation*, Appl. Phys. Lett. **74,** 1519–1521 (1999).
123. R. L. Lipson, E. J. Baldes, and A. M. Olsen, *Mematoporphyrin deriva-*

tive: A new aid for endoscopic detection of malignant disease, J. Thorac. Cardiovasc. Surg. **42,** 623–629 (1961).
124. T. J. Dougherty, B. W. Henderson, S. Schwartz, J. W. Winkelman, and R. L. Lipson, in *Photodynamic therapy*, B. W. Henderson and T. J. Dougherty, eds., (Marcel Dekker, New York, 1992), pp. 1–15.
125. I. Wang, Ph.D. thesis, Lund University, The Jubileum Institute, Department of Oncology, Lund University Hospital, SE-221 85 Lund, Sweden, 1999.
126. J.-L. Boulnois, *Photophysical processes in recent medical laser developments: A review*, Lasers Med. Sci. **1,** 47–66 (1986).
127. Z. Malik and H. Lugaci, *Destruction of erythroleukaemic cells by photoinactivation of endogenous porphyrins*, Br. J. Cancer **56,** 589–595 (1987).
128. J. C. Kennedy, R. H. Pottier, and D. C. Pross, *Photodynamic therapy with endogenous protoporphyrin IX: Basic pronciples and present clinical experience*, J. Photochem. Photobiol. B **6,** 143–148 (1990).
129. J. C. Kennedy and R. Pottier, *Endogenous protoporphyrin IX, a clinically useful photosensitizer for photodynamic therapy*, J. Photochem. Photobiol. B **14,** 275–292 (1992).
130. K. Svanberg, T. Andersson, D. Killander, I. Wang, U. Stenram, S. Andersson-Engels, R. Berg, J. Hohansson, and S. Svanberg, *Photodynamic therapy of non-melanoma malignat tumours of the skin using topical δ-amino levulinic acid sensitization and laser irradiation*, Br. J. Dermatol. **130,** 743–751 (1994).
131. M. Kondo, N. Hirota, T. Takaoka, and M. Kajiwara, *Heme-biosynthetic enzyme activities and porphyrin accumulation in normal liver and hepatoma cell lines of rat*, Cell Biol. Toxicol. **9,** 95–105 (1993).
132. P. Hinnen, F. W. M. de Rooij, M. L. F. van Velthuysen, A. Edixhoven, R. van Hillegersberg, H. W. Tilanus, J. H. P. Wilson, and P. D. Siersema, *Biochemical basis of 5-aminolaevulinic acid-induced protoporphyrin IX accumulation: a study in patients with (pre)malignant lesions of the oesophagus*, Br. J. Cancer **78,** 679–682 (1998).
133. H. Heyerdahl, I. Wang, D. L. Liu, R. Berg, S. Andersson-Engels, Q. Peng, J. Moan, S. Svanberg, and K. Svanberg, *Pharmacokinetic studies on 5-aminolevulinic acid-induced protoporphyrin IX accumulation in tumours and normal tissues*, Cancer Lett. **112,** 225–231 (1997).
134. C. af Klinteberg, A. M. K. Enejder, I. Wang, S. Andersson-Engels, S. Svanberg, and K. Svanberg, *Kinetic fluorescence studies of 5-aminolevulinic acid-induced protoporphyrin IX accumulation in basal cell carcinomas*, J. Photochem. Photobiol. B **49,** 120–128 (1999).
135. J. Moan, L. W. Ma, and V. Iani, *On the pharmacokinetics of topically applied 5-aminolevulinic acid and two of its esters*, Int. J. Cancer **92,** 139–143 (2001).
136. J. T. H. M. van den Akker, V. Iani, W. M. Star, H. J. C. M. Sterenborg, and J. Moan, *Topical application of 5-aminolevulinic acid hexyl ester and 5-aminolevulinic acid to normal nude mouse skin: Differencies in protoporphyrin IX fluorescence kinetics and the role of the stratum corneum*, Photochem. Photobiol. **72,** 681–689 (2000).
137. P. Uehlinger, M. Zellweger, G. Wagnieres, L. Juillerat-Jeanneret, H. van den Bergh, and N. Lange, *5-Aminolevulinic acid and its derivatives: physical chemical properties and protoporphyrin IX formation in cultured cells*, J. Photochem. Photobiol. B **54,** 72–80 (2000).
138. M. S. Thompson, L. Gustafsson, S. Pålsson, N. Bendsoe, M. Stenberg, C. af Klinteberg, S. Andersson-Engels, and K. Svanberg, *Photodynamic therapy and diagnostic measurements of basal cell carcinomas using esterfified and non-esterified δ-aminolevulinic aced*, J. Porphyrins Phthalocyanines **5,** 147–153 (2001).
139. J. Moan and K. Berg, *The photodegradation of porphyrins in cells can be used to estimate the lifetime of singlet oxygen*, Photochem. Photobiol. **53,** 549–553 (1991).

140. K. Berg and J. Moan, *Lysosomes and microtubules as targets for photochemotherapy of cancer*, Photochem. Photobiol. **65,** 403–409 (1997).
141. K. W. Woodburn, Q. Fan, D. R. Miles, D. Kessel, Y. Luo, and S. W. Young, *Localization and efficacy analysis of the phototherapeutic lutetium texaphyrin (PCI-0123) in the murine EMT6 sarcoma model*, Photochem. Photobiol. **65,** 410–415 (1997).
142. V. H. Fingar, T. J. Wieman, S. A. Wiehle, and P. B. Cerrito, *The role of microvascular damage in photodynamic therapy: The effect of treatment on vessel constriction, permeability and leukocyte adhesion*, Cancer Res. **52,** 4914–4921 (1992).
143. D. L. Liu, I. Wang, S. Andersson-Engels, C. H. Håkansson, U. Stenram, and K. Svanberg, *Intra-operative laser-iinduced photodynamic therapy in the treatment of experimental hepatic tumours*, Eur. J. Gastroenterol. Hepatol. **7,** 1073–1080 (1995).
144. S. Pålsson, L. Gustafsson, N. B. N, M. S. Thompson, S. A.-E. S, and K. Svanberg, *Kinetics of the superficial perfusion and temperature in connection with photodynamic therapy of basal cell carcinomas using esterified and non-esterified 5-aminolaevulinic acid*, Br. J. Dermatol. **148,** 1179–1188 (2003).
145. *Ceralas PDT lasers for various photosensitizers*, Biolitec Inc., CeramOptec products, http://www.ceramoptec.de/ceralas.htm.
146. M. Stenberg, M. S. Thompson, T. Johansson, S. Pålsson, C. af Klinteberg, S. Andersson-Engels, U. Stenram, S. Svanberg, and K. Svanberg, in *Optical biopsy and tissue optics*, I. J. Bigio, G. J. Mueller, G. J. Puppels, R. W. Steiner, and K. Svanberg, eds., (Proc. SPIE, 2000), Vol. 4161, pp. 151–157.
147. Q. Peng, T. Warloe, K. Berg, J. Moan, M. Kongshaug, K.-E. Giercksky, and J. M. Nesland, *5-Aminolevulinic Acid-Based Photodynamic Therapy: Clinical Research and Future Challenges*, Cancer **79,** 2282–2308 (1997).
148. I. Wang, N. Bendsoe, C. af Klinteberg, A. M. K. Enejder, S. Andersson-Engels, S. Svanberg, and K. Svanberg, *Photodynamic Therapy versus cryosurgery of basal cell carcinomas; results of a phase III randomized clinical trial*, Br. J. Dermatol. **144,** 832–840 (2001).
149. S. Svanberg, S. Andersson-Engels, R. Berg, J. Johansson, and K. Svanberg, Physics Department, Lund Institute of Technology, Sweden. Swedish patent (1996).
150. N. Ohlsson and O. Rylow, *Development of a multifibre system for interstitial photodynamic therapy of malignant tumours*,, Physics Department, Lund Institute of Technology, Sweden. LRAP-240 (1998).
151. T. Johansson, M. S. Thompson, M. Stenberg, C. af Klinteberg, S. Andersson-Engels, S. Svanberg, and K. Svanberg, *Feasibility study of a system for combined light dosimetry and interstitial photodynamic treatment fo massive tumors*, Appl. Opt. **41,** 1462–1468 (2002).
152. G. G. Stokes, *Über die Änderung der Brechbarkeit des Lichtes*, Phil. Transact. **107,** 11–11 (1852).
153. H. Stübel, *Die fluoreszenz tierischer gewebe in ultravioletten licht*, Pflügers Arch. **142,** 1–1 (1911).
154. L. Baert, R. Berg, B. van Damme, M. A. D'Hallewin, J. Johansson, K. Svanberg, and S. Svanberg, *Clinical fluorescence diagnosis of human bladder carcinoma following low-dose Photofrin injection*, Urology **41,** 322–330 (1993).
155. K. Svanberg, E. Kjellén, J. Ankerst, S. Montán, E. Sjöholm, and S. Svanberg, *Fluorescence studies of hematoporphyrin derivative (HpD) in normal and malignant rat tissue*, Cancer Res. **46,** 3803–3808 (1986).
156. U. Gustafsson, S. Pålsson, and S. Svanberg, *Compact fiber-optic fluorosensor using a continuous-wave violet diode laser and an integrated spectrometer*, Rev. Sci. Instr. **71,** 3004–3006 (2000).
157. W. Alian, S. Andersson-Engels, K. Svanberg, and S. Svanberg, *Laser-induced fluorescence studies of meso-tetra(hydroxyphenyl)chlorin in ma-*

lignant and normal tissues in rat, Br. J. Cancer **70,** 880–885 (1994).
158. M. Andreasson and O. Sandström, Master's thesis, Lund Institute of Technology, Lund, Sweden, 1998.
159. S. Andersson-Engels, J. Johansson, and S. Svanberg, *Medical diagnostic system based on simultaneous multispectral fluorescence imaging*, Appl. Opt. **33,** 8822–8029 (1994).

Part II